POLITECNICO DI TORINO

Master Degree Course
in Electronic Engineering

Master Degree Thesis

Study of new oscillator schemes based on exceptional points of degeneracy

Supervisors
prof. Ladislau Matekovits (Politecnico di Torino)
prof. Filippo Capolino (University of California, Irvine)

Candidate
Enrico Maria Renzi

A.Y. 2018-2019

ABSTRACT

The aim of this thesis is to introduce a new concept of distributed radiating and oscillating device by investigating and manipulating some dispersive properties of particular periodic structures based on planar technology.

Floquet-Bloch modes describe the propagation of electromagnetic waves in periodic transmission lines. Two-port periodic guiding structures allow the occurrence of *regular* band edge (RBE), that is a fundamental class of exceptional point of degeneracy (EPD). Under these special dispersion conditions, both the two system eigenvectors and eigenvalues coalesce. This represents a standing wave where energy is not flowing through the periodic circuit.

A description of the wide range of applications in which dispersive degeneracy conditions have crucial importance is presented. As an example the reader will notice how it is possible to have better control of beam and directivity in fast travelling wave radiators, to allow the design of high Q-factor and high spectral purity oscillators and obtain sensors with enhanced sensitivity.

After a basic introduction to radio frequency and microwave oscillators, leaky wave antennas and to the basis of the periodic structures mathematical model, the attention is eventually focused on the general transmission line theory of exceptional points of degeneracy. For these structures, the central concept of gain (introduced by active devices) and loss (ohmic and radiation) balance is presented, pointing out how symmetries are involved in determining whether or not an EPD can exist.

As a final result of the study, two microstrip ladder oscillators schemes based on regular band edge are proposed. Microstrip lines, interdigitated capacitors and non-linear active devices are conveniently arranged in asymmetric and folded structures able to provide a stable oscillation, high spectral purity, high loaded Q-factor, ability to radiate at the oscillation frequency along with a simple design.

Finally, a last section presents some considerations about the possibility of having oscillation in looped ladder structures. Where the behaviour of an infinitely long periodic structure is reproduced, EPD can be ideally retrieved by providing gain. Operating near such special degeneracy conditions further improvements appear, leading to potential performance enhancement in a broad variety of microwave and optical devices.

ACKNOWLEDGMENTS

Part of this thesis was carried out in prof. Filippo Capolino's research laboratory at Department of Electrical Engineering and Computer Science, University of California, Irvine (U.S.A.).

I would like to thank from the bottom of my heart all those who made to write this Thesis possible. Special thanks to my supervisors Prof. Ladislau Matekovits and Prof. Filippo Capolino, for their patience, for their availability and their precious teachings, which will accompany me in my future professional life. Special thanks to Hamidreza Kazemi, Dmitry Oshmarin, Ahmad Almutawa and in particular to Tarek Mealy and Ahmed Abdelshafy, who guided me in the preparation and realization of my project, sharing with me their knowledge, some laugher, and their, already little, time. Special thanks to prof. Franco Maddaleno, unique and inimitable guide and to Ermanno Citraro and Alessio Berto, who were exceptional travel and adventure companions in California. Special thanks you to Fabio and Lorenzo, irreplaceable friends. And least but not last, a warm thank you to Sofia, always present, dulcis in fundo.

CONTENTS

1 INTRODUCTION 1
1.1 Background and Thesis Aim 1
1.2 Thesis outline 3

I THE STATE OF THE ART

2 THE STATE OF THE ART 7
2.1 Exceptional Points of Degeneracy: Overview and Applications 7
2.2 Thesis Motivation 12

II THEORETICAL BACKGROUND

3 RF AND MW RESONATORS 15
3.1 Series and Parallel resonant circuits 15
3.1.1 Series resonant circuits 15
3.1.2 Parallel resonant circuits 16
3.1.3 Loaded and unloaded Q-factor 17
3.1.4 The Coupling Coefficient and Critical Coupling 17
3.2 Interdigitated Capacitor as Resonant Unit 18
4 RF AND MW OSCILLATORS 21
4.1 Kurokawa's criteria for oscillation 21
4.2 Negative Resistance From Active Elements 23
4.2.1 Negative Resistance from Tunnelling Diodes 24
4.2.2 Negative Resistance from Transistor Model 25
4.3 Q-factor in oscillators 25
4.4 Noise in Oscillators 26
4.5 Some Oscillator Design Considerations 27
5 PERIODIC STRUCTURES AND EPDS 29
5.1 Infinite Periodic Structures 29
5.2 Discrete Periodic Structures 33
5.3 Dispersion Diagram of a Periodic Structure 34
5.4 Phase and group velocity 35
5.5 Floquet's Theorem and Spatial Harmonics 35
5.6 N-th order EPDs 37
5.7 EPDs in practice 39
5.8 Regular Band Edge, RBE 40
6 ANTENNA THEORY AND LEAKY WAVE ANTENNAS 43
6.1 Antenna Parameters 43
6.1.1 Radiation Power and Intensity 43
6.1.2 Beamwidth, Directivity, Efficiency and Gain 44
6.1.3 Polarization 46
6.2 Leaky wave antennas 47
6.3 Field Behaviour of Leaky Waves 48
6.3.1 Field Behaviour in Periodic LWA 51

III DESIGN AND SIMULATION
7 DESIGN AND SIMULATION OF TWO SINGLE-LADDER RBE RADIATING OSCILLATORS 57
7.1 Motivation 57
7.2 RBE Oscillator at $\beta d = 0$ 58
7.2.1 Unit Cell Design 59
7.2.2 Frequency response of the passive ladder circuit 64
7.2.3 Active single-ladder circuit and RBE 68
7.2.4 Modes Analysis 76
7.2.5 Oscillation and Radiation Analysis 81
7.3 Folded ladder design 86
7.4 Closed Loops and Distributed Gain 87
IV CONCLUSIONS
8 CONCLUSIONS 91
V APPENDIX
A PROOF OF KUROKAWA'S STABILITY CONDITION 95
B ENERGY FLOW THROUGH A PERIODIC STRUCTURE 97
C FARFIELD FIELDS DERIVATION 99
D TRANSMISSION LINE CIRCUIT MODEL 101
E RBE OSCILLATOR AT $\beta d = 0$, SIMULATION SETUP 103
F EIGENMODE SOLVER MODES FIELD CUTS 111
G 8 CELL ARRAY SIMULATION SETUP 119
BIBLIOGRAPHY 121

LIST OF FIGURES

Figure 2.1 Sketch of the dispersion diagram with three different degeneracies: second order (RBE), third order (SIP) and fourth order degeneracy (DBE), respectively [4]. 7
Figure 2.2 (a) FPC realized in [8] (top) and giant transmission gain obtained compare to standard and RBE FPC (bottom).(b) CROW structure used in [4]. 9
Figure 2.3 (a) Second order degeneracy retrieved by the addition of gain [10]. (b) Fourth order degeneracy retrieved by adding gain [7]. 9
Figure 2.4 (a) Two uniform coupled transmission lines: one is lossy whereas the other one is active. (b) A second order EPD is obtained (the metric $|\det(U)|$ is close to zero where degeneracy appears). (c) Extremely narrow beam LWAs can be conceived with EPD coupled transmission lines. (d) Beamwidth varying with different values of mutual capacitance C_m [10]. 10
Figure 2.5 Design proposed in [7]: (a) unit cell, (b) realised discrete periodic structure, (c) simulation and measurement of dispersion diagram, (d) shift from ω_d in reflection and transmission parameters 11
Figure 2.6 (a) Double ladder oscillator realised in [6]. (b) Minimum driving admittance scales as $1/N^5$ for DBE structure. (c) Q-factor versus the number of cells for different loads. 11
Figure 3.1 Series RLC resonator. 15
Figure 3.2 Parallel RLC resonator. 16
Figure 3.3 (a) Printed interdigital capacitor in microstrip technology with microstrip access lines [29]. (b) Interdigital capacitor design parameters [29]. (c) Interdigital capacitor equivalent circuit. 18
Figure 3.4 Equivalent circuit for a microstrip interdigital capacitor provided with access lines. 20
Figure 4.1 Negative resistance (a) series and (b) parallel oscillator circuit model. 21
Figure 4.2 Example of V-I non linear third order characteristic around a given bias point. 23
Figure 4.3 (a) Esaki diode small signal equivalent circuit model and (b) output characteristic [37]. 24
Figure 4.4 Negative resistance BJT with capacitive feedback equivalent circuit. 25
Figure 4.5 Noise power versus frequency for a transistor amplifier operating at frequency f_0 [28]. 26

Figure 4.6 Modulation of the oscillation frequency f_c due to phase noise [28]. 27
Figure 5.1 Infinite periodic structure blocks model. 29
Figure 5.2 Dispersion diagram for a lossless unitcell where stop and pass bands are highlighted. (a) Phase shift (propagation constant). The first three harmonics are plotted and frequencies ω_{ei} limit the boundaries between passbands and stopbands. (b) Attenuation constant. 34
Figure 5.3 Visual difference between phase velocity v_p and group velocity v_g. 36
Figure 5.4 Dispersion diagram expanded in for n spatial harmonics. Solid lines are for forward propagating modes, dashed lines for backward propagation. 37
Figure 5.5 Coalescence of two Floquet harmonics at FBZ edge ($\beta d = \pi$) in a lossless structure. 38
Figure 5.6 Detail on half FBZ edge ($\beta d = \pi$) for a periodic lossy structure with and without loss and gain balance. 39
Figure 6.1 Polarization plane for an electromagnetic wave and its polarization ellipse as a function of time [42]. 46
Figure 6.2 Ray picture used as a physical interpretation of field behaviour and radiated power in leaky-wave antennas: (a) forward leaky wave and (b) backward leaky way [43]. 49
Figure 6.3 Brillouin diagram plotted as $k_0 d$ vs $\beta_n d$ in which shadow and radiation region are highlighted. Radiation cone is defined above the solid yellow lines. 52
Figure 6.4 Closed stop band occurs at $\beta_0 = \pi$, corresponding to bounded modes. Open stopband occurs around $\beta_0 = 2\pi$, where radiation is possible [43]. 53
Figure 7.1 (a) Interdigital capacitor microstrip printed model. (b) Simplified model for describing radiation from interdigital capacitor fingers. (c) Layout of the symmetrical unit cell realised in ADS with the parameters in table 7.2. 60
Figure 7.2 (a) Dispersion diagram for the lossy symmetrical unit cell (table 7.2). (b) $\beta d = 0$ and Z_B are compared. (c)(d) Bloch impedance for the forward and backward propagating mode. 62
Figure 7.3 Input impedance of the cascade of 8, 16, 32, 96 uni cells (last cell terminated on a short circuit). 63
Figure 7.4 Layout of the asymmetrical unit cell extracted in ADS with parameters in table 7.3. 64
Figure 7.5 (a) Dispersion diagram for the asymmetrical lossless unit cell (table 7.3). (b) $\beta d = 0$ compared with Z_B. (c)(d) Bloch impedance for the forward and backward propagating mode. 65

Figure 7.6 (a) Dispersion diagram for the asymmetrical lossy unit cell (table 7.3). (b) $\beta d = 0$ compared with Z_B. (c)(d) Bloch impedance for the forward and backward propagating mode. 66
Figure 7.7 (a) Lossless structure. Discrete structure input impedance varying the number of unit cells: input resistance (above), input reactance (below). (b) Lossless structure. Discrete structure input impedance varying the number of unit cells: input resistance (above), input reactance (below). 67
Figure 7.8 (a) Simulation setup in ADS for Q-factor evaluation (b) Total loaded Q-factor for the passive ladder structure. 68
Figure 7.9 Block scheme for the time domain simulation of the circuit with asymmetrical unit cell. 69
Figure 7.10 (a) Time domain response of the lossless ladder oscillator based on asymmetrical unit cell ($N = 8$). (b) Fourier transform of the time domain response shown in (a). As i appears the spectrum is very pure in a very large bandwidth. (c) Detail on the voltage wave form and to the associated phase. 71
Figure 7.11 (a) Time domain response of the lossyladder oscillator based on asymmetrical unit cell ($N = 8$). (b) Fourier transform of the time domain response shown in (a). As i appears the spectrum is very pure in a very large bandwidth also in the lossy case. (c) Detail on the voltage wave form and to the associated phase. The phase shift is 72
Figure 7.12 (a) Unit cell simulated with gain element. (b) Dispersion diagram for the unit cell with and without gain. 73
Figure 7.13 (a) g_s parametrization as a function of the number of cell. The driving admittance can is fit by $1/N^{2.7}$ suggesting the presence of a RBE. (b) Voltage exponential decay along the line for $N = 8, 16$. The voltage remains almost constant by varying the number of cells. (c) Peak voltage value is slightly changed by varying g_e. 74
Figure 7.14 (a) ADS MoM simulation is compared with CST FD and TD solver with employing discrete face ports. (b) ADS MoM simulation is compared with CST FD and TD solver with employing waveguide ports and deembedding the scatterign parameters. (c) ADS lossless simulation versus CST eigenmode solver. 75

Figure 7.15 Mode 2: electric field distribution for interdigital capacitor at f_r. The high value of the electric field are non physical and due to the eigenmode solver, in which losses are ignored. A different color map is used in this plots in order to better understand the field distribution in the capacitor. 76
Figure 7.16 (a)(b)(c)Mode 2: electric field distribution for the unit cell at f_r. The high value of the electric field are non physical and due to the eigenmode solver, in which losses are ignored. (d) Electric field surrounding the unit cell at different cutting planes. 79
Figure 7.17 (a)(b)(c) Mode 2: magnetic field distribution for the unit cell at f_r. The high value of the electric field are non physical and due to the eigenmode solver, in which losses are ignored. (d) Magnetic field surrounding the unit cell at different cutting planes. 80
Figure 7.18 8 cell array used as resonant-radiating device. Port 1 is used to feed the structure, whereas port 2 is used as load. Port 1 is used to feed the structure, whereas port 2 is used as load. 81
Figure 7.19 (a) Driving point impedance for the lossy designed array. (b) Output impendance for the designed array. (c) Voltage in time domain response at the input port. (d) Output spectrum: oscillation is located at $f_{r8} = 2.6145\,\mathrm{GHz}$. 82
Figure 7.20 Scattering and loss parameters for (a) lossy and (b) lossless structure: reflection coefficient (top lef), transmission coefficient (top right), total loss (bottom left) and VSWR (bottom right). 83
Figure 7.21 (a-d)Farfield radiation pattern and related cuts on the main planes for the lossy array. Radiation efficiency is very low because of the large amount ohmic and dielectric losses. (e) Axial ratio: the polarization is mainly elliptical in the main radiation direction. (f) Broadband radiation loss for lossy $N = 8$ array. (g)Broadband radiation loss for lossless $N = 8$ array. 85
Figure 7.22 Radiated field in the vicinity of the array at various phase steps showing the existance of a travelling wave. The cylindrical surface on which the electric field is evaluated is oriented along th x axis centered around the device. It has radius equal to 20 cm and height equal to 1 m. 86
Figure 7.23 (a) Realised folded unit cell. (b) Voltage waveform of an 8 cell structure. (c) Output spectrum at each oscillator node. (d) Zoom on voltage waveforms. 87
Figure 7.24 Looped structure mimicking an infinitely long structure. 88
Figure D.1 Transmission line T-circuit equivalent. 101

LIST OF TABLES

Table 7.1 Rogers RO6010 main technological parameters. 59
Table 7.2 Symmetric unit cell design parameters. The total number of fingers is N_p=80. 61
Table 7.3 Symmetric unit cell design parameters. The total number of fingers is N_p=60. 63
Table 7.4 Main result from simulation of the 8 cells ladder lossless array. 69
Table 7.5 Main result from simulation of the 8 cells ladder lossy array. 70
Table 7.6 Main result from full wave simulation of the 8 cells ladder array. 81

1 INTRODUCTION

1.1 BACKGROUND AND THESIS AIM

An *exceptional point of degeneracy* (EPD) is a singularity in waveguiding structures dispersion diagram (DD) at which eigenvectors are collinear and eigenvalues degenerate [1]. Waves travelling in systems able to operate at these points experience substantial reduction of group velocity. Hence, structures capable of supporting these extremely slow modes, exhibit very high quality factor Q [2], [3] and spectral purity, being also very well suited for application including filters-resonators [4], high-power microwave generation [5] and oscillators [6].

BACKGROUND Coupled periodic transmission lines [7], periodically loaded waveguides [8], anisotropic dielectric stacks and microwave cavities [3] are some example of one dimensional periodic structures exhibiting EPDs. All the information regarding wave propagation and frequency dispersion are contained in the unit cell, the basic block defining the periodicity, and can be extracted through its $ABCD$ parameters, also known as transmission matrix ($\underline{\mathbf{T}}$) [9]. The diagonalization of $\underline{\mathbf{T}}$ provides the system eigenvalues λ and its associated eigenvectors $\psi_e(z)$. This set of parameters represents the complex wave number $\lambda = \alpha + j\beta$ and the associated orthonormal basis that defines all the possible combinations of waves that can propagate in the structure, expressed as $\psi(z) = \psi_0 e^{\pm\lambda z}$. Wherever two or more eigenvalues and they relative eigenvectors degenerate in the DD, i.e. they collapse in a set of one only (λ,ψ_e), there an EPD is found [10]. Moreover, the number of coalescing eigenvalues defines the order m of the EPD, for instance: 2$^{\text{nd}}$ order in case of a *regular band edge* (RBE), 4$^{\text{th}}$ order in case of *degenerate band edge* (DBE) [2]. If the degeneracy appears $\underline{\mathbf{T}}$ becomes defective and looks as a Jordan Block [10]. These degeneracies usually are located at the edges of first Brillouin zone (FBZ) where the propagating wave phase shift is $\beta d = 0, \pi$, and dispersion relation can be approximated as $(\omega - \omega_e) \propto (\beta - \beta_e)^m$. Group velocity $v_g = d\omega \,/\, d\beta$ is null at (ω_e, β_e) and much more smoother close in the vicinity of this point for increasing values of m. Therefore, at EPDs group velocity vanishes, group delay dramatically in a narrower bandwidth inducing an increment in quality factor Q and frequency selectivity of the periodic structure. EPDs do not exist in practice both because infinite periodic structures do not exist and because the presence of losses and the and in RF, MW and optic devices. By compensating losses through gain [10] or manipulating structures topology [4] an EPD can be ideally retrieved also in real cases.

MOTIVATIONS AND AIM OF THE THESIS Recent research interest in structures exhibiting EPDs has arised in a number of applications, spanning from particles sensing [11] ad high transmission gain Fabry-Pérot lasers in optics

[3] to narrow beam antennas [10] and high power electron beams [5], [12] in electronics. Many research papers have laid the foundation and the formalism to better understand how to engineer and recognise the presence of an EPD in finite periodic structure and coupled transmission lines [4], [7], [13]. In particular, the design of EPD oscillators has recently received a surge of interest thanks to their capability of exhibiting ultra-high quality factors, extremely pure oscillation spectra and very low noise characteristics [8], [14]. An example is in [6], where two topologies of ladder oscillators are realised by means of purely LC circuits exhibiting oscillation around RBE frequency for the former and DBE frequency for the latter, respectively. In particular, it must be recalled that the order of degeneracy is at most equal to the number of terminations of a given cell (two in case of a single ladder and four, in case of a double ladder).

The single ladder, has N cascaded cells closed on a termination load and its topology exhibits some very peculiar properties uniquely related to the presence of an RBE, namely: the minimum driving point admittance, g_s, scales as $1/N^3$, the total Q-factor is proportional to N^3, the voltage waveform peak is barely independent on the used driving point admittance above sturt-up threshold and load change are very well sustained and mode jumping is not present. Besides, the oscillation frequency ω_r shift from RBE frequency ω_e is proportional to $1/N^2$. Even if this structures have been proven to exhibit EPDs they are or realised with lumped elements, or by means of loaded waveguides. No mention in literature is present about the realization of this kind of topology by means of microstrip lines. Relying on the previous assumptions, one question may be posed: *(i) is it possible to design any other EPD oscillating structures based on microstrip technology?*

Another challenging aspect can be brought to light. Previously it has been mentioned that loss (conduction, dielectric and radiation) can be ideally compensated by inserting gain in the structure. At input port this would make the circuit to look very similar to a purely reactive resonator. However, loss compensation would not be distributed, but rather present in a discrete location. Therefore, a consistent part of the circuit could still present radiation loss if conveniently designed. Moreover, it is necessary to recall that an high Q-factor implies a small amount of losses, whereas the presence of radiation resistance is in contrast to this. So, the next design question would be: *(ii) is it an EPD condition sufficient oscillator also able to radiate, even if this is in contrast to having a large Q-factor?*

The aim of this Thesis is then *to answer to both design questions (i) and (ii) through the derivation, simulation and characterization of novel oscillator schemes based on exceptional points of degeneracy.*

PERSONAL CONTRIBUTION In order to answer to design questions (i) and (ii) an eight cells single ladder RBE oscillator have been realised. The EPD is located at $\beta d = 0$. The first design step of a suitable resonating element. An interdigital capacitor has been employed and designed to maximise its radiation resistance and minimize phase shits among radiating edges on its surface. After that, two access lines have been added to realise the unit cell. Asymmetric access lines turned out to be more convenient to obtain EPD at centre FBZ. The final layout area is approximatively $18\,\mathrm{mm} \times 18\,\mathrm{mm}$. Then, the unit cell is then simulated in full wave simulator and characterized to successfully verifying that an EPD could be retrieved by adding gain.

Next, a certain number of unit cell is cascaded to realize the actual resonator. The characterisation of the loaded quality factor suggests that using 8 cells loaded with a short circuit the structure behaves almost as an infinite periodic structure. After gain is added, provided by means of the equivalent model of a nonlinear cubic voltage controlled current source, it is then proved that the structure is an RBE oscillator. In fact, the figures of merit related to single ladder RBE oscillators are verified to be featured by the design (for instance $g_s = 1/N^{2.7}$). In particular the phase shift between each cell is 8 deg, meaning that the oscillator is actually working very close to $\beta d = 0$, i.e. the band edge (each cell in phase with the others). Moreover, resonance frequency $f_r = 2.535\,\mathrm{GHz}$ is slightly shifted from EPD frequency $f_e = 2.4561\,\mathrm{GHz}$. Besides, maximum loaded quality factor is $Q_{t,max} \approx 2000$ and minimum driving point impedance is $g_{e,min} = 5.8\,\mathrm{mS}$.

The next step it to perform eigenmode simulation by means of fullwave simulator to verify the T-matrix method validity and analysing field topology of the radiating mode. The radiating mode turns out to be the first $n = -1$ Floquet harmonic (see Chapter 5 for reference).

Full wave frequency domain simulations eventually suggest that the oscillator does not show particularly remarkable radiation properties. In fact even if the radiating mode is a leaky wave and the structure is working as leaky wave antenna (LWA), radiation efficiency is low due to large conduction and dielectric losses ($\eta_{nc} \simeq -15\,\mathrm{dB}$ for the lossless structure versus $\eta_{nc} \simeq -30\,\mathrm{dB}$ in lossy). This result suggests that the oscillator may be used as nearfield source rather than farfield ($|E_{pk}| \simeq 0.7\,\mathrm{V/m}$ at $0.5\,\mathrm{m}$ from the structure, with an excitation of $0.5\,\mathrm{W}$). Keep in mind that this result has been obtained without the addition of gain, because of simulation limitation. The actual structure could therefore present significant enhancements. Further steps such as a prototype realization and topology improvements are under investigations.

1.2 THESIS OUTLINE

The Thesis is organized in eight chapters:

- Chapter 1: an overview on the work developed is outlined, along with the Thesis motivations and aims.
- Chapter 2: the state of art about the research on EPDs is presented, along with some applications based on this concept.
- Chapter 3: some basic details about RLC resonators are given. The interdigital capacitor resonator is presented.
- Chapter 4: theory of oscillators is presented along with some figure of merit. Some configurations of negative resistance oscillators are described.

- Chapter 5: the detailed and rigorous mathematical model for periodic structures based on transmission matrix method is presented. EPD theory in periodic structures is deeply analysed. This is the core theoretical chapter and the reader is invited to start the reading from here.
- Chapter 6: basic antenna theory and formalism is developed. Working principles of periodic leaky wave antennas are explained in detail.
- Chapter 7: the design and characterisation of an RBE oscillator is presented. At the chapter end two more circuits are introduced and they are currently under investigation.
- Chapter 8: conclusion about the developed work and future works are introduced.

Part I

THE STATE OF THE ART

2 THE STATE OF THE ART

2.1 EXCEPTIONAL POINTS OF DEGENERACY: OVERVIEW AND APPLICATIONS

In literature an *exceptional point of degeneracy* (EPD) is defined as a point in the parameters space describing frequency dispersion of a structure, in which two or more system eigenmodes and eigenvalues coalesce [1]. This particular condition usually takes place at singularities of the dispersion diagram, where group velocity vanishes and some properties of the system may be enhanced. In practice, they can be found in lossless waveguides operating at cutoff frequency or at the band edge of periodic structures and more in general in both electronic [7], [8], [12] and optical [2], [4], [15] devices conveniently engineered.

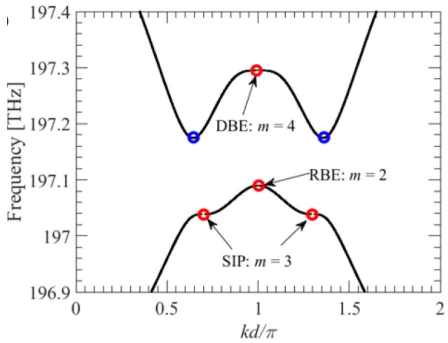

Figure 2.1: Sketch of the dispersion diagram with three different degeneracies: second order (RBE), third order (SIP) and fourth order degeneracy (DBE), respectively [4].

Simple degeneracy, regarding eigenvalues or eigenmodes only is a much weaker state than what one has with EPDs. In fact, the former condition originates a *diabolic point* (DP) or *double semi-simple eigenvalue*, where two eigenvalues coalesce in the dispersion diagram [11]. Whether the former condition is less demanding, on the contrary to have an EPD two conditions must concurrently verify [10]:

- Eigenvalues, λ_i, geometrical multiplicity is larger than algebraic multiplicity, i.e. they degenerate;
- Eigenmodes, ψ_i, associated to λ_i coalesce (they are superposed).

Another key difference between the two kinds of singularities lies in the different response that a system operating around and EPD shows in case of different perturbation. A perturbation ε can be a change in the system design parameter, a variation in working condition or in external excitations. The effect produced by ε traduces in a degeneracy disappearance and also known as *mode splitting*. In case of DP the eigenmode splitting is proportional to perturbation strength ε, whereas in case of EPD the splitting scales as $\varepsilon^{1/m}$, with m the order of degeneracy, i.e. the number of coalescing eigenmodes and eigenvectors. The result is that for a sufficiently small perturbation ε, the splitting at the exceptional point is larger meaning that they exhibit larger sensitivity to external stimuli, if they are sufficiently small [11]. Though, this property represents both a benefit and a drawback. In fact, EPDs result to be extremely sensitive to change in system and external parameters, meaning that they are very difficult to observe in practice.

A first proof of EPDs existence and measurability has been observed in microwave microcavities by Dembowski *et al.* in 2001 [16]. After this experiment, a surge of interests on this topic arised in solid state physics, and EPDs have became to be observed in many different systems such as in coupled atom-cavity systems [17], microwave cavities [18], [19] and optical microcavities [20], [21].

The simplest EPD can be found in uniform hollow waveguides, having in mind the dispersion relation close to cutoff frequency [8]. In this case backward and forward modes coalesce approaching $\beta = 0$ in the dispersion diagram. In this instance, two eigenmodes and two eigenvalues degenerate represents a 2$^{\text{nd}}$ order degeneracy (figure 2.1), i.e. a *regular band edge* (RBE) [22]. Applications of RBE can be also found in high power electron beam oscillators such as [5]. Similarly a 3$^{\text{rd}}$ order degeneracy, or *stationary inflection points* (SPI), can be defined if the degeneracy is threefold. Evidences of third order degeneracies can be found for instance in coupled resonator optical waveguides [4]. The same applies to a fourth order EPD, also known as *degenerate band edge* (DBE), that can be observed for example in Fabry-Pérot cavities based on anisotropic stratified dielectric stacks [2] and coupled transmission lines [7].

The feature that makes EPDs so valuable if present in a system, is a set of properties related to frequency dispersion. For instance, a structure that exhibits an EPD of order m, shows a dispersion relation that can be asymptotically approximated around the singularity as:

$$(\omega - \omega_e) \propto (\beta - \beta_e)^m \tag{2.1}$$

where ω and β are the angular frequency and the guided wavenumber, whereas the point (β_e, ω_e), designed by the subscript e, defines the degeneracy location [10]. Moreover, modelling a device operating with its system matrix, one has that it is *defective* at EPD. Under this assumption (demonstrated in [10]) the matrix is a Jordan block, whose solution eigenmodes can be expressed as $\psi(z) \propto z^{q-1} e^{jkz} \psi_0^q(z)$, with $q = 2, 3, \ldots, m$, and $\psi_0^q(z)$ the generalized eigenvector [23]. As a matter of fact, RBEs usually occurs at band edge and this condition is associated with slow-wave properties, meaning that group velocity reduces there, eventually vanishing when reaching $\beta = 0, \pi/d$ [24]. This is one of the key properties of EPD systems. For instance distributed and waveguide resonators exploiting this working principle can support modes with extremely high group delay, featuring very high quality factors [2], [25], [26], being hence suitable to application like narrowband filters, high power microwave generation [5], [8], ultra high-

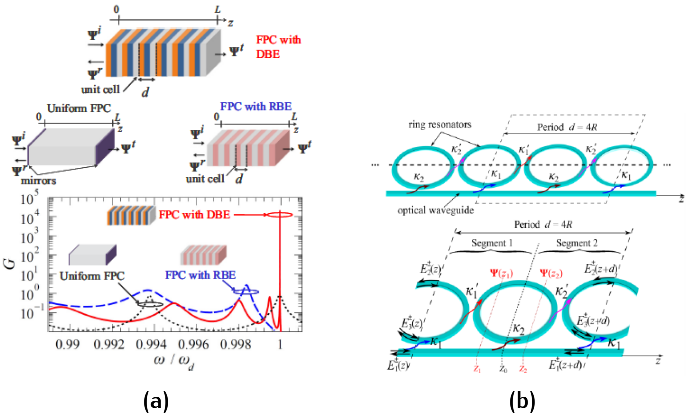

Figure 2.2: (a) FPC realized in [8] (top) and giant transmission gain obtained compare to standard and RBE FPC (bottom). (b) CROW structure used in [4].

Q resonator [3], ultra low-threshold oscillators [6] and narrow-beam leaky wave antennas [7].

An example of giant Q-factor can be found in [8], where a Fabry-Pérot cavity (FPC) resonator made of unconventional photonic crystals, composed by three anisotropic dielectric layers, is realised (figure 2.2a). The structure is periodic and each unit cell is a stack of three misaligned anisotropic (birinfrangent) layers. This kind of structure, unlike a standard or two-layers unit-cell structure (RBE) FPC, is proved to support DBE and the authors demonstrate that the giant enhancement in the Q-factor and transmission power gain is related to this property.

Exceptional point of degeneracies do not exist in practice, since losses and imperfections are omnipresent in real devices [10]. Moreover, as previously mentioned, EPD systems are extremely susceptible to parameters variation and perturbation.

Real systems may be reconducted to EPD by introducing gain (figure 2.3), in a localized or distributed way, retrieving the degeneracy. This requirement also satisfy the Parity-Time (PT) symmetry to develop exceptional points with gain and loss balance [7]. Coupled uniform waveguides (CW)

Figure 2.3: (a) Second order degeneracy retrieved by the addition of gain [10]. (b) Fourth order degeneracy retrieved by adding gain [7].

have been demonstrated to sustain second order EPDs thanks to gain and loss balance condition. Normally, CW do not show EPDs except from zero frequency, where four eigenmodes are collinear. Suppose now to have the system in figure 2.4. One can observe that two coupled lines are present: one of them is lossy and the other one is fed by distributed gain element. In this condition, energy is transferred from the active line to the lossy line, and a second order EPD can be obtained [10]. Moreover, the use of such a structure, paved the way to new concept of leaky wave antennas (LWA) where ultra narrow beam and enhanced directivity can be achieved. By con-

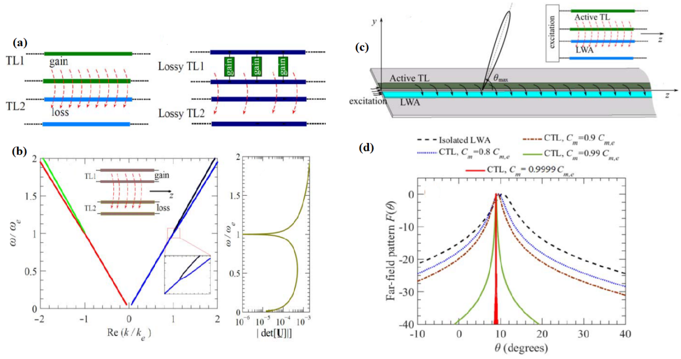

Figure 2.4: (a) Two uniform coupled transmission lines: one is lossy whereas the other one is active. (b) A second order EPD is obtained (the metric $|\det(U)|$ is close to zero where degeneracy appears). (c) Extremely narrow beam LWAs can be conceived with EPD coupled transmission lines. (d) Beamwidth varying with different values of mutual capacitance C_m [10].

veniently designing periodic coupled transmission lines it is also possible to theoretically observe fourth order degeneracy [7]. Figure 2.5 shows that the periodic structure unit cell is made of a modulated line coupled to a uniform microstrip by means of a metal connection. Also in this case gain is needed to retrieve the EPD, but degeneracy can be achieved even if no perfect PT symmetry is respected. The DD obtained is meaningful for an infinite structure only. Experimental demonstration of the dispersion diagram exhibiting four quasi-coalescing eigenmodes have been reported. To obtain resonance close to EPD frequencies, th realisation of a discrete structure requires enough cascaded unit cells. The effect of having finite structure is the shift induced in resonance frequency. Gain elements are still required induce the EPDs and the design is currently under investigation [27].

Some coupled structures such as coupled resonator optical waveguides (CROW) also exhibit the possibility to sustain second, third, fourth and even sixth order EPDs, depending on the employed design [4]. The added value of this device, showed in figure 2.2b, is the possibility to induce EPDs without the need of satisfying gain and loss balance, thus breaking PT symmetry. The proposed geometry consists of a chain of coupled ring resonators with outer radius R. They are coupled side-by-side to a uniform optical waveguide. Coupling is assumed to be present in discrete points , where the rings are close to each other and to the uniform line. By conveniently design the aspect ratio of these structures large Q-factors a giant scaling can be obtained. The word giant is used referring to the anomalous scaling law that can be encountered dealing with geometries supporting DBEs. In particular, in this structures Q-factor is inversely proportional to Floquet-Bloch mode group velocity, i.e. $Qv_g = \text{const}$, therefore, approaching a DBE, where $v_g = 0$ one ideally has $Q = \infty$ as reported in [4].

Lately, also the possibility to have EPDs induced by time-varying parameters, rather has been proposed in [13]. A recent practical application of EPDs

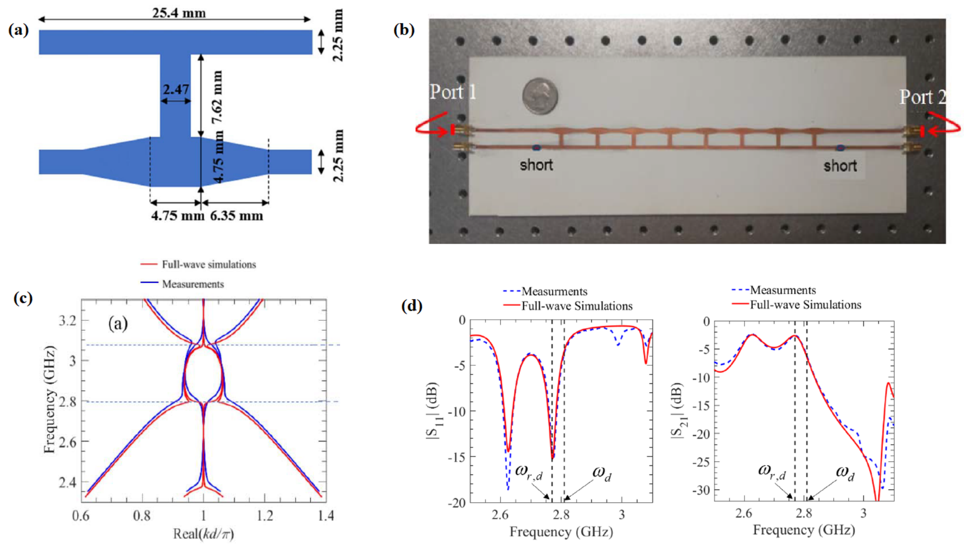

Figure 2.5: Design proposed in [7]: (a) unit cell, (b) realised discrete periodic structure, (c) simulation and measurement of dispersion diagram, (d) shift from ω_d in reflection and transmission parameters.

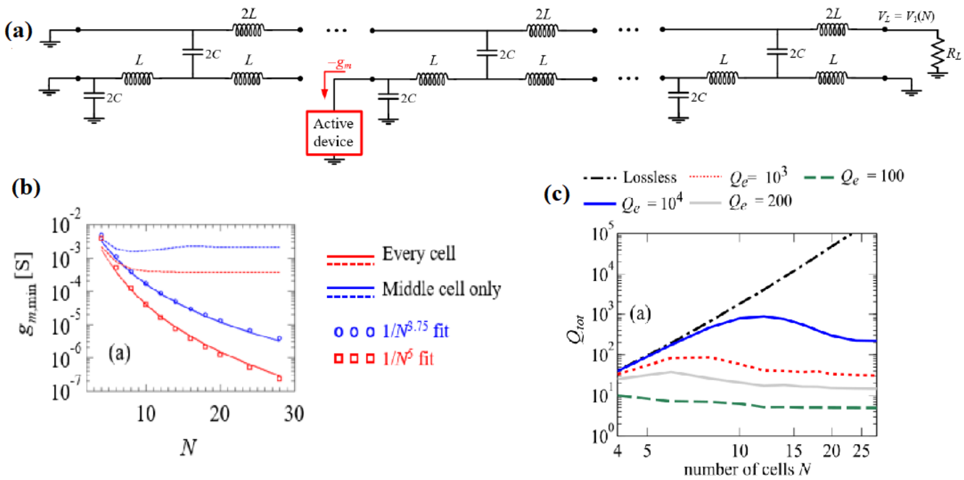

Figure 2.6: (a) Double ladder oscillator realised in [6]. (b) Minimum driving admittance scales as $1/N^5$ for DBE structure. (c) Q-factor versus the number of cells for different loads.

is reported in [6], where a double ladder oscillator is realised using lumped elements (figure 2.6). Moreover single and double ladder are compared. A gain element is introduced at the node in which the driving point impedance is minimum, compensating for losses and guaranteeing oscillation. Being a double ladder, this structure support four modes. In particular, thank to DBE the double ladder presents also some enhanced features with respect the single ladder, such as:

- Minimum value of the driving point impedance proportional to $1/N^5$.
- Total quality factor proportional to N^5 (with maximum value proportional to 10^4).

- Lower oscillation threshold compared to a single ladder structure.
- Strong reduction of mode jumping, meaning that the oscillation frequency is independent on the load value.

Currently a printed elements variant of the circuit is under investigation. Even if this application is particularly well suited for low power (low threshold) and low noise purposes (large Q-factor, [28]), EPDs can be also exploited in high power applications such as distributed backward wave oscillators [5].

2.2 THESIS MOTIVATION

Even if the presence of EPDs is known since the last two decades [16], [18], [19], a recent research interest in EPDs has arised in a number of applications, spanning from particles sensing [11] ad high transmission gain FPC lasers in optics [2] to narrow beam antennas [10] and high power electron beams [5], [12] in electronics. Many recently published papers have laid the foundation and the formalism to better understand how to engineer and recognise the presence of an EPD [4], [6], [7], [10], [13].

As mentioned in the previous section, in many application related to radiofrequency, microwave electronics and optics the presence of EPDs is a benefit. Many of the properties related to devices operation may be enhanced because of the coalescence of system eigenmodes, paving the way to a new class of sensors, filters, pulse forming networks. In particular, the dramatic reduction of group velocity and the increase in loaded quality factor is a crucial enhancement in the realization of novel oscillator schemes in which giant resonance and ultra high spectral purity are both present, along with low oscillation thresholds and load effect minimization.

Although some example of EPD oscillators can be found in literature [6], [12], they are mainly based DBE and usually designed as periodic structures of lumped elements or in bulky hollow metallic waveguides. Moreover, no mention to radiation properties in this devices has been highlighted till now.

The aim of this Thesis is to study new single ladder oscillator schemes based on EPDs in a simple monolithic microstrip technology, analysing how the main figures of merit behave with respect design parameters and demonstrating, if possible, the evidence of exceptional points of degeneracy. Furthermore, the design is oriented toward topologies also able to provide radiation, in order to verify if oscillation and radiation may be concurrently present in an EPD system.

Part II

THEORETICAL BACKGROUND

3 RF AND MW RESONATORS

3.1 SERIES AND PARALLEL RESONANT CIRCUITS

RF and microwave resonators are widely employed in the design of filters, frequency meters, tuned amplifiers and oscillators [9]. Although these circuits undergoes to distributed parameters circuit theory in short wavelength regime, their working principles are very similar to those of series and parallel lumped *RLC* circuits. Figure 3.1 and figure 3.2 show two basic circuit of series and parallel resonator respectively.

3.1.1 Series resonant circuits

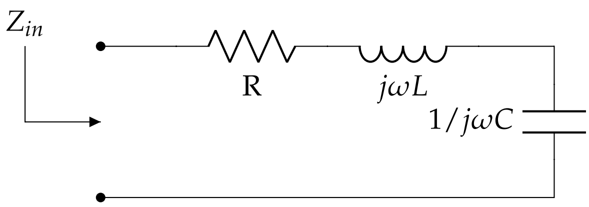

Figure 3.1: Series RLC resonator.

Looking at figure 3.1, the input impedance is given by:

$$Z_{in} = R + j\omega L - j\frac{1}{\omega C} \tag{3.1}$$

with complex power delivered equal to:

$$\begin{aligned} P_{in} &= \frac{1}{2}VI^* = \frac{1}{2}|I|^2\left(R + j\omega L - j\frac{1}{\omega C}\right) \\ &= P_{loss} + 2j\omega(W_m - W_e) \end{aligned} \tag{3.2}$$

where $P_{loss} = \frac{1}{2}|I|^2 R$ is the power dissipated by the resistor, $W_e = \frac{1}{4}|I|^2\frac{1}{\omega^2 C}$ is the total electric energy stored in C and $W_m = \frac{1}{4}|I|^2 L$ is the total magnetic energy stored by the inductor. Substituting 3.2 in 3.1 and recalling that resonance appear when $W_m = W_e$, on has:

$$Zin = \frac{P_{loss} + 2j\omega(W_m - W_e)}{\frac{1}{2}|I|^2} = R \tag{3.3}$$

Moreover, having $W_m = W_e$ one has the resonant pulsation defined as $\omega_0 = 1/\sqrt{LC}$.

An important figure of merit is the resonant circuit *quality factor*, Q, defined as:

$$\begin{aligned} Q &= \omega \frac{\text{average stored energy}}{\text{power loss}} \\ &= \omega \frac{W_m + W_e}{P_{loss}} \end{aligned} \tag{3.4}$$

From which it appears that the higher is the loss the lower is Q. At resonance, if no additional resistive loads are connected to the resonator, Q has the maximum possible value and it is called *unloaded* Q, denoted by Q_0. In fact:

$$Q_0 = \omega_0 \frac{2W_m}{P_{loss}} = \frac{\omega_0 L}{R} = \frac{1}{\omega_0 RC} \tag{3.5}$$

Next, considering a small variation from ω_0 given by $\omega = \omega_0 + \Delta\omega$ one can rewrite Z_{in} as:

$$Z_{in} = R + j\omega L \left(\frac{\omega^2 - \omega_0^2}{\omega^2} \right) \simeq R + j \frac{2RQ_0 \Delta\omega}{\omega_0} \tag{3.6}$$

We can finally define the *half-power fractional bandwidth* as the bandwidth at which the power is 3dB below the power delivered at resonance. At this condition $\omega_0 \pm BW/2$, then $\Delta\omega/\omega_0 = BW/2$ and:

$$\begin{aligned} |Z_{in}|^2 &= 2R^2 \\ |R + jRQ_0(BW)|^2 &= 2R^2 \\ BW &= \frac{1}{Q_0} \end{aligned} \tag{3.7}$$

A series resonant circuit acts as a stop band filter at pulsation ω_0 [9].

3.1.2 Parallel resonant circuits

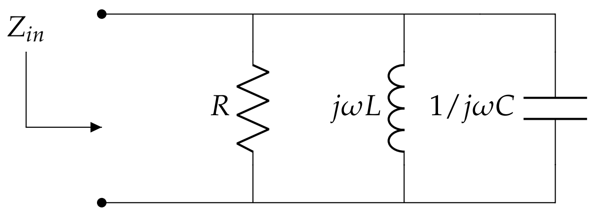

Figure 3.2: Parallel RLC resonator.

Looking at figure 3.2, the input impedance is given by:

$$Z_{in} = Y_{in}^{-1} = \left(\frac{1}{R} + \frac{1}{j\omega L} - j\omega C \right)^{-1} \tag{3.8}$$

Given $P_{loss} = \frac{1}{2}\frac{|V|^2}{R}$ the power dissipated by the resistor, $W_e = \frac{1}{4}|V|^2 C$ the total electric energy stored in C and $W_m = \frac{1}{4}\frac{|V|^2}{\omega^2 L}$ the total magnetic energy stored by the inductor, one has at resonance (or *antiresonance*):

$$Zin = \frac{P_{loss} + 2j\omega(W_m - W_e)}{\frac{1}{2}|I|^2} = R \tag{3.9}$$

The unloaded quality factor at antiresonance $\omega_0 = 1/\sqrt{LC}$ is given by:

$$Q_0 = \omega_0 \frac{2W_m}{P_{loss}} = \frac{R}{\omega_0 L} = \omega_0 RC \tag{3.10}$$

Close to resonance the input impedance can be approximated as follows:

$$Z_{in} \simeq \frac{R}{1 + j2Q_0\Delta\omega/\omega_0} \tag{3.11}$$

Moreover the half-power fractional bandwidth is $BW = 1/Q_0$.

3.1.3 Loaded and unloaded Q-factor

The addition of a series or a parallel load R_L has the effect of lowering the total resonator Q-factor, which takes the name of *loaded Q*, or Q_L. If a series connection of a load with a RLC resonator is present then *external Q* is given by:

$$Q_e = \frac{\omega_0 L}{R_L} \tag{3.12}$$

whereas, in case of parallel RLC group Q_e is:

$$Q_e = \frac{R_L}{\omega_0 L} \tag{3.13}$$

The total loaded quality factor is thus:

$$Q_L = \left(\frac{1}{Q_e} + \frac{1}{Q_0}\right) \tag{3.14}$$

3.1.4 The Coupling Coefficient and Critical Coupling

With *coupling* it is intended how much a resonator is matched to its attached circuitry and how effective is the power transfer between them (not to be confused with coupling in coupled transmission lines). A measure of the amount of coupling is given by the *coupling coefficient*, defined as:

$$g = \frac{Q_0}{Q_e} \tag{3.15}$$

Depending on the two Q-factors three conditions can hold:

- $g < 1$: *undercoupled* resonator.
- $g = 1$: *critically coupled* resonator.
- $g > 1$: *overcoupled* resonator

Moreover, the loaded Q-factor is:

$$Q_L = \frac{Q_0}{1+g} = Q_e \frac{g}{1+g} \tag{3.16}$$

Power transfer is maximum provided that a resonator is matched with its feeding line at resonance frequency. The resonator is said critically coupled if this happens [9] . Moreover, it is possible to define the normalized frequency shits corresponding to the quality factors as:

$$\delta_0 = \pm\frac{1}{Q_0} \qquad \delta_L = \pm\frac{1}{Q_L} \qquad \delta_e = \pm\frac{1}{Q_e} \tag{3.17}$$

3.2 INTERDIGITATED CAPACITOR AS RESONANT UNIT

Electromagnetic coupling between closely placed lines can be exploited to obtain capacitors in printed technology (figure 3.3a shows an example). Several strips (fingers) are put in parallel separated by a thin gap in order to form a periodic structure whose electrical parameters are dispersive and nonlinear functions of the number of coupled elements. The advantage of printed capacitors is that they can be fabricated in monolithic microwave integrated circuits (MMIC), besides the possibility to have higher quality factors [29]. Actually, the model describing this kind of devices is quite complex, [30][29] therefore only the main approximated results are shown here. Supposing to having a microstrip technology operating in sub-wavelength

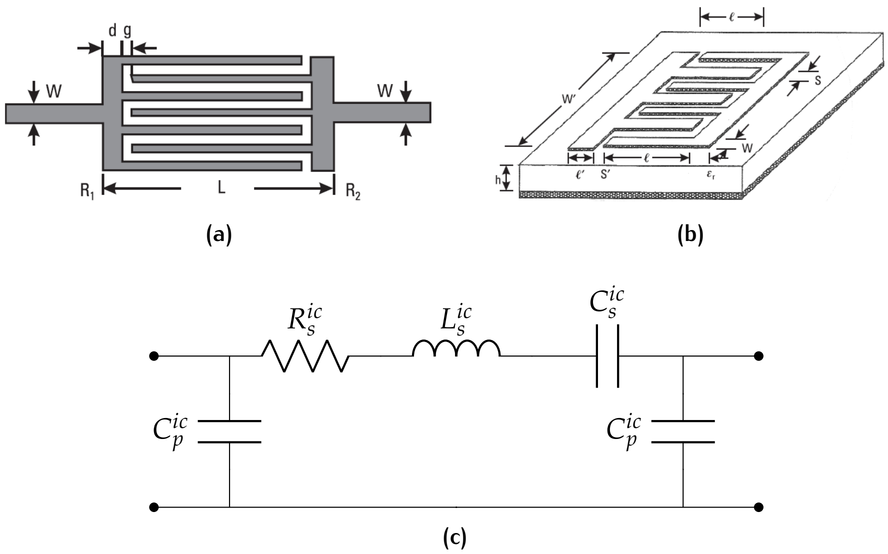

Figure 3.3: (a) Printed interdigital capacitor in microstrip technology with microstrip access lines [29]. (b) Interdigital capacitor design parameters [29]. (c) Interdigital capacitor equivalent circuit.

regime whose parameters are defined in figure 3.3b, a possible equivalent circuit that describes a center-tap interdigitated capacitor, CIDC, is shown in figure 3.3c. The circuit is valid for low frequency, in order to consider the circuit as lumped. Having a substrate with thickness h, dielectric relative permittivity ϵ_r and N fingers with length $l < \lambda_0/4$, the total gap capacitance is given by:

$$C_s^{ic} = (\epsilon_r + 1)l[(N-3)A_1 + A_2] \quad \text{(pF)} \tag{3.18}$$

where:

$$A_1 = 4.409 \tanh\left[0.55\left(\frac{h}{W}\right)^{0.45}\right] \times 10^{-6} \quad pF/\mu m \tag{3.19a}$$

$$A_2 = 9.92 \tanh\left[0.52\left(\frac{h}{W}\right)^{0.5}\right] \times 10^{-6} \quad pF/\mu m \tag{3.19b}$$

Instead, for what concerns the series resistance R is:

$$R_s^{ic} = \frac{4}{3}\frac{l}{WN}R_{sq} \tag{3.20}$$

where R_{sq} is the sheet resistivity in ohms per square for the employed conductor used in the technology. Series inductance L_s^{ic} and shunt capacitance C_p^{ic} are calculated through transmission line theory:

$$L_s^{ic} = \frac{Z_0\sqrt{\epsilon_{re}}}{c} l \tag{3.21a}$$

$$C_p^{ic} = \frac{1}{2}\frac{\sqrt{\epsilon_{re}}}{Z_0 c} l \tag{3.21b}$$

It is now useful to notice that the circuit in figure 3.3c is the Π-equivalent of the interdigital capacitor, with components:

$$Y_{\Pi 1}^{ic} = Y_{\Pi 2}^{ic} = j\omega C_p^{ic} \tag{3.22a}$$

$$Y_{\Pi 3}^{ic} = \frac{j\omega C_s^{ic}}{1 + j\omega C_s^{ic} R_s^{ic} - \omega^2 L_s^{ic} C_s^{ic}} \tag{3.22b}$$

whose associated Y matrix is given by [31]:

$$\underline{\mathbf{Y}}_{\Pi}^{ic} = \begin{pmatrix} Y_{11}^{ic} & Y_{12}^{ic} \\ Y_{21}^{ic} & Y_{22}^{ic} \end{pmatrix} = \begin{pmatrix} Y_{\Pi 1}^{ic} + Y_{\Pi 3}^{ic} & -Y_{\Pi 3}^{ic} \\ -Y_{\Pi 3}^{ic} & Y_{\Pi 1}^{ic} + Y_{\Pi 3}^{ic} \end{pmatrix} \tag{3.23}$$

where:

$$Y_{11}^{ic} = Y_{22}^{ic} = \frac{j\omega(C_s^{ic} + C_p^{ic}) - \omega^2 R_s^{ic} L_s^{ic} C_p^{ic} - j\omega^3 L_s^{ic} C_s^{ic} C_p^{ic}}{1 + j\omega R_s^{ic} L_s^{ic} - \omega^2 R_s^{ic} L_s^{ic}} \tag{3.24a}$$

$$Y_{12}^{ic} = Y_{21}^{ic} = -\frac{j\omega C_s^{ic}}{1 + j\omega C_s^{ic} R_s^{ic} - \omega^2 L_s^{ic} C_s^{ic}} \tag{3.24b}$$

for which transformation to transmission matrix parameters can be easily performed following well known conversion rules [9]. The quality factor Q^{ic} and the series resonance frequency $f_s e$ for the resonator are given by:

$$Q_c^{ic} = \frac{1}{\omega C_s^{ic} R_s^{ic}} = \frac{3WN}{\omega C_s^{ic} 4 l R_{sq}} \tag{3.25a}$$

$$f_{se} = \frac{1}{2\pi\sqrt{L_s^{ic} C_s^{ic}}} \tag{3.25b}$$

Depending on the interdigitated capacitor area and number of fingers, the obtainable value of series capacitances and inductances are around hundreds of fF and pH, respectively. Usually these devices are treated as lumped elements in the majority of their applications, a part for some special cases, such as J-inverter networks used for filtering purposes [29]. Being sub-wavelength, many loss contributions can be neglected, such as radiation losses. However, conduction loss is kept into account through R_s, even if it can be minimized by increasing the number of fingers. This also produces an increment in the series capacitance. However, the capacitor could be employed as unit cell in periodic structures. In this case, radiation could be present since electromagnetic properties, would depend on the topology of the new circuit rather than the single element.

The integrated capacitor can be used as unit cell resonanting element in a microstrip resonator. To do so, it must obviously connected to two microstrip access line. Transmission matrix satisfy the group property, therefore, given the series cascade of two two-ports whose transmission matrix are $\underline{\mathbf{T}}_A(z_0, z_1)$ and $\underline{\mathbf{T}}_B(z_1, z_2)$, the overall transmission matrix is defined as $\underline{\mathbf{T}}_{tot}(z0, z2) = \underline{\mathbf{T}}_B(z_1, z_2)\underline{\mathbf{T}}_B(z_1, z_2)$. Therefore, by connecting the interdigital capacitor, transmission parameters $\underline{\mathbf{T}^{\mathbf{ic}}}$, to two access lines whose T-matrix is $\underline{\mathbf{T}^{\mathbf{tl}}}$one has:

$$\underline{\mathbf{T}} = \underline{\mathbf{T}^{\mathbf{tl}}\mathbf{T}^{\mathbf{ic}}\mathbf{T}^{\mathbf{tl}}} \tag{3.26}$$

where the expression and the derivation for $\underline{\mathbf{T}^{\mathbf{tl}}}$ is reported for simplicity in appendix D. The complete circuit representing the cascade of the three blocks is reported in figure 3.4.

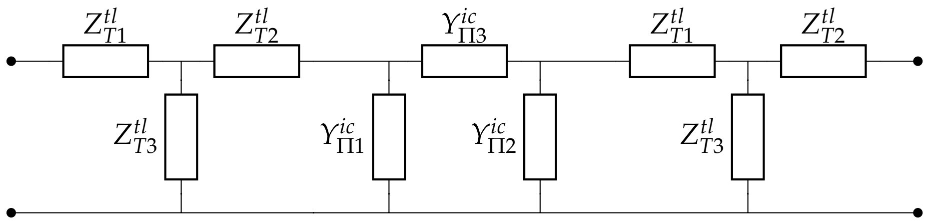

Figure 3.4: Equivalent $T - \Pi - T$ circuit for a microstrip interdigital capacitor provided with access lines.

4 RF AND MW OSCILLATORS

4.1 KUROKAWA'S CRITERIA FOR OSCILLATION

Oscillators are nonlinear circuits in which the interplay between an active device and a resonating circuit produces as a result an output waveform whose frequency content and amplitude are fixed by the circuit itself. In particular, the purer is the output spectrum (ideally one-tone), the better is the oscillator performances.

Usually, this kind of system can be described as an amplifier circuit in which part of the output energy is fed back though the feedback loop (whose feedback gain is F) to the active device (with open-loop gain A) in phase with the input signal. The linear feedback circuit has closed-loop gain:

$$A_v = \frac{V_o}{V_i} = \frac{A}{1 - AF} \tag{4.1}$$

The simpler requirement to have a stable oscillation without waveform dumping or saturation is the Barkhausen stability criterion on loop gain AF [32], that reduces to:

$$|AF| = 1 \tag{4.2a}$$

$$\arg(AF) = 2n\pi, \quad n = 0, 1, 2 \ldots \tag{4.2b}$$

Therefore the loop gain must be unitary and the loop phase equals zero, guaranteeing the presence of a pole of the transfer function right half-plane (unstable region). However, the presence of a pole in the unstable region only allows any perturbation or noise to start-up a sinusoidal oscillation that exponentially diverges to infinite amplitude. A more detailed analysis requires to keep into account nonlinear behaviour too, that are in fact responsible of gain saturation. In fact, this phenomenon self limits the output and decreases (increases) the gain in which 4.2 are satisfied, self-regulating the process.

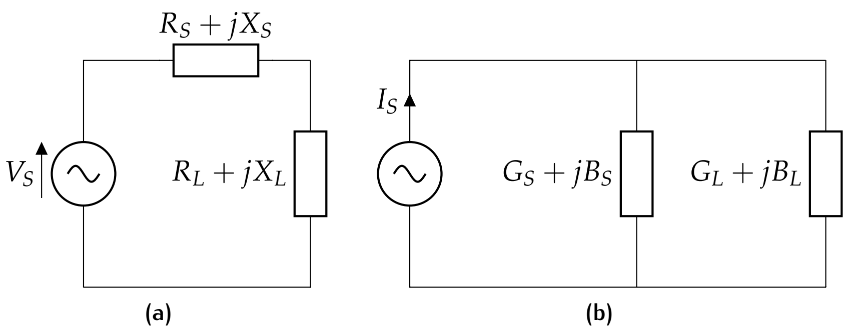

Figure 4.1: Negative resistance (a) series and (b) parallel oscillator circuit model.

To have a simpler and complete description of the system under analysis, Kurokawa introduced the concept of negative resistance oscillators [33].

Figure 4.1a and 4.1b represent the model of a one-port negative resistance oscillator,in series and parallel configuration respectively. It is possible to distinguish two sides, namely: the active device (on the left) and the frequency selective load, that is a resonator, on the right. The active device can represent a two-port solid state device, such a Gunn or a tunnel diode, exhibiting negative output conductance in some working regions [34]. Other possibilities include the use of operational amplifier in negative resistance configuration or FET equipped with a phase inversion network [32].

Referring to figure 4.1a, the load impedance $Z_L(I_0, j\omega) = R_L(I_0, j\omega) + X_L(I_0, j\omega)$ is linear, whereas the active device output impedance $Z_S(I_0, j\omega) = R_S(I_0, j\omega) + X_S(I_0, j\omega)$ is in general nonlinear with respect the fundamental current component I_0. Both the quantities also linearly depend on frequency. Z_S can be considered linear with respect I if the current high order harmonics are weakly effective in the source output waveform. A first necessary condition to have oscillation [9] in the circuit is:

$$R_L(I_0, j\omega_0) + R_S(I_0, j\omega_0) = 0 \tag{4.3a}$$

$$X_L(I_0, j\omega_0) + X_S(I_0, j\omega_0) = 0 \tag{4.3b}$$

Usually start-up requires $|R_S| > 1.2R_L$ [28]. Since load is a passive device with $R_L > 0$, implying energy dissipation, the condition $R_S < 0$ must be satisfied, meaning that the source is providing energy to the system. Given the start-up oscillation frequency ω_p, it is initially necessary that $R_L + R_S(I, j\omega_p) < 0$. The condition suggests that the system is unstable at start-up and it eventually encounters a transient due to noise or a given external excitations. As the current I increases, $|R_S|$ decreases, stabilizing to a value of current I_0, that finally brings the circuit to steadily oscillate at $\omega_0 \neq \omega_p$. The drop of $|R_S|$ is a necessary condition, since, waveforms cannot reach infinite amplitude as I_0 rises. The difference in the final frequency is due to the resonator reactance, that is both current dependent and responsible of selecting the oscillation frequency ($X_S(I_{osc}, j\omega_{osc}) \neq X_S(I_0, j\omega_0)$).

Figure 4.1b shows the equivalent parallel model of a negative resistance oscillator. Here, it is possible to distinguish two sides, namely: the active device, whose input admittance is $Y_S(V, j\omega) = G_S(V, j\omega) + B_S(V, j\omega)$ and the frequency selective load, embodied by $Y_L(V, j\omega) = G_L(V, j\omega) + B_L(I, j\omega)$. In this case, the condition to have oscillation is given by:

$$G_L(V_0, j\omega_0) + G_{in}(V_0, j\omega_0) = 0 \tag{4.4a}$$

$$Y_L(V_0, j\omega_0) + Y_{in}(V_0, j\omega_0) = 0 \tag{4.4b}$$

Usually start-up requires $|G_S| > 1.2G_L$ [28]. A stable oscillation is only ensured by systems where every perturbation is dumped out. In practice active device reactive impedance (admittance) reactive components are due to parasitic that often happen to be nonlinear with respect to device operating point [35]. The behaviour of this elements is known, not the exact value though, meaning that conditions 4.3b and 4.4b could be valid for frequency other than ω_0. However the use of high-Q resonators makes this effect often negligible [32], since ImZ_L rapidly vary close to resonance avoiding frequency deviations. Another condition to determine if the oscillation is stable at a given

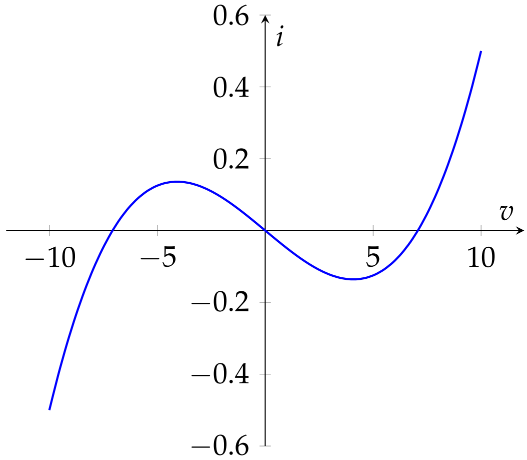

Figure 4.2: Example of V-I non linear third order characteristic around a given bias point.

frequency, is proposed by Kurokawa [9] and demonstrated in Appendix A. It gives:

$$\frac{\partial R_S}{\partial I}\frac{\partial}{\partial \omega}(X_L + X_S) - \frac{\partial X_L}{\partial \omega}\frac{\partial R_S}{\partial I} > 0 \tag{4.5}$$

The condition 4.5 is valid, provided that Z_L (Y_L) is slow varying with respect to the current (voltage). Since $\partial R_S/\partial I > 0$ and $\partial X_L + X_S/\partial I >> 0$ the result is always verified if resonator quality factor is large, confirming what is stated above. It is important to notice that the concept of *stability* has not to be intended in its classical significance. In this case - and only with nonlinear circuits - the whole system is unstable in order to allow oscillation and the effort is focused in obtaining a bounded waveform, whose magnitude returns to its steady state even if perturbations appear.

Equivalent conditions for oscillation can be derived by using scattering parameters measured at the source output port and reflection coefficient at the input of the tank, S'_{11} and Γ_L respectively [28]. Having:

$$S'_{11} = \frac{R_S + jX_S - Z_0}{R_S + jX_S + Z_0} \tag{4.6}$$

$$\Gamma_L = \frac{R_L + jX_G - Z_0}{R_L + jX_G + Z_0} \tag{4.7}$$

then, if 4.3 holds:

$$\Gamma_L S'_{11} = \frac{-R_L - jX_L - Z_0}{-R_L - jX_L + Z_0} \cdot \frac{R_L + jX_G - Z_0}{R_L + jX_G + Z_0} = 1 \tag{4.8}$$

4.2 NEGATIVE RESISTANCE FROM ACTIVE ELEMENTS

The modelling of the source into oscillators often require to consider that as a two-port network. This two port needs to be unstable in the classical sense and many well known stability criteria such as the, Nyquist, k-Δ_S or the two μ parameters model [36] . The alternative approach is to consider diodes, transistors or other active circuits as one-port networks with negative output conductance or resistance.

Regardless of the two-terminal circuit, that can be described as controlled generator or a non linear resistor, the required output V-I in case of negative output resistance device is:

$$v(t) = I_0 - r_m(I_0)i(t) + \alpha_{nr}(I_0)i(t)^3 - \beta_{nr}(V_0)i(t)^5 + \dots \quad (4.9)$$

whereas for negative output conductance devices the I-V relations is expressed as:

$$i(t) = V_0 - r_m(V_0)i(t) + \alpha_{nc}(V_0)v(t)^3 - \beta_{nc}(V_0)v(t)^5 + \dots \quad (4.10)$$

From figure 4.2 it appears that the output characteristics above, depict the general case in which a circuit is operating around its DC operating point, presenting a odd non linear behaviour. High order terms - larger than the third order - can be in general neglected, unless information about harmonic distortion are required (as in non-linear amplifier design [36]).

4.2.1 Negative Resistance from Tunnelling Diodes

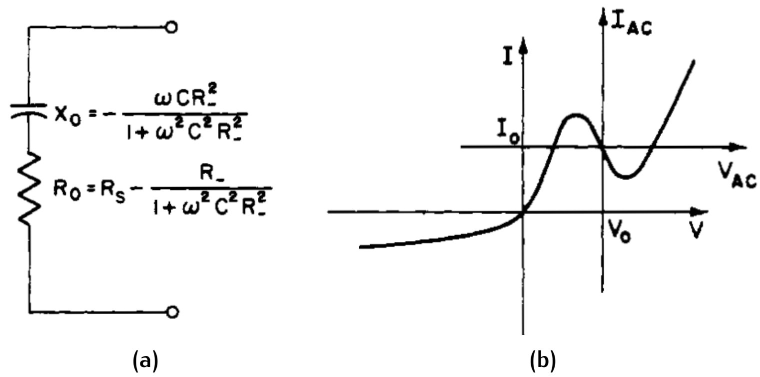

Figure 4.3: (a) Esaki diode small signal equivalent circuit model and (b) output characteristic [37].

Tunnel diodes are elements well suited for RF and low millimeter applications. They are mainly fabricated in GaAs technology and they and the range of application spans from hundreds of MHz to some tens of GHz [28]. *Microwave diodes* are another class of one port semiconductors devices, often used in high frequency applications. Examples of these kind of devices are Gunn diodes, and transit time diodes. In this case oscillation, derives from the built-in physical mechanism rather than the presence positive feedback loops [36].

Esaki diodes main feature regards the output I-V characteristic depicted in figure [tunnel diode IV and equivalents], to which the linear circuit model is associated . In fact, although the diode junction resistance is positive, the differential resistance can be negative for a certain range of input voltages.

The reduced equivalent circuit in figure 4.3 [37] is a series impedance whose real and imaginary parts are:

$$R_O = R_S - \frac{R_-}{1+\omega^2 C^2 R_-^2} \tag{4.11a}$$

$$X_O = -\frac{\omega C R_-^2}{1+\omega^2 C^2 R_-^2} \tag{4.11b}$$

Where R_- is the negative junction resistance and it can be obtained by the diode model itself by calculation at the resistive cutoff frequency, at which R_O becomes null.

4.2.2 Negative Resistance from Transistor Model

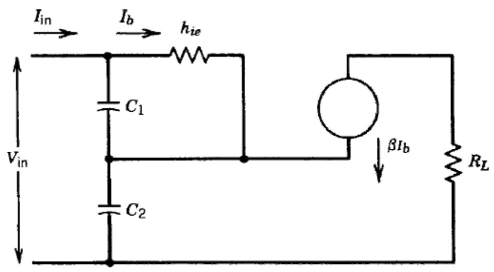

Figure 4.4: Negative resistance BJT with capacitive feedback equivalent circuit.

A feedback loop can be used to provide negative resistance in a circuit with transistors. An example, using a BJT transistor linear model is reported in figure 4.4 where a capacitive loop is employed [28]. In this case the input impedance is:

$$Z_{in} \simeq \frac{-g_m}{\omega^2 C_1 C_2} + \frac{1}{j\omega[C_1C_2/(C_1+C_2)]} \tag{4.12}$$

where, besides $R_{in} = -gm/(\omega^2 C_1 C_2)$ an equivalent series capacitance $C_{in} = C_1C_2/(C_1+C_2)$ appears. BJT transistors are usually preferred in microwave applications, thanks to their superior phase noise characteristic [36].

4.3 Q-FACTOR IN OSCILLATORS

The quality factor of an oscillator strongly depend on the presence of a load, different from a the standard 50 Ω termination. This traduces into an oscillation frequency and phase shift. For an external load whose VSWR is S, oscillation frequency f_0 and frequency deviation Δf, the external quality factor is:

$$Q_{ext} = \frac{f_0}{1\Delta f}\left(S - \frac{1}{S}\right) \tag{4.13}$$

This figure of merit is a measure of the average stored energy into the oscillator circuit and it different from the external Q of the resonator. The definition follows:

$$Q_{ext} = 2\pi \frac{\text{time-averaged stored energy}}{energydeliveredtotheloadpercycle} \tag{4.14}$$

That is different from the definition of Q_L that considers the power dissipated by the whole oscillator per each cycle. Even though the oscillator output power is difficult to predict, it is expected to to be less than the saturated power that the employed active element would have in a large signal amplifier application [28].

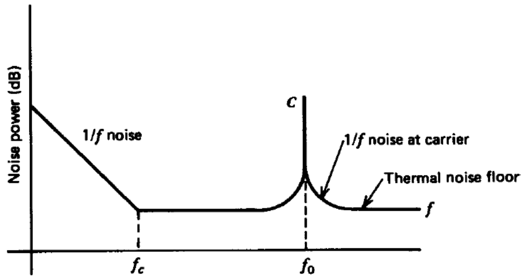

Figure 4.5: Noise power versus frequency for a transistor amplifier operating at frequency f_0 [28].

4.4 NOISE IN OSCILLATORS

Practical oscillators can have short term amplitude and frequency instabilities due to noise. In particular there are:

- Intrinsic noise, mainly due to thermal effect, shot noise and Flicker noise.
- Extrinsic noise, due to power supply and substrate noise.

Real oscillators output waveform suffer both amplitude and phase modulation. Therefore, one has:

$$v_{out} = V_0(1 + A(t)) \cos(\omega_0 t + \varphi(t)) \tag{4.15}$$

Noise can be seen as a random input to the oscillator and can affect the oscillation frequency, modulating the instantaneous working point. Flicker noise is ubiquitous and present in many physical systems. It is associated to a variety of causes [36] and its typical power spectrum is depicted in figure 4.5. This noise, whose law is proportional to $1/f$ is effective until the *corner frequency*, f_c, that is the point at which white (thermal) noise, power spectrum becomes higher. Being f_c around few GHz, Flicker noise is only effective in RF circuits [36]. Diodes offer noise too, mainly due to shot noise, proportional to diode bias and inverse saturation current.

Low frequency noise is up-converted in oscillators. Having a carrier at frequency f_0 and a modulating signal at frequency f_m, two frequency contributions appear at $f_1 = f_0 - f_m$ and $f_2 = f_0 + f_m$ (figure 4.6). A useful formula introduced by Leeson gives the ratio of sideband power in 1 Hz bandwidth at f_m. Sideband power power level is measured from f_0 [28]:

$$L(f_m) = \frac{1}{2}\left[1 + \frac{\omega_0^2}{4\omega_m^2}\left(\frac{P_{in}}{\omega_0 W_e} + \frac{1}{Q_0} + \frac{P_{sig}}{\omega_0 W_e}\right)^2\right]\left(1 + \frac{\omega_c}{\omega_m}\right)\frac{FkT_0}{P_{avs}} \tag{4.16}$$

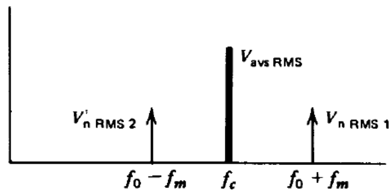

Figure 4.6: Modulation of the oscillation frequency f_c due to phase noise [28].

where: ω_m is the pulsation offset (with respect to the carrier), ω_0 the centre frequency, ω_c the Flicker corner pulsation, Q_0 the unloaded Q, F the noise factor of the transistor, kT the thermal noise per unit bandwidth (at 300 K), P_{avs} the average power at oscillator output, P_{sig} the signal power, P_{in} the input power and $\omega_0 W_e$ the reactive power.

4.5 SOME OSCILLATOR DESIGN CONSIDERATIONS

A part for satisfying Kurokawa's stability and oscillation conditions, some other design considerations can be pointed out [28]:

- Maximize the unloaded Q employng well suited free running sources for the desired frequency band operation.
- Maximize the reactive energy by means of high ac voltage drops across the resonator or by minimizing the LC ratio. The limits are set by the operation limits of the active device.
- Avoid saturation to a prevent Q and spectral purity degradation.
- Choose active devices with a low noise figure.
- High impedance devices such as FETs can minimize phase perturbations.
- Use devices with low corner frequency. Usually BJT are preferred in these applications, since they have a lower corner frequency than FETs. Systems that use feedback benefit of a strong noise reduction.
- Energy should be coupled to the resonator, rather than other parts of the circuit. This allows the resonator to also limit the bandwidth of the circuit, being it a filter.

5 PERIODIC STRUCTURES AND EPDS

One Transmission lines and waveguides if loaded at periodic intervals with identical obstacles are referred as periodic structures. Besides the possibility to have a variety of shapes, these structures are interesting for two aspects [38]:

- Passband and stopband characteristics;
- Capability of supporting slow-waves whose propagation depends on the topology of the whole structure.

A passband is a frequency range in which a wave can propagate without attenuation, whereas stopbands are bands through which wave is cut off and does not propagate.

5.1 INFINITE PERIODIC STRUCTURES

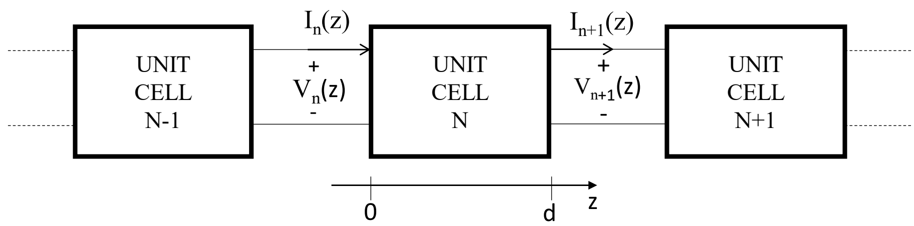

Figure 5.1: Infinite periodic structure blocks model.

First, the propagation of waves in a one dimensional, reciprocal, infinite and periodically loaded line is derived. The basic constitutive element, called *unit cells* have length d. The structure is oriented along the z axis, as depicted in figure 5.1. The line can be considered as a cascade of identical two-ports, modelled by a transmission matrix. Current and voltages at the input and output of a single cell are related as follows:

$$\begin{bmatrix} V_n(\omega) \\ I_n(\omega) \end{bmatrix} = \begin{bmatrix} A(\omega) & B(\omega) \\ C(\omega) & D(\omega) \end{bmatrix} \begin{bmatrix} V_{n+1}(\omega) \\ I_{n+1}(\omega) \end{bmatrix} = \underline{\mathbf{T}} \begin{bmatrix} V_{n+1}(\omega) \\ I_{n+1}(\omega) \end{bmatrix} \tag{5.1}$$

For a reciprocal network, the T-matrix determinant is unitary, [9] therefore $det(\underline{\mathbf{T}}) = AD - BC = 1$, the matrix $\underline{\mathbf{T}}$ is non singular and diagonalizable. Being a piece of transmission line, the two-port supports wave propagating in both forward and backward direction, with complex propagation constant $\pm\gamma(\omega)$. The + sign stands refers to backward propagation, whereas the minus sign refers to forward propagation. Moreover, since the structure is periodic, voltages and current will be periodic as well passing from the n-th to the n+1-th cell. Supposing to start the propagation from the initial position $z = 0$, one has the following boundary condition:

$$V(z, \omega) = V(0)e^{-\gamma(\omega)z} \tag{5.2a}$$

$$I(z, \omega) = I(0)e^{-\gamma(\omega)z} \tag{5.2b}$$

Therefore after passing n cells of length d:

$$V_{n+1}(\omega) = V_n(\omega)e^{-\gamma(\omega)d} \tag{5.3a}$$

$$I_{n+1}(\omega) = I_n(\omega)e^{-\gamma(\omega)d} \tag{5.3b}$$

The propagation constant $\gamma = \alpha + j\beta$ takes into account both the harmonic (periodic) and lossy behaviour of the line, with β and α respectively. Notice, from now on all the quantities will be considered function of frequency ω, so for the sake of simplicity the notation $f(\omega)$ will be drop. Obtaining V_n and I_n from 5.3 and substituting into 5.1, one has:

$$\underline{\mathbf{T}} \begin{bmatrix} V_{n+1} \\ I_{n+1} \end{bmatrix} = \begin{bmatrix} V_{n+1}e^{\gamma d} \\ I_{n+1}e^{\gamma d} \end{bmatrix} = e^{\gamma d} \begin{bmatrix} V_{n+1} \\ I_{n+1} \end{bmatrix} \tag{5.4}$$

Therefore, by defining:

$$\psi_{n+1}(\omega) = \begin{bmatrix} V_{n+1}(\omega) \\ I_{n+1}(\omega) \end{bmatrix} \qquad \lambda_{\pm}(\omega) = e^{\pm\gamma(\omega)d}$$

the following 2×2 eigenvalue problem is obtained:

$$\underline{\mathbf{T}}(\omega)\psi_n(\omega) = \lambda(\omega)\underline{\mathbb{I}}\psi_n(\omega) \tag{5.5}$$

where ψ_n is the state vector, $\lambda_{\pm}$ is the eigenvalue of the system and $\underline{\mathbb{I}}$ is the 2×2 identity matrix. Moreover, the transfer matrix satisfy the group property $\underline{\mathbf{T}}(z_2, z_0) = \underline{\mathbf{T}}(z_2, z_1)\underline{\mathbf{T}}(z_1, z_0)$, the symmetric property $\underline{\mathbf{T}}(z_1, z_0)\underline{\mathbf{T}}(z_0, z_1) = \underline{\mathbb{I}}$ and the J-unitary property:

$$\underline{\mathbf{T}}^{\dagger}(z_1, z_0) = \underline{\mathbf{J}}\underline{\mathbf{T}}^{-1}(z_1, z_0)\underline{\mathbf{J}}, \qquad \underline{\mathbf{J}} = \underline{\mathbf{J}}^{-1} = \underline{\mathbf{J}}^{\dagger} = \begin{bmatrix} 0 & 1 \\ 1 & 0 \end{bmatrix} \tag{5.6}$$

that comes from the reciprocity restriction on the two-port [10]. Being the two-port reciprocal, the system is diagonalizable. Given that, the matrix **T** can also be rewritten in term of its similarity transformation as:

$$\underline{\mathbf{T}} = \underline{\mathbf{U}\boldsymbol{\Lambda}\mathbf{U}}^{-1} \tag{5.7}$$

where:

$$\underline{\mathbf{U}} = \begin{bmatrix} V_{e-} & V_{e+} \\ I_{e-} & I_{e+} \end{bmatrix} \qquad \underline{\boldsymbol{\Lambda}} = \begin{bmatrix} e^{-\gamma d} & 0 \\ 0 & e^{+\gamma d} \end{bmatrix}$$

Where **U** is a nonsingular transformation matrix. The columns of this matrix represent the set of two column eigenvectors $[\psi_{e-}, \psi_{e+}$ that form one orthonormal basis for the system. They are defined as follows:

$$\psi_{e-}(\omega) = \begin{bmatrix} V_{e-}(\omega) \\ I_{e-}(\omega) \end{bmatrix} \qquad \psi_{e+}(\omega) = \begin{bmatrix} V_{e+}(\omega) \\ I_{e+}(\omega) \end{bmatrix}$$

Each normalized eigenvector also represent the voltage and current eigenmodes that can propagate along the line. Since they are associated to their relative eigenvalues - i.e. to their propagation constants - it is possible to notice that: ψ_{e-} is a forward propagating mode related to $\lambda_- = e^{-\gamma d}$ and ψ_{e+} is a forward propagating mode related to $\lambda_+ = e^{+\gamma d}$. To solve the eigenvalue problem in 5.5 the characteristic polynomial is derived:

$$(\underline{\mathbf{T}} - \lambda \underline{\mathbb{I}})\psi_n = 0 \tag{5.8}$$

Excluding the trivial solution $\psi_n = 0$, one has:

$$\begin{aligned}
\det(\underline{\mathbf{T}} - \lambda \underline{\mathbb{I}}) = \begin{vmatrix} A - e^{\gamma d} & B \\ C & D - e^{\gamma d} \end{vmatrix} &= 0 \\
AD + e^{2\gamma d} - (A+D)e^{\gamma d} - BC &= 0 \\
e^{2\gamma d} - tr(\underline{\mathbf{T}})e^{\gamma d} + det(\underline{\mathbf{T}}) &= 0
\end{aligned}$$

where $tr(\underline{\mathbf{T}}) = A + D$ si the matrix trace and $det(\underline{\mathbf{T}}) = 1$. Then:

$$e^{2\gamma d} - tr(\underline{\mathbf{T}})e^{\gamma d} + 1 = 0 \tag{5.9a}$$

$$\begin{aligned}
e^{\gamma d} + e^{-\gamma d} &= tr(\underline{\mathbf{T}}) \\
\cosh \gamma d &= \frac{tr(\underline{\mathbf{T}})}{2}
\end{aligned}$$

$$\cosh \alpha d \cos \beta d + j \sinh \alpha d \sin \beta d = \frac{tr(\underline{\mathbf{T}})}{2} \tag{5.9b}$$

Alternatively it is possible to solve for 5.9a as follows, looking for the roots of the second order polynomial:

$$e^{\pm\gamma(\omega)d} = \frac{tr(\underline{\mathbf{T}}(\omega)) \pm \sqrt{tr(\underline{\mathbf{T}}(\omega))^2 - 4}}{2} \tag{5.10}$$

The right-hand side in 5.9ab is in general a complex quantity. In that case $\alpha \neq 0$ and $\beta \neq 0$. However, if $tr(\underline{\mathbf{T}})$ is real two cases exist:

- $\alpha = 0, \beta \neq \pi$: this case correspond to a non attenuated propagating wave (no loss), defining the pass band of the periodic structure. Moreover, equation 5.9ab reduces to:

$$\cos \beta d = \frac{tr(\underline{\mathbf{T}})}{2} = \frac{A+D}{2} \in \mathrm{Re} \tag{5.11}$$

  Since $|\cos \beta d| = |(A+D)/2| \leq 1$, thus:

$$|A + D| \leq 2 \Rightarrow \text{no attenuation} \tag{5.12}$$

  that is the condition for a two-port to allow propagation without attenuation, meaning that either the two-port does not contain resistances or positive and negative resistance are balanced so that the overall resistance is null ($A = D^*$). If no loss is present, it can be proved that both A and D are real, whereas B and C are both imaginary quantities [39].

- $\alpha \neq 0$, $\beta = 0, \pi$: this condition defines the stop band of the periodic structure. Power is reflected back rather than dissipated and 5.9ab reduces to:

$$\cosh \alpha d = \left| \frac{tr(\underline{\mathbf{T}})}{2} \right| \geq 1 \tag{5.13}$$

  which has solutions for positively travelling waves, $\alpha > 0$, and backward travelling waves, $\alpha < 0$.

It is important to notice that voltages and currents defined by 5.4 are defined only if measured at the terminals of the unit cell. Under this assumption the structure has similar properties to any uniform transmission line. Wave having this behaviour in periodic structures are called *Bloch waves* [38] .

It is also possible to define a characteristic impedances for these waves, the *Bloch impedance*:

$$Z_{BL}(\omega) = Z_0 \frac{V_n(\omega)}{I_n(\omega)} \tag{5.14}$$

where V_n and I_n are normalized quantities. To obtain Z_{BL} the system 5.5 is solved for the state vector ψ_n:

$$(A - e^{\gamma d})V_n + BI_n = 0$$
$$CV_n + (D - e^{\gamma d})I_n = 0$$

that, from the first equation, yields:

$$\frac{V_n}{I_n} = -\frac{B}{A - e^{\gamma d}} = -\frac{D - e^{\gamma d}}{C}$$

hence, in two equivalent forms:

$$Z_{BL}^{\pm} = Z_0 \frac{2B}{tr(\underline{\mathbf{T}}) \pm \sqrt{tr(\underline{\mathbf{T}})^2 - 4}} \tag{5.15}$$

$$Z_{BL}^{\pm} = Z_0 \frac{1}{C} \left[\frac{1}{2}(A - D) \pm j\sqrt{1 - \frac{1}{4}(A + D)^2} \right] \tag{5.16}$$

That are the general expressions for the two Z_B referring to the forward mode (+) and backward mode (-). The two quantities are in general different, provided that the network is asymmetrical. On the contrary, if the network is reversible one has $A = D$ and then:

$$Z_{BL}^{\pm}(\omega) = \frac{\pm B(\omega) Z_0}{\sqrt{A(\omega)^2 - 1}} = \pm Z_0 \sqrt{\frac{B(\omega)}{C(\omega)}} \tag{5.17}$$

In case of pass band and no loss $B = jb$ and $C = jc$, therefore Z_{BL} is real. By converting transfer matrix parameters to transmission matrix parameters [9], the following relations for propagation constant and Bloch impedance hold:

$$\cosh \gamma d = \frac{Z_{11} + Z_{22}}{2Z_{12}} \tag{5.18}$$

$$Z_{BL}^{\pm} = \frac{Z_{11} - Z_{22}}{2} \pm Z_{12} \sinh \gamma d = \zeta \pm Z \tag{5.19}$$

where:

$$\zeta = \frac{Z_{11} - Z_{22}}{2} \qquad\qquad Z = Z_{12} \sinh \gamma d$$

5.2 DISCRETE PERIODIC STRUCTURES

A more realistic description of infinite periodic structures refers to the case in which they are truncated, having then a discrete number of cells and closed on a load Z_L. At the terminals of the n-th unit cell operating in a pass band one has:

$$V_n = V_0^+ e^{-j\beta nd} + V_0^- e^{+j\beta nd} = V_n^+ + V_n^- \tag{5.20a}$$

$$I_n = I_0^+ e^{-j\beta nd} + I_0^- e^{+j\beta nd} = V_n = \frac{V_n^+}{Z_{BL}^+} + \frac{V_n^-}{Z_{BL}^-} \tag{5.20b}$$

then, at the load terminals, after N cells, one has:

$$V_N = V_N^+ + V_N^- = Z_L I_N = Z_L \left(\frac{V_N^+}{Z_{BL}^+} + \frac{V_N^-}{Z_{BL}^-} \right) \tag{5.21}$$

It is now possible to define the characteristic voltage reflection coefficient at the load as:

$$\begin{aligned} \Gamma_L = \frac{V_N^+}{V_N^-} &= -\frac{\frac{Z_L}{Z_{BL}^+} - 1}{\frac{Z_L}{Z_{BL}^-} - 1} \\ &= \frac{Z - \zeta}{Z + \zeta} \frac{Z_L - Z - \zeta}{Z_L + Z - \zeta} \end{aligned} \tag{5.22}$$

At the nth terminal, the Bloch wave reflection coefficient is:

$$\Gamma_n = \frac{V_n^+}{V_n^-} = \Gamma_L e^{-2(N-n)\gamma d} \tag{5.23}$$

Whereas the input impedance seen at the nth two port is:

$$\begin{aligned} Z_n = \frac{V_n}{I_n} &= \frac{V_n^+ + V_n^-}{I_n^+ + I_n^-} \\ &= \frac{V_n^+(1 + \Gamma_n)}{V_n^+/Z_n^+ + V_n^-/Z_n^-} \\ &= \frac{Z_B + Z_B(1 + \Gamma_n)}{Z_B^- + +Z_B^+ \Gamma_n} \end{aligned} \tag{5.24}$$

Discrete periodic structures used for filtering or as frequency selective circuits could require a matched load, in order to deliver the maximum power delivery. Any matching network can be used as termination [9], recalling that:

- Symmetric discrete structures require a load $Z_L = Z_B^+ = Z_B^-$.
- Asymmetric structures require a load $Z_L = Z_B^+$ at the end of the positive z-direction termination (right side). On the contrary, a load $Z_L = Z_B^-$ is used if matching is required for backward waves, i.e. to negative z.

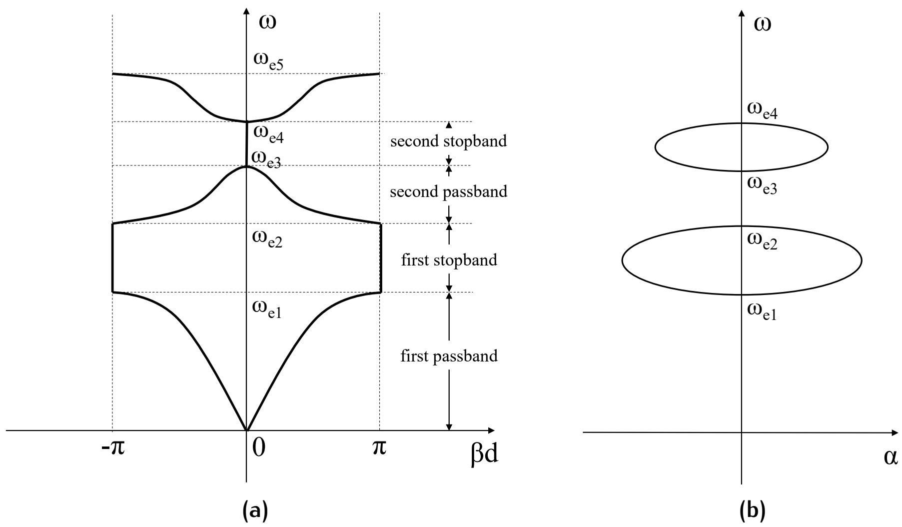

Figure 5.2: Dispersion diagram for a lossless unitcell where stop and pass bands are highlighted. (a) Phase shift (propagation constant). The first three harmonics are plotted and frequencies ω_{ei} limit the boundaries between passbands and stopbands. (b) Attenuation constant.

5.3 DISPERSION DIAGRAM OF A PERIODIC STRUCTURE

A useful visual representation of the dispersive behaviour of the propagation constant γ, for both real and imaginary part, can be obtained by plotting the dispersion diagram (DD), also called Brillouin Diagram. This graph is meaningful for infinite periodic structures only [39]. Frequency is mapped as a function of the phase delay, i.e. the Bloch wave vector imaginary part like:

$$\omega = f(\beta(\omega)) \tag{5.25}$$

of which, on example is plotted in figure 5.2. Equation 5.25 is often difficult to express explicitly and the solution of the eigenmode system 5.5 could not be unique, meaning that different frequencies may share the same wave number β, producing the characteristic *band* structure of the diagram [40]. The number of bands is, as rule of thumbs, equal to the number of resonating element contained in the unit cell [39]. The reason why βd is called phase delay, comes from equation 5.5: supposing to be in passband and in a lossless system, i.e. $\alpha = 0$, βd is the argument (phase) of the harmonic eigenfunction $e^{-j\beta d}$, that represents that delays the Bloch wave from input to output terminal though the unit cell.

Equation 5.11 is the function that describes the behaviour of the propagation constant in pass band. It is a bounded function whose limits are [0,+1] for the forward mode and [-1,0] for the backward mode, in fact:

$$-1 < \cos \beta d = tr(\underline{\mathbf{T}}(\omega))/2 < 1 \tag{5.26}$$

Equation above is real and defined provided that the right-hand side has value in the interval [-1,1] only. The set of βd values for which the relation above is true is $-\pi < \beta d < \pi$. This interval is also known as *first Brillouin zone* (FBZ) or irreducible BZ. Figure 5.2 shows that the limit of pass and stopbands occur at multiple values of π and that this is the periodicity of the FBZ. In particular, one edge of the passband always occur when the electrical spacing between discontinuities (two-port terminals) is equal to one half of the guided mode wavelength, or, more in general, where symmetry in the system are defined [41]. Since the structure is continuous and 5.11 periodic, solution with $\beta d = \beta d + 2n\pi$, with n arbitrary integer, are still valid and they are associated to Bloch wave spatial harmonics, in which the guided mode can be expanded.

5.4 PHASE AND GROUP VELOCITY

Recalling that the free space the following relation hold:

$$k_0 = \omega\sqrt{\epsilon_0\mu_0} = \omega c \tag{5.27}$$

it is possible to define the *phase velocity* for a periodic structure as:

$$v_p = \frac{\omega}{\beta} = \frac{k_0 d}{\beta d} c \tag{5.28}$$

that, as depicted in figure 5.3 it represent the slope of a line from the origin to a point P in the dispersion diagram. It represent the speed at which a single harmonic (tone) moves in the periodic structure.

Recalling that γ is a function of frequency, one has that the *group velocity* is different from the phase velocity. The definition follows:

$$v_g = \frac{d\omega}{d\beta} = c\frac{d(k_0 d)}{d(\beta d)} \tag{5.29}$$

Group velocity is equal to the slope of the function $\omega(\gamma)$ and as it appear from figure 5.3 it is null at FBZ and it tends to zero close to its edges. Every time v_g or v_p deviate from equation 5.27, called *light line*, the system is defined *dispersive*. Moreover, v_g is the speed at which a signal can propagate through a waveguiding structure, with a *group delay*:

$$\tau = \frac{d}{v_g} \tag{5.30}$$

It can be shown that the same rules are valid in periodic transmission line, and that v_g is the speed at which energy flows throughout the line [38]. The demonstration is reported in Appendix B. Moreover, it is necessary to point out that phase and group velocity are meaningful quantities as long as the medium is purely dispersive, then $\omega = \omega(\beta)$. If absorption also occurs, the two quantities cease to have a physical meaning. On the contrary, energy velocity meaning remains valid [39].

5.5 FLOQUET'S THEOREM AND SPATIAL HARMONICS

Floquet's theorem introduces the possibility of expressing the field as superposition of field harmonics in a periodic structure. Having the total electric

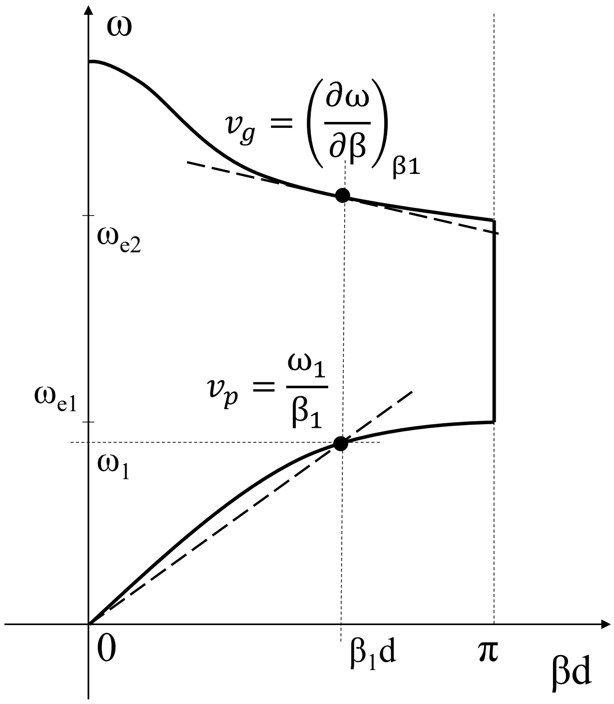

Figure 5.3: Visual difference between phase velocity v_p and group velocity v_g.

(magnetic) field defined in the periodic structure, with periodicity d, as follows:

$$\mathbf{E}(x,y,z) = \mathbf{E}(x,y,z)e^{-\gamma z} \tag{5.31}$$

with $\mathbf{E}_p$ periodic vector function along z such that:

$$\mathbf{E}_p(x,y,z+nd) = \mathbf{E}_p \tag{5.32}$$

Then, the periodic field vector $\mathbf{E}_p(x,y,z)$ is expressed through Floquet's theorem as:

$$\begin{aligned} \mathbf{E}_p(x,y,z) &= \sum_{n=-\infty}^{\infty} \mathbf{E}_{pn}(x,y)e^{-j\beta z - j\frac{2n\pi z}{d}} \\ &= \sum_{n=-\infty}^{\infty} \mathbf{E}_{pn}(x,y)e^{-j\beta_n z} \end{aligned} \tag{5.33}$$

The amplitudes $\mathbf{E}_{pn}$ are periodic vector function along z with periodicity d associated to the n-th mode. Each element of the expansion is an Hartree or *spatial harmonic* propagating with β_n and phase velocity:

$$v_{pn} = \frac{\omega}{\beta_n} = \frac{\omega}{\beta + 2n\pi/d} \tag{5.34}$$

Notice that this quantity can be negative, depending on which n is selected. The group velocity of each Hartree harmonic will be:

$$v_{gn} = \left(\frac{d\beta_n}{d\omega}\right)^{-1} = \left(\frac{d\beta}{d\omega}\right)^{-1} = v_g \tag{5.35}$$

from where it is easy to notice that each harmonic propagates with the same dispersive law, even if v_p and v_g could have opposite signs. A visual representation of the Floquet expansion is given in figure 5.4.

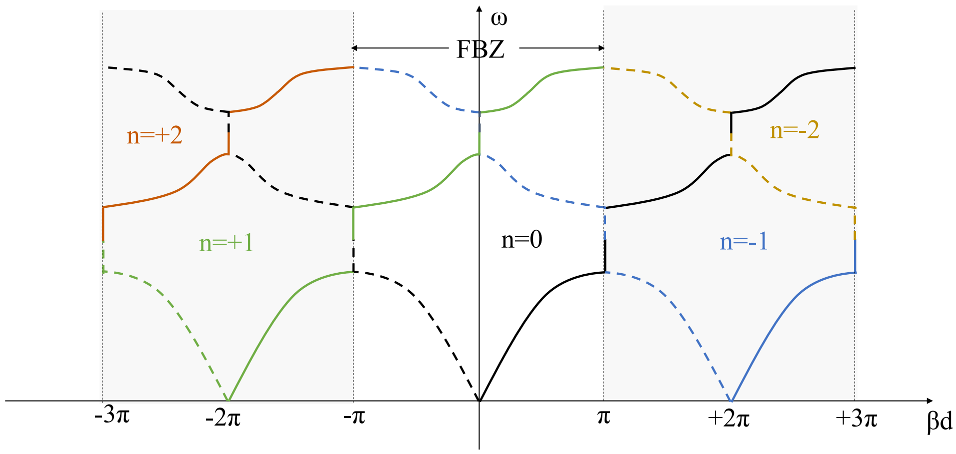

Figure 5.4: Dispersion diagram expanded in for n spatial harmonics. Solid lines are for forward propagating modes, dashed lines for backward propagation.

5.6 N-TH ORDER EPDS

Now that some of the mathematical and physical aspects of periodic structures have been highlighted, it is possible to focus on specific properties that such a system can have and what are the necessary conditions to make them appear. In particular, it is interesting to consider how to model and describe a periodic circuit working at the edges of its pass and stopbands. It is also useful to consider a more complete version of the dispersion diagram that represents the FBZ only like the one in figure 5.2. As it appears both real part βd (phase shift) and attenuation αd are reported on the same graph.[1] In a lossless structure, attenuation is null in passbands whereas $\Re\gamma$ is non zero. On the contrary the phase shift becomes null (and meaningless) in stopbands, where αd is positive for forward Floquet modes and negative for backward waves. It is also noticeable how the dispersion diagram of a periodic structure exhibits a mirror symmetry around the band edges (namely: $\beta d = 0, \pi$); the origin of this fact comes from the Floquet theory, as presented in the previous section. The dispersion diagram shows that there are two independent periodic eigenstates, associated to four distinct periodic eigenvalues. However, a periodic structure, described by a two-port presents this behaviour in all the dispersion diagram except to the points located at the edges of each passband-stopband transition. These specific frequencies are denoted as *band edges*. In fact, provided that the system is gainless and lossless, at this points both eigenvalues and eigenvectors coalesce originating a degeneracy condition known as *exceptional point of degeneracy*, or EPD.[2]–[4], [8], [10], [13] Notice that having an EPD is different than having just a degenerate eigenmode condition in a system. For example, two different uniform transmission line can share the same eigenvalues, having though different field distributions [10].

The simplest degeneracy condition can happen in two-ports described by a 2x2 transmission matrix $\underline{\mathbf{T}}$, in which two Floquet modes with having eigen-

1 Notice that, conversely to the phase shift, attenuation exponential term is not a periodic function, meaning that the graph only serves as qualitative reference to the following analysis

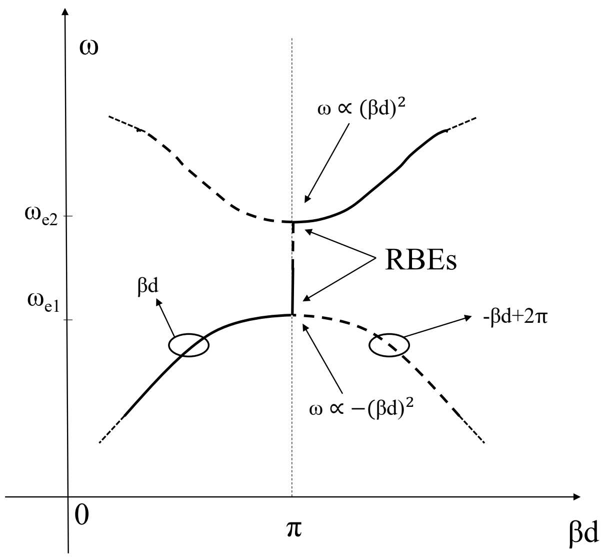

Figure 5.5: Coalescence of two Floquet harmonics at FBZ edge ($\beta d = \pi$) in a lossless structure.

values $+\beta$ and $-\beta + 2\pi/d$ coalesce (as in figure 5.5). Manifesting at the border or at the centre of the FBZ, this condition represent a second order degeneracy an it is referred as *regular band edge* (RBE) [8]. Higher order degeneracy conditions can happen in circuit that can support more modes [6], [7], [10]. Also in this case the idea at the basis of EPDs remains the same: system eigenvectors coalesce forming a unique eigenvector for a specific frequency (that in this case can be far from FBZ edges), at which also eigenvalues degenerate. Even though EPDs with order higher than four have not been observed yet [7], a general formulation to model the mathematics behind this problem exists, and it is proposed below.

Considering a generic N-port, whose state vector at port i is denoted by:

$$\mathbf{\Phi}_i(z) = [\phi_1(z), \phi_2(z), \ldots, \phi_n(z)]^T \tag{5.36}$$

its $N \times N$ transmission matrix $\underline{\mathbf{T}}$ will be such that the following eigenvalue problem can be written:

$$(\underline{\mathbf{T}} - \xi_i \underline{\mathbb{I}})\mathbf{\Phi}_i = 0 \tag{5.37}$$

The diagonalizability of matrix $\underline{\mathbf{T}}$ as been assumed. State vectors $\Phi_i(z)$ are also called regular eigenvectors, corresponding to Floquet-Bloch multipliers $\xi_i = e^{+jk_i d}$, with $i = 1, 2, 3, ..., N$, where both k and $-k$ wave vector are solutions, defined in the FBZ in $[-\pi, \pi]$. It is then possible to define the diagonal matrix $\underline{\mathbf{\Gamma}}$ as:

$$\underline{\mathbf{\Gamma}} = \begin{bmatrix} \xi_1 & 0 & \ldots & 0 \\ 0 & \xi_2 & \ldots & \vdots \\ \vdots & \vdots & \ddots & 0 \\ 0 & \ldots & 0 & \xi_N \end{bmatrix} \tag{5.38}$$

such that:

$$\underline{\mathbf{T}} = \underline{\mathbf{V}\mathbf{\Gamma}\mathbf{V}}^{-1} \tag{5.39}$$

where $\underline{\mathbf{V}}$ is a $N \times N$ non singular similarity transformation matrix that diagonalizes $\underline{\mathbf{T}}$. Outside band edge, each column of $\underline{\mathbf{V}}$ contains one of the N independent eigenvectors that are solution for the system, i.e. $\underline{\mathbf{V}} = [\mathbf{\Phi}_1^*|\mathbf{\Phi}_2^*|\ldots|\mathbf{\Phi}_N^*]$ (the symbol * denotes the normalized eigenvector of the system).

Though, this condition is no more valid at an EPD: eigenvalues algebraic and geometric multiplicity become equal, eigenvectors degenerate, $\underline{\mathbf{T}}$ becomes defective and non diagonalizable and $\underline{\mathbf{V}}$ become singular. From linear algebra it is well known that Jordan Blocks exhibit one degenerate eigenvector only, and N-1 other generalized eigenvectors [23]. ({valid for each value of N?}) The solution for the N generalized eigenvectors can be found by solving the Floquet-Bloch form [7]:

$$[\underline{\mathbf{T}} - \xi_d \underline{\mathbb{I}}]^q \mathbf{\Phi}_q^g(z) = 0, \qquad \text{q = 1,2,3,...,N} \tag{5.40}$$

where $\mathbf{\Phi_1}^g = \mathbf{\Phi_1}$ is the regular eigenvector, whereas $\mathbf{\Phi}_2^g$, $\mathbf{\Phi}_3^g,\ldots,\mathbf{\Phi}_N^g$ are the generalized eigenvectors of ranks 2,3,. . . ,N, respectively. It can be proven that in such a condition the transmission matrix $\underline{\mathbf{T}}$ is similar to a Jordan canonical matrix, for which the following transformation is valid:

$$\underline{\mathbf{T}} = \underline{\mathbf{S}}\underline{\mathbf{\Gamma}}_d\underline{\mathbf{S}}^{-1}, \quad \underline{\mathbf{\Gamma}}_d = \begin{bmatrix} \xi_{d,1} & 1 & 0 & 0 \\ 0 & \xi_{d,2} & 1 & 0 \\ 0 & 0 & \xi_{d,3} & 1 \\ 0 & 0 & 0 & \xi_{d,4} \end{bmatrix} \tag{5.41}$$

where $\underline{\mathbf{V}} = [\mathbf{\Phi}_1^g|\mathbf{\Phi}_2^g|\ldots|\mathbf{\Phi}_N^g]$. Even in this case degeneracy can occur both at centre or at the edge of the FBZ.

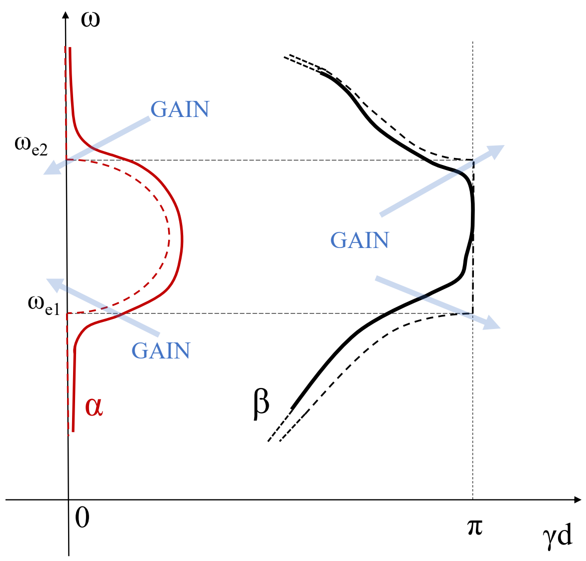

Figure 5.6: Detail on half FBZ edge ($\beta d = \pi$) for a periodic lossy structure with and without loss and gain balance.

5.7 EPDS IN PRACTICE

It is important now to recall that a perfect degeneracy condition corresponds to an infinite lossless structure and it does not exists in practice (figure 5.6).

Whenever a discrete periodic structure is taken into account or losses are present (substrate, conduction or radiation) external gain may be added in order to retrieve, only at some frequencies, the main features typical of having EPDs.

Moreover, EPDs are very sensitive to any kind of tolerances in components parameters [7]. In particular, willing to design an antenna whose working principle is based on EPDs, losses become a necessary presence, in a distributed form. Regardless the kind of perturbation that is affecting the circuit, a certain degree of degeneracy can be still retrieved and evaluated through a mathematical tool proposed in [7], where the concept of *hyperdistance between four eigenvectors of the transfer matrix* is developed. This quantity, denoted by D_H can be generalized to an N-th order degeneracy as follows:

$$D_H(\omega) = \frac{1}{k} \sum_{m=1,n=1,m\neq n}^{N} |\sin\theta_{mn}| \tag{5.42}$$

$$\theta_{mn}(\omega) = \text{acos}\left(\frac{\text{Re}\{\langle \mathbf{\Phi}_m | \mathbf{\Phi}_n \rangle\}}{||\mathbf{\Phi}_m||||\mathbf{\Phi}_n||}\right) \tag{5.43}$$

where $k = N(N-1)(N-2)...(N-j+1)$. Where $\langle \mathbf{\Phi}_m | \mathbf{\Phi}_n \rangle$ represents the generalized scalar vector between complex vectors. The hyperdistance vanishes whenever the complex angle between all the eigenvectors becomes null. This quantity is better suited for evaluating the degree of degeneracy than $\det(\underline{\mathbf{U}})$. In fact, to make the latter quantity approaching zero it is enough that two only eigenvectors coalesce at a certain frequency ω (this could be useful to recognise a RBE, not higher order EPDs though). Conversely the former quantity, keeps into account the angle between all the system eigenvectors. Though, in case of a two-port with N=2, $\det(\underline{\mathbf{U}})$ is sufficient to recognise coalescence, since two eigenvectors only are present. $D_H(\omega_e)$ is null in lossless and periodic structures, though it can only approach zero in practical cases. Therefore, a threshold ϵ_e, whose value depends on the application, such that an EPD is present whether $D_H(\omega_e) < \epsilon_e$.

As mentioned, the particular condition that allows the existence of an EPD requires the addition of *gain*. Basically, this gain is provided by means of active elements, that can compensate part of the losses naturally present in the circuit. The goal to be achieved is the perfect *loss and gain balance*, that ideally would bring back the hyperdistance at zero at EPD frequency. Notice that gain compensation condition does not imply parity-time symmetry in the circuit [7], therefore gain and loss could not be exactly symmetric in magnitude.

Moreover, loss and gain balance does not imply that the circuit is unstable, providing self-oscillation in a finite-length structure. One remark, is that perfect compensation could not even be necessary to achieve the benefits provided by an EPD [7].

5.8 REGULAR BAND EDGE, RBE

A regular band edge is a point of degeneracy in which two states present the same eigenvectors and eigenvalues. Taking the graph in figure 5.5 as reference, the EPD frequency is indicated as ω_e (associated to a wave vector β_e). It is possible to identify the transition from two states with phase progression at $\omega < \omega_e$ into two purely evanescent states for $\omega > \omega_e$. The transition frequency is represented by $\omega = \omega_e$, in which the corresponding eigenstate represents a standing resonant mode with infinite group delay [10]. It has been demonstrated that a system working at EPD regime can offer much sharper resonance, then higher Q-factor, compared to other system in which degeneracy is not exploited. Working close to an EPD imply low group velocity, increasing the round-trip travel time inside a resonator meaning large quality factors [38]. Moreover, the higher the degree of degeneracy is, the more properties related to frequency response of the circuit are enhanced [4], [6], [7]. Although dispersion relation and dispersion diagram is exact for infinite structures only, the benefits of EPDs are still noticeable with a discrete number of unit cells. It has been demonstrated in [2] that resonances take place in the vicinity of the band edge. Furthermore, fields behave very similarly to standing wave at each of these frequencies. Under this assumption the wave vector for both forward and backward Floquet-Bloch modes, at resonance can approximated as:

$$\beta_s \approx \beta_e \pm \frac{\pi}{Nd} s, \quad \text{s=1,2,...} \tag{5.44}$$

where s is he order of the number of resonant peaks before or after ω_e, β_e is the wave number at FBZ edge, hence $k_e = \pi/d$ and N is the number of cells employed in the discrete periodic structure. Below (or above) band edge, the dispersion relation $\omega(\beta)$ can be approximated by a quadratic parabola as:

$$\omega \approx \omega_e + \frac{1}{2}\left(\frac{\partial^2 \omega}{\partial \beta^2}\right)_{\beta=\beta_e} (\beta - \beta_e)^2 \tag{5.45}$$

Where the second order derivative is negative if the passband is defined for $\omega < \omega_e$ and positive if the passband is defined for $\omega > \omega_e$. Substituting 5.44 in 5.45 one has:

$$\omega_s(N) \approx \omega_e + \frac{1}{2}\left(\frac{\partial^2 \omega}{\partial \beta^2}\right)_{\beta=\beta_e} \left(\frac{\pi}{Nd} s\right)^2, \quad \text{s=1,2,...} \tag{5.46}$$

Equation 5.46 suggests that for a structure with a sufficiently high number of unit cells, resonance frequency ω_s would be close to ω_e. Notice that this quadratic approximation is valid for second order degeneracy. Higher orders, would bring to even more sharper response, thanks to the wider range of β for which the group velocity would be closer to zero (larger group delay).

As already stated, in RBE condition both eigenvectors and eigenvalues must be degenerate. The former condition is guaranteed by:

$$|\det(\underline{\mathbf{U}}(\omega_e))| < \epsilon_e \tag{5.47}$$

whereas the latter is obtained from the general case of equation 5.10, with $\det(\underline{\mathbf{T}}) \neq 1$:

$$\lambda_{1,2} = \frac{tr(\underline{\mathbf{T}})}{2} \pm \sqrt{\left(\frac{tr(\underline{\mathbf{T}})}{2}\right)^2 - \det(\underline{\mathbf{T}})} \tag{5.48}$$

from where one has that $\lambda_1 = \lambda_2$ if and only if $tr\underline{\mathbf{T}}/2 = \pm\sqrt{\det(\underline{\mathbf{T}})}$.

6 ANTENNA THEORY AND LEAKY WAVE ANTENNAS

6.1 ANTENNA PARAMETERS

This chapter aims to define the basic formalism useful to understand the most important antennas parameters used to qualify the performance of these structures in farfield. Farfield is define as a region in which longitudinal component of the radiated field can be neglected and fields can be approximated by their θ and φ components only in the form:

$$\mathbf{E}(r,\theta,\varphi) \simeq B_0 \boldsymbol{p}_e(\theta,\varphi)) \frac{e^{-jkr}}{4\pi r} \tag{6.1}$$

where: B_0 is a quantity that includes information on field intensity and antenna geometry, $\boldsymbol{p}(\theta,\varphi))$ is the generalized electric moment given by the field distribution on the source, and $\frac{e^{-jkr}}{4\pi r}$ is the Greens spheric function. The derivation of 6.1 can be found in appendix C. Commonly farfield region is taken as a distance $R_{ff} > 2D_A^2/\lambda$ to infinity from the antenna, in which D_A is the larger dimension and λ the radiated frequency.

6.1.1 Radiation Power and Intensity

Electromagnetic waves are used to carry informations trough wireless or guiding media, from one point to the other. The radiated power per unit area can be evaluated by means of the Poynting vector, that is defined as follows for both time domain (instantaneous) on the left and its complex counterpart, on the right (phasor):

$$\mathscr{S}(x,y,z;t) = \mathscr{E} \times \mathscr{H} \qquad \mathbf{S}(x,y,z) = \frac{1}{2}\mathrm{Re}(\mathbf{E} \times \mathbf{H}^*) \tag{6.2}$$

Both relations are defined in [W/m^2]. Weather the left hand side defines an instantaneous value, the right hand side represent the averaged power density per unit area. To obtain the total radiated power it is sufficient to integrate over a spherical surface S as follows:

$$P_r = \oint_S \mathbf{S} \cdot d\boldsymbol{s} = \frac{1}{2}\oint_S \mathrm{Re}(\mathbf{E} \times \mathbf{H}^*) \cdot d\boldsymbol{s} \quad [\mathrm{W}] \tag{6.3}$$

One can now define the *radiation intensity* as the power radiated from and antenna per unit solid angle as:

$$U = r^2|\mathbf{S}| = r^2 W_r \qquad [\mathrm{W/unit\ solid\ angle}] \tag{6.4}$$

where W_r is the radiation density ([W/m^2]) and r the radius of the sphere. Recalling that $W_r = |\mathbf{E}(r, \theta, \varphi)|^2/(2Z_0)$ (where Z_0 is the characteristic impedance of the medium), one has:

$$\begin{aligned} U(\theta,\varphi) = \frac{r^2}{2Z_0}|\mathbf{E}(r,\theta,\varphi)|^2 &\simeq \frac{r^2}{2Z_0}[|\mathbf{E}_\theta(r,\theta,\varphi)|^2 + |\mathbf{E}_\varphi(r,\theta,\varphi)|^2] \\ &\simeq [|\mathbf{E}^0_\theta(\theta,\varphi)|^2 + |\mathbf{E}^0_\varphi(\theta,\varphi)|^2] \\ &= B_0 F(\theta,\varphi) \end{aligned} \tag{6.5}$$

where $\mathbf{E}(r, \theta, \varphi) = \mathbf{E}^0(\theta, \varphi)\frac{e^{-jkr}}{r}$ is the farfield electric field radiated from the antenna. The approximations made in the equation before come from the farfield fields derivation as reported in appendix C. Total radiated power can be evaluated by integrating over the solid angle:

$$P_r = \oint_\Omega U d\Omega = \int_0^{2\pi}\int_0^{\pi} U \sin\theta d\theta\, d\varphi \tag{6.6}$$

6.1.2 Beamwidth, Directivity, Efficiency and Gain

There exist two main parameters defined by IEEE to evaluate the beamwidth of an antenna. The *half power beam width*, HPBW, is defined as "In a plane containing the direction of the maximum of a beam, the angle between the two directions in which the radiation intensity is one-half value of the beam" [42]. The second important quantity is referred as *first null beam width*, FNBW, that is the angle at which the first null of the main lobe is located.

Directivity is meaningful for non-isotropic sources and it is defined as:

$$D = \frac{U}{U_0} = \frac{4\pi U_{max}}{P_r} \tag{6.7}$$

The quantity is dimensionless and it is calculated as the ratio between the maximum of the radiation intensity in a given direction and the total power radiated by the antenna as it was radiated by an isotropic point source. This quantity is always greater than one in the direction of maximum radiation and it is referred as $\max_{4\pi}(D) = D_0$. Actually, this is a figure of merit that gives indications about the directional properties of an antenna compared with those of an isotropic source radiating the same power [43]. To consider sources whose farfield depend on spherical coordinates, one can define:

$$U_{max} = B_0 F(\theta,\varphi)|_{max} \tag{6.8}$$

therefore:

$$\begin{aligned} D_0 &= \frac{4\pi F(\theta,\varphi)|_{max}}{\int_0^{2\pi}\int_0^{\pi} F(\theta,\varphi)\sin\theta d\theta\, d\varphi} \\ &= \frac{4\pi}{\int_0^{2\pi}\int_0^{\pi} F_n(\theta,\varphi)\sin\theta d\theta\, d\varphi} \end{aligned} \tag{6.9}$$

where

$$F_n(\theta,\varphi) = \frac{F(\theta,\varphi)}{F(\theta,\varphi)|_{max}} \tag{6.10}$$

is the *normalized radiation pattern*.

Simpler expressions are available to estimate directivity for antennas in which sidelobes level is well below main lobe. Given that, the main lobe HPBW is taken for the two main cuts (e.g. E-plane or H-plane[1]) One has:

$$D_0 \approx \frac{72.815}{HPBW_E^2 + HPBW_H^2} \tag{6.11}$$

where HPBW_E and HPBW_H are defined for E and H-plane, respectively (degrees).

Antenna efficiency is used to consider losses and the input terminal and within the antenna itself:

$$\eta_0 = \eta_{cd}(1 - |\Gamma|^2) \tag{6.12}$$

where $(1 - |\Gamma|^2)$ is the reflection missmatch efficiency, defined at the antenna input terminals, whereas η_{cd} is the radiation efficiency, that includes information about the antenna loss due to conduction and dielectric. In fact an antenna can be seen as a lossy one-port whose input impedance is $Z_A = R_r + R_L + jX_A$, in which R_r is the radiation resistance of the antenna, i.e. the loss component converted in radiation. The remaining part of the impedance is needed to take into account conduction losses and reactive behaviour. Maximum power delivery, with $\Gamma = 0$ is obtained in case of conjugate matching. In this case given a generator whose output impedance is $Z_g = R_g + jX_g$, then $R_g = R_r + R_L$ and $X_g = -X_A$.

Radiation efficiency η_r is the link between directivity and antenna *gain*. Gain, is defined as:

$$G = \frac{4\pi U(\theta, \varphi)}{P_{in}(\text{lossless isotropic source})} \tag{6.13}$$

and it is the ratio between the radiation intensity of the antenna and the input power accepted by an isotropic source. It can be also defined with respect to power accepted by other kind of reference antennas (such as horn antennas). Noticing that $P_r = \eta_{cd}/$:

$$G(\theta, \varphi) = \frac{4\pi U(\theta, \varphi)}{P_r/\eta_{cd}} = \eta_{cd} D(\theta, \varphi) \tag{6.14}$$

In the direction of maximum radiation:

$$G_0 = \eta_{cd} D_0 \tag{6.15}$$

$$G_{0abs} = \eta_0 D_0 \tag{6.16}$$

In case of input matching at antenna terminals, one has $\Gamma = 0$, hence $G_0 = G_{0abs}$ In case of directive antennas an empirical estimation for G_0 is:

$$G_0 \simeq \frac{30000}{HPBW_E HPBW_H} \tag{6.17}$$

1 Actually, these two reference planes are defined for linearly polarized sources only, but they can be used for other kind of polarizations [42].

6.1.3 Polarization

Polarization of a radiated wave is defined as a curve traced by the end point of the vector representing the instantaneous electric field, once it is observed along the direction of propagation [43]. This quantity may vary depending on which pattern direction is chosen. In particular, for distance large enough from a transmitting antenna, an observer would receive the polarization of a plane wave. In fact, increasing the radial direction of propagation, the ray of curvature of a radiated wave approaches infinite, therefore appearing as a plane wave front.

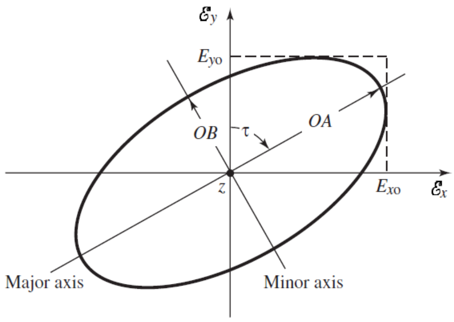

Figure 6.1: Polarization plane for an electromagnetic wave and its polarization ellipse as a function of time [42].

Field variables in time-harmonic regimes at any point appear like:

$$\begin{aligned}\mathscr{E}(x,y,z,t) &= \mathrm{Re}\{(\mathscr{E}_{x0}e^{jk_x x}\hat{\boldsymbol{x}} + \mathscr{E}_{y0}e^{jk_y y}\hat{\boldsymbol{y}} + \mathscr{E}_{z0}e^{jk_z z}\hat{\boldsymbol{z}})e^{j\omega_0 t}\} \\ &= \mathrm{Re}\{(\mathbf{E}' + j\mathbf{E}'')e^{j\omega_0 t}\} = \mathrm{Re}\{\mathbf{E}e^{j\omega_0 t}\} \\ &= \mathbf{E}'\cos\omega_0 t - \mathbf{E}''\sin\omega_0 t \qquad (6.18)\end{aligned}$$

Therefore, the electric field can be defined as the sum of two vectors with arbitrary directions on the *polarization plane*. This representation is useful to have information about the vector polarization of a given time-harmonic field. Depending on the phasors $\mathbf{E}'$ and $\mathbf{E}''$ one can have three different conditions:

- *Linear* polarization if $\mathbf{E}' \times \mathbf{E}'' = 0$.
- *Circular* polarization if $\mathbf{E}' = \mathbf{E}''$ and $\mathbf{E}' \cdot \mathbf{E}'' = 0$.
- *Elliptical* polarization if $\mathbf{E}' \neq \mathbf{E}''$ and the two vectors are neither parallel or perpendicular.

An example of polarization plane for an elliptical polarization is shown in figure 6.1. The plot domain is the (θ,φ) plane and the two main axis are visible in the polarization ellipse: OA, the major axis and OB, the minor axis. The ratio of the length of these two quantities gives the *axial ratio* [43]:

$$AR = \frac{OA}{OB}, \qquad 1 \leq AR \leq \infty \qquad (6.19)$$

where:

$$OA = \sqrt{\frac{1}{2}\left[E_\theta^2 + E_\varphi^2 + \sqrt{E_\theta^4 + E_\varphi^4 + 2E_\theta^2 E_\varphi^2 \cos(2\Delta\varphi)}\right]} \tag{6.20}$$

$$OB = \sqrt{\frac{1}{2}\left[E_\theta^2 + E_\varphi^2 - \sqrt{E_\theta^4 + E_\varphi^4 + 2E_\theta^2 E_\varphi^2 \cos(2\Delta\varphi)}\right]} \tag{6.21}$$

This quantity is calculated in CAD like CST MW Studio, and can be used to understand the polarization. In fact, the field is:

- Circularly polarized if $AR = \infty$ ($\Delta\varphi = \pm\pi/2$).
- Linearly polarized if $AR = 1$ ($\Delta\varphi = 0, \pi$).
- Elliptically polarized otherwise.

6.2 LEAKY WAVE ANTENNAS

Leaky wave antennas (LWA) are a class of antenna based on travelling wave and use them to obtain radiation. The main advantages of this kind of radiators are the possibility of frequency controlled beam steering and beamwidth sharpness along with feeding and structural simplicity (waveguide or printed technology). Leaky wave antennas can support fast or slow waves where the phase constant is less than the free-space wavenumber k_0. This property allow the travelling wave to leak power in a continuous way along the guiding structure. From there the name *leaky*. The propagation constant can only be complex for this kind of waves since loss is required to have radiation. The wavenumber along the propagation direction is defined by $k_z = \beta - j\alpha$.[2] Depending on weather the structure is *uniform*, *quasi-uniform* or *periodic* different kind of physical mechanism take place leading the antenna to radiation. Another way to classify LWAs comes by considering weather they are one or two-dimensional. This chapter is focused on one dimensional leaky wave antennas, since the main goal of the thesis is the development of such a structure. Though the same principles can be applied to two-dimensional structures that represent a possible development of the proposed design [44].

One-dimensional Uniform LWAs

The structure can be fed at one edge or in the middle. In both cases an absorbing termination is required for residual propagating power. What visually characterize this antennas is a longitudinal uniform geometry along the propagation direction, z (the structure can be uniform or even tapered for beam shaping purposes). This kind of structure supports wave radiation in one quadrant only, with a continuous power leakage along the extension of the aperture. Radiation is forward directed if $\beta > 0$ or backward directed if $\beta < 0$. In case of centre feeding, the radiation is mirrored with respect the symmetry axis (x). Broadside radiation is possible with composite right/left-handed structures only [44].

2 Here the convention is opposite to what is used in chapter 5, where the wavenumber is indicated by $\gamma = \alpha + j\beta$.

One-dimensional Periodic LWAs

The antenna can be fed at its centre or at the edges and power matching loads are required. One-dimensional periodic LWAs present uniform structures where a slow propagating wave with $\beta > k_0$ is periodically modulated along the longitudinal direction. Radiation takes place along the structure where the slow wave encounters discontinuities introduced by the periodic modulation. In chapter 5 the theory behind Floquet waves has been presented and it now clear how a periodic modulation allows one to expand the propagating field in a superposition of infinite harmonics whose wavenumber is represented by $k_{zn} = k_0 + 2\pi n/d$, where d is periodicity, and $k_0 = \beta - j\alpha$ the wave vector of the fundamental Floquet mode ($n = 0$). The fundamental mode must be a slow wave incapable of radiation, but one of the higher order harmonics is usually designed to be fast and produce radiation. Usually the $n = -1$ harmonic is used for this purpose, for which $-k_0 < \beta_{-1} < k_0$. The wavenumber sign decide the direction of propagation and usually this LWA can support both forward and backward modes. Beam steering is controlled by tuning the operation frequency spanning from the negative ($z < 0$) to the positive ($z > 0$) quadrant. Radiation at the edges of the radiation (endfire) is usually conically shaped, whereas the broadside farfield approaches a donut shaped. Unfortunately, radiation is usually degradated at broadside since this direction corresponds to the edge of the periodic structure stop-band in frequency domain. Previously, stop band condition has been analysed, pointing out that it correspond to a zero-group velocity point, hence to a standing wave into the structure. The same happens here, where the LWA turns into a standing wave antenna, where, having attenuation constant close to zero, radiation is degradated. An additional drawback is that the same radiator used as LWA presents a different radiation pattern if used as standing wave antenna. Moreover, matching is usually difficult in the second design [43], requiring also the presence of reactive loads to obtain the correct field phase in each radiating element.

One-dimensional Quasi-Uniform LWAs

Feeding is can be provided at both one edge or at the end of the line and absorbers are also required. The main difference between periodic and quasi-uniform LWAs is that the former has uniform geometry, whereas the latter shows a periodic shaping along the waveguiding structure. Besides, the fundamental Floquet tone is a fast wave and radiation occurs because of this one.

6.3 FIELD BEHAVIOUR OF LEAKY WAVES

In order to achieve radiation, a leaky wave antenna must support a fast wave with $\beta < k_0$. Given an infinitely extended aperture with a TM electric field $E_y(x, z)$, at the metal-air interface ($x = 0$) one has:

$$E_y(0, z) = Ae^{-jk_z z} \tag{6.22}$$

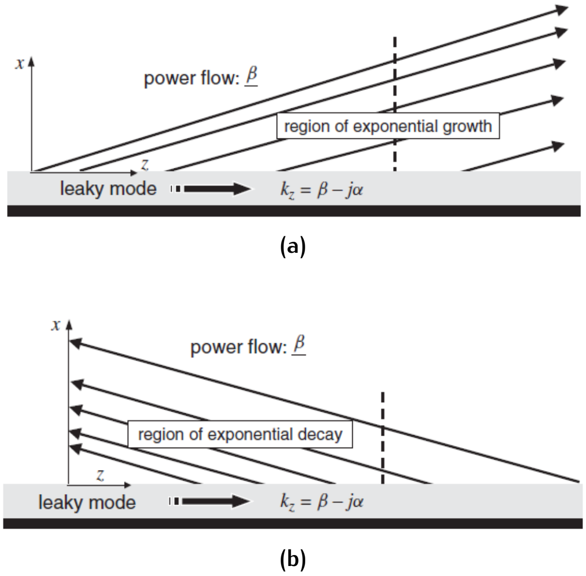

Figure 6.2: Ray picture used as a physical interpretation of field behaviour and radiated power in leaky-wave antennas: (a) forward leaky wave and (b) backward leaky way [43].

where the wave vector the wave vector is $k_z = \beta - j\alpha$ and A a constant. The power leakage of such an LWA is associated to the attenuation constant α. Above the aperture, for $x > 0$ one has:

$$E_y(0,z) = Ae^{-jk_z z}e^{jk_x x} \tag{6.23}$$

where the x component of the wavenumber is:

$$k_x = \sqrt{k_0^2 - k_z^2} \tag{6.24}$$

where $k_0 = \omega\sqrt{\epsilon_0\mu_0}$ is the free space wave number. Defining $k_x = \beta_x - j\alpha_x$, squaring and equating imaginary parts in 6.24:

$$\beta\alpha = -\beta_x\alpha_x \tag{6.25}$$

Supposing forward propagation along z, one has $\beta > 0$ and $\alpha > 0$, therefore it follows that $\alpha_x < 0$, meaning that the wave in the air region is exponentially increasing (figure 6.2). As it appear, a decaying propagation along z, must be accompanied by an exponential increase in the surrounding medium. This behaviour is often referred as *improper* or *non-spectral* [43]. The reason why the imaginary part of the wave vector vertical component is negative, can be easily explained. Being the LWA radiating, the power flow is directed outside the boundary of the guiding medium, along a direction pointed by the phase vector:

$$\boldsymbol{\beta} = \hat{\boldsymbol{x}}\beta_x + \hat{\boldsymbol{z}}\beta_z = \mathrm{Re}(\bar{k}) = \mathrm{Re}(\hat{\boldsymbol{x}}k_x + \hat{\boldsymbol{z}}k_z) \tag{6.26}$$

in which $\beta = \beta_z$. One can define:

$$\tan\theta_0 = \frac{\beta_x}{\beta_z} \tag{6.27}$$

the angle between the phase vector $\bar{\beta}$ and the guiding medium (yz plane). Provided that the attenuation factor is small, one has:

$$\cos\theta_0 = \frac{\beta}{k_0} \quad [\text{rad}] \tag{6.28}$$

that is a useful relation to understand the radiation inclination for the LWA. Moreover, half power beam width (HPBW) can be evaluated by means of an empirical formula proposed by Oliner in [45]:

$$HPBW \approx \frac{1}{\frac{Lk_0}{2\pi}\cos\left(\frac{\pi}{2}-\theta_0\right)} \quad [\text{rad}] \tag{6.29}$$

where L is the length of the LWA. Equation 6.28 predicts weather radiation takes place or not. In particular, whenever $|\beta| < k_0$ it exists a real value θ_0 at which the LWA radiates. On the contrary, if $|\beta| > k_0$ the propagating mode is a slow wave whose leakage angle is complex, meaning that no leakage angle exist in the visible space. The corresponding mode is a surface wave whose amplitude is exponentially decaying and diffused in near field only above the aperture. Slow waves are still able to radiate at discontinuities (for example from the source), but they are referred as *non-physical* and are non likely to be physically significant (no radiation except for discontinuities).

Antenna length is usually chosen in order to satisfy specific requirement on radiation efficiency. In fact, given α, usually a good design approach is to look for a radiation efficiency around $0.90 - 0.95$, with the remaining part absorbed by the load [45]. Given $P_r(z)$ the power radiated along the LWA:

$$\frac{P_r(L)}{P_r(0)} = e^{-2\alpha L} = e^{-4\pi\frac{\alpha}{k_0}\frac{L}{\lambda_0}} \tag{6.30}$$

from where it appears that α and L should not be decided arbitrarily. Radiation efficiency is then given by:

$$\eta_r = 1 - e^{-2\alpha L} \tag{6.31}$$

Going back to relation 6.23, one has that the radiated power flow is stronger from areas closer to the feeding point for forward propagating waves. In case of backward propagating waves, group velocity is still directed along positive z direction, whereas phase velocity is directed in the opposite direction. Although in this case β_x is still positive, α_x is positive as well and in this case the fields are called *proper*, since they attenuate moving far from the source. In both cases power leakage is more intense close to the antenna feeding, only the phase shift of the radiated field will be different in the two radiation mechanisms. The same reasonings can be applied in case of periodic LWA, where the first negative harmonic can be proper or improper depending on which radiation quadrant is chosen. For centre fed LWA the TM_1 field at $x = 0$ is given by:

$$E_y(0,z) = E_y(0,0)e^{-jk_z|z|} \tag{6.32}$$

and in this case field is propagating from $z = 0$ to $z = \pm\infty$. In this case, radiation takes place within a cone defined by an angle θ_0 (starting from yz

plane). For angles $\theta_0 < \theta < \pi/2$ a shadow region appear, *shadow boundary*, in which field intensity is strongly reduced. The TM field distribution in 6.32 can be calculated as:

$$E_y(x,z) = \frac{1}{2\pi} \int_{-\infty}^{+\infty} \tilde{E}_y(0,k'_z) e^{-jk'_x x} e^{-jk'_z z} \, dk'_z \tag{6.33}$$

where the Fourier transform on the aperture is:

$$\tilde{E}_y(0,k'_z) = A \left[\frac{2jk_z}{k'^2_z - k^2_z} \right] \tag{6.34}$$

with the vertical wavenumber given by $k'_x = \sqrt{k_0^2 - k'^2_z}$, that can be either a positive real number or a negative imaginary number [43].

6.3.1 Field Behaviour in Periodic LWA

A previously mentioned this antenna exploits a travelling wave, whose fundamental mode is slow and periodically modulated along thee structure. Because of Floquet theorem, the modal field can be expanded in a Fourier series as follows:

$$\mathbf{E}(x,y,z) = \sum_{n=-\infty}^{\infty} \mathbf{A}_n(x,y) e^{-jk_{zn}z} \tag{6.35}$$

with

$$k_{zn} = k_{z0} + \frac{2\pi n}{d} \tag{6.36}$$

wavenumber of the n-th Floquet harmonic. Fundamental mode has $k_{z0} = \beta_0 - j\alpha = \beta - j\alpha$. Radiation is achieved provided that the LWA unit cell periodicity is well designed (see later) and that one of the high order space harmonics is a fast wave, usually the space harmonic with $n = -1$. In this case the first negative harmonic wavenumber is the one of a fast wave, therefore: $-k_0 z < \beta_{-1} < k_0$ with $\beta_{-1} = \beta_0 - 2\pi/d$. The beam direction is automatically controlled by means of frequency from backward to forward endfire. Provided that, $n = -2$ space harmonic must remain a slow wave with $\beta_{-2} < -k_0$ as well as the fundamental tone with $\beta_0 > k_0$ [43]. This condition requires two constraints: the first regards the LWA unit cell periodicity that must be decided so that $d/\lambda_0 < 1/2$, where λ_0 is the wavelength corresponding to the higher forward endfire frequency [44]; the second condition is a limit on the effective relative permittivity experienced by the guided mode. For a TEM mode one has:

$$\epsilon_r^{eff} > 9 \tag{6.37}$$

that is equivalent to the condition $\beta_0/k_0 > 3$ [44].

In general, broadside radiation can be challenging to be achieved by means of LWA, since this beam direction corresponds in frequency to the *open stopband* of the periodic structure, at which: $\beta_{-1} = 0$ that is $\beta_0 d = 2\pi$ (FBZ edge). The name comes from the fact that at this frequency the harmonic $n = -1$ would radiate, though this is not possible since the attenuation constant α drops to zero. What happens is that a perfect standing wave ideally sets up within each cell (each cell is in phase with the others) of the periodic structure, without radiation. [to be clarified] As a matter of fact, in

LWA with pure series or shunt radiating elements only, stop-band problems cannot be reduced effectively [44]. A solution to avoid this is to put two radiating elements per each cell, spaced by d/4 or to use *composite right/left-handed metamaterials*, CRLH metamaterials, in which radiation occurs from the fundamental and scanning is continuous from endfire to broadside [43].

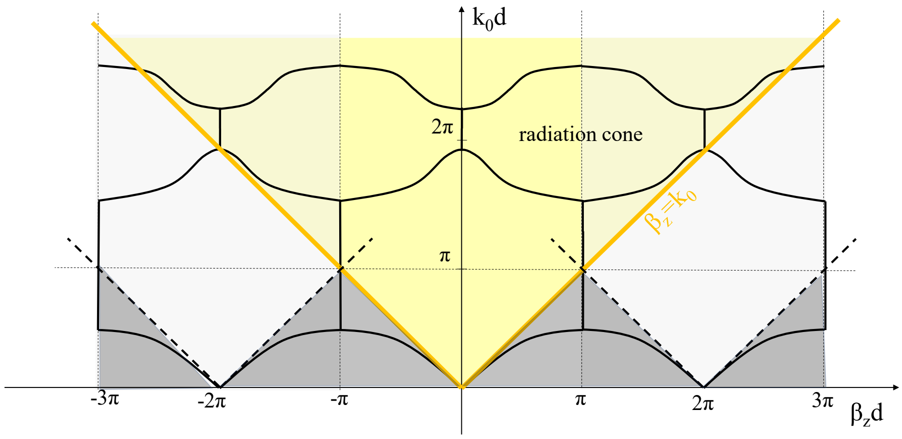

Figure 6.3: Brillouin diagram plotted as k_0d vs β_nd in which shadow and radiation region are highlighted. Radiation cone is defined above the solid yellow lines.

Brillouin diagram, BD, can be used to identify at which frequency, guided modes radiate. As mentioned in chapter 5, the plot for each n-th mode, is shifted by 2π from the others. Moreover, Floquet theory suggests that it is sufficient to print the diagram within the FBZ to obtain all necessary information about the modes sustained by the periodic structure. Figure 6.3 shows the BD for the n-th harmonic.[3] The bold lines represent the *light line*, defined by the linear relation $k_0 = \beta_n$. Basically, it divides the BZ into two regions: one above the cone, where fast modes radiate, being *coupled* to the surrounding medium modes, the *radiation region*; one underneath the cone (shaded area), in which modes are *bounded*, o slow and cannot propagate. The diagram indicates that if a mode has frequency high enough, hence $k_0d > \pi$, it is a leaky mode.

Graph in figure [DD n=0 and n=-1] may help in understanding some of the concepts presented above. As it appears, mode $n = 0$ phase shift starts from $\beta_0d = 0$ reaching at $\beta_0d = \pi$ the *closed stop band*, that is usually located below light line. Basically, this means that the mode is bounded and non-leaky, even if β_0d is not perfectly constant and the stop-band is not well defined. In particular, the condition is equivalent to have a perfectly shielded periodic structure, then *closed* without possibility of radiation leakage. Actually, in this region fields are reactive with an evanescent decay from the guiding structure.

The *open stop band* occurs instead for $\beta_{-1} = 0$ (the same as $\beta_0 = 2\pi$), in this region there is a sharp phase shift transition and a fast variation of the attenuation constant, that is null at the *stop-band null points*. Propagation,

3 The BD shows k_0d, not ω, as a function of the phase shift β_nd. The two representation are equivalent.

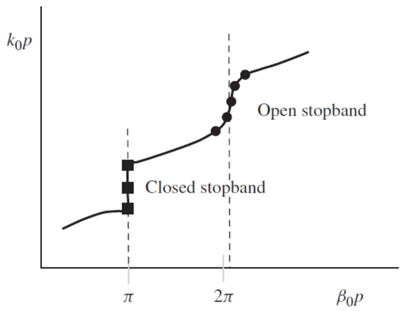

Figure 6.4: Closed stop band occurs at $\beta_0 = \pi$, corresponding to bounded modes. Open stopband occurs around $\beta_0 = 2\pi$, where radiation is possible [43].

along with loss, produces then leaky wave radiation, i.e. $\beta_{-1} \neq 0$ and $\alpha \neq 0$. Moreover, modes are proper when $\beta_{-1} < 0$ and improper when $\beta_{-1} > 0$.

In addition, to obtain the scan angle for a given frequency, relation 6.28can be adapted as follows:

$$\cos\theta_0 \approx \frac{\beta_{-1}}{k_0} \quad [\text{rad}] \tag{6.38}$$

Hence, by substituting $\beta_{-1} = \beta_0 - 2\pi/d$:

$$\cos\theta_0 \approx \frac{\beta_0}{k_0} - \frac{2\pi}{k_0 d} \tag{6.39}$$

that exhibits the possibility to change the beam direction depending on how the right hand side elements compare to each other [45].

Part III

DESIGN AND SIMULATION

7 DESIGN AND SIMULATION OF SINGLE-LADDER RBE RADIATING OSCILLATORS

7.1 MOTIVATION

Is it possible to design an RF periodic structure based distributed oscillator, whose topology allows also to have acceptable radiation? To give an answer to this question it is necessary to recall that a device capable of performing this task should be able to:

1. Exhibit a high Q-factor in order to have a sharp frequency response at the required oscillation frequency;
2. Exhibit low conduction losses, in order to maximise the time during which power is maintained inside the resonant structure;
3. Exhibit high radiation losses in order to increase radiation efficiency (along with low conduction losses);
4. Exhibit, depending on the application, a large area in order to improve gain and beamwidth.

As it appears, the first two conditions stated above are in antithesis with 3 and 4. In fact, 1 and 2 are necessary conditions to have a good oscillation. A large Q-factor is hallmark of good frequency selectivity and a small amount of loss insides a resonant structure. Moreover, it is worth to recall, that the energy "flow" into an oscillating ideal LC circuit is purely reactive. This result can only be achieved by compensating the resistive part of the resonator input impedance and requires the employment of low loss technologies. In case of monolithic or hybrid microstrip technology, this is translated into substrates with low *loss tangent*, δ_L, and very good conductors for the metal layer [36].

On the other hand, a good radiating device, i.e. an antenna, is usually a lossy structure, in which radiation losses are preferred and maximized with respect to conduction and substrate losses [42]. The measure of how good a radiator operates is the radiation efficiency, close to 1, if loss if unwanted loss is minimized. Basically, this parameter quantify the amount of input power that is converted into radiated power. Besides condition 3, 4 Moreover, antenna gain can be somehow related to the area occupied by the radiating elements [42]. Unfortunately, larger circuit are translated in higher conduction losses. Therefore, condition 3 requires something obviously in contrast with 1 and 2.The obvious conclusion is that a compromise between the above requirements must be found.

In chapter 2 and 5 it has been presented how periodic structures and EPDs can help in achieving high performances in oscillators, resonators, sensors and even antenna designs. In particular, the following sections of this chapter are focused on the realization of two different oscillator topologies in which an interdigital capacitor is used either as resonant unit and radiating element. Both the topologies are designed so that RBE oscillation is preferred:

- RBE oscillator at $\beta d = 0$: in this case the oscillation frequency $f_e 0$ close to the frequency at which the $n = -1$ Floquet harmonic eigenvalue exhibits a degeneracy, at the centre of the FBZ.
- RBE oscillator at $\beta d = \pi$: in this case the oscillation frequency $f_{e\pi}$ is located in the neighbourhood of frequency at which the $n = -1$ Floquet harmonic eigenvalue exhibits a degeneracy, at the edge of the FBZ.

Whether the former design uses a straight ladder, in which all the capacitors are aligned in the same direction, the latter employs a folded structure. The reason of this difference stands is explained in section 7.3. The main difficulty operating close to stopband edges is that a quasi-standing wave is present in the circuit, ideally carrying no power except reactive one and making radiation not efficient. However, the proposed designs tries to exploit the *array* as a leaky wave antenna[1], radiating in broadside direction. Both the structures present subwavelength designs in which the area occupied by the interdigital capacitors is maximised, in order to increase, if possible, the radiation resistance.

7.2 RBE OSCILLATOR AT $\beta d = 0$

In chapter 3 it has been presented how an interdigital capacitor can be used as resonant unit cell into a periodic structure, in order to realise a distributed resonator. What allows the use of such a circuit in microwave technology for this purpose, is the presence of a parasitic inductance and resistances at RF frequency. Besides, two access line must be provided to each resonant unit, adding so an equivalent LC circuit at both sides. The resulting unit cell is a complex LC circuit whose parameters could be extracted by means of formulas reported in [32]. The same circuit could also be considered as a high order filter, for which design parameters and figure of merit are difficult to extract since expression are somewhat cumbersome.

The reasons why a series interdigital capacitor is chosen comes from the fact that it desired to The reason why a series interdigital capacitor is chosen as resonant unit are:

- It acts as high pass filter, therefore all the possible oscillation frequencies below a certain value are rejected;
- The topology can be compact (short) along the signal direction of propagation;
- Capacitance can be increased playing on fingers width and number, rather than their length;

1 The structure is not properly an array, since the devices has no signals fed at the input. However in the following it referred as an array, for simplicity.

- Simplicity of implementation.

On the other hand, this technology brings some drawbacks:

- The circuit model is cumbersome and simplifications may not be possible;
- Using small fingers (length or width below 0.1 µm) the effect of technology tolerances could become significant.

In order to obtain high capacitance value with a large occupied area an high dielectric constant is required. Moreover, small dielectric losses are required, meaning that loss tangent must be limited. Rogers RO6010 has been chosen as substrate [46], since its applicability to high frequency ranges. The main technological parameters are reported in table 7.1. The design is carried on

Table 7.1: Rogers RO6010 main technological parameters.

Quantity	Symbol	Value	Units
Dielectric permittivity	ϵ_r	10.7	
Dielectric loss tangent	δ_d	0.0023	
Metal layer thickness	t	18	µm
Substrate height	h	127	µm
Copper conductivity	σ	5.8×10^7	S/m

using Keysight Advanced Design System (ADS) and CST Microwave Studio.

7.2.1 Unit Cell Design

The design of the interdigital capacitor, figure 7.1a, is started by using a symmetric structure, with the two microstrip lines having the same width and length. The access lines are directed along the x axis, whereas the capacitor extension develops along the y axis. The capacitor is extended along one preferred direction in order to:

1. maximize the number of fingers;
2. minimize the radiated electric field along the y direction;

The two requirements are related to each other. Suppose to connect a voltage source to one side of the capacitor at $x = 0$ and to ground the other side, the instantaneous electric field distribution would be the one in figure 7.1b. Supposing that every dimension of the device is short with respect to the guided wavelength, one can notice that the electric fringing field on the long sides of each finger is in opposition of phase to the one distributed on the long sides of the neighbour fingers, so that this components are cancelled. On the other hand, the electric field on the width of each finger sums up to the other, representing the main source of radiation. Actually, having a leaky wave, radiation would be distributed along the whole structure, though losses along

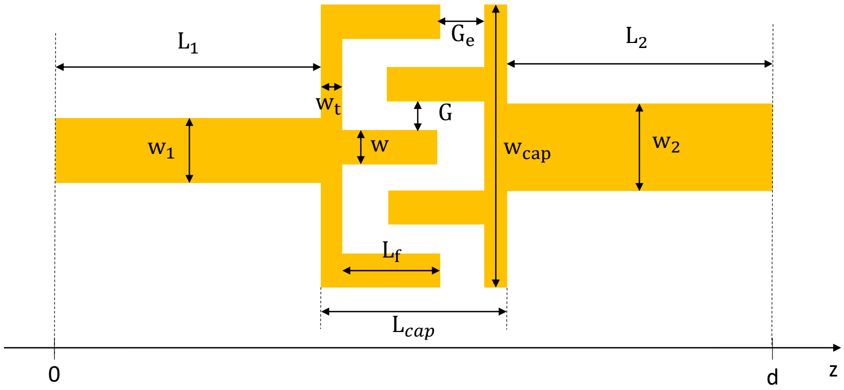

(a)

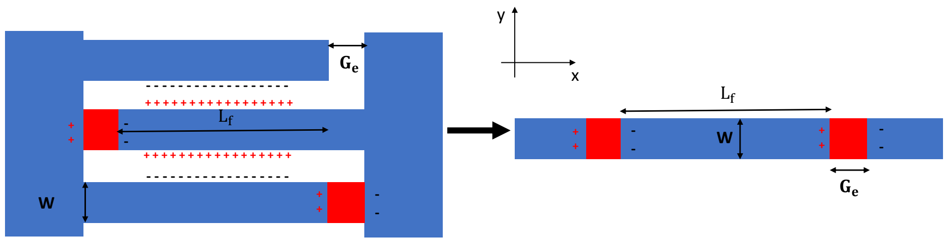

(b)

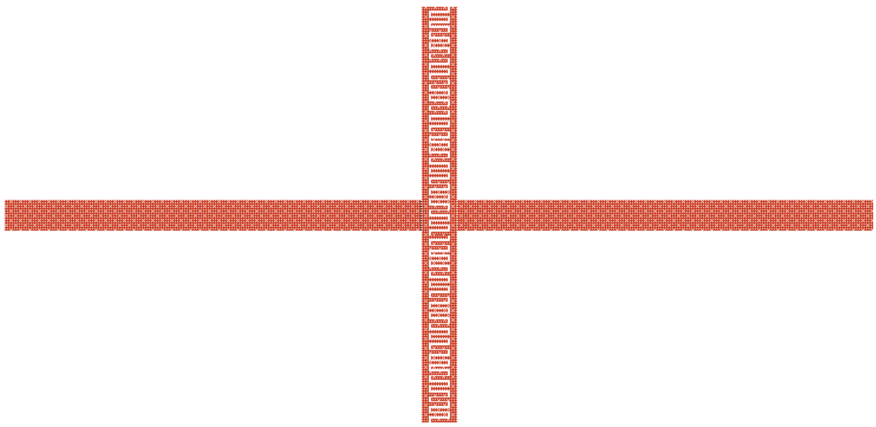

(c)

Figure 7.1: (a) Interdigital capacitor microstrip printed model. (b) Simplified model for describing radiation from interdigital capacitor fingers. (c) Layout of the symmetrical unit cell realised in ADS with the parameters in table 7.2.

the lines are considered negligible for now. If the approximation above is valid each pair of fingers can be considered as a unique radiator. Referring to the circuit in figure 7.1a, the geometrical parameter for the symmetric unit cells are reported in table 7.2. Using ADS, the circuit layout is generated and simulated by means of Momentum Microwave simulator (method of moments simulator), in order to keep into account every kind of loss

Table 7.2: Symmetric unit cell design parameters. The total number of fingers is N_p=80.

Quantity	Value [mm]	Quantity	Value [mm]
w	0.200	L_1	23.975
G	0.100	w_1	1.800
G_e	0.125	L_2	23.975
w_t	0.400	w_2	1.800
L_f	1.000	d	50.000
w_{cap}	23.900		
L_{cap}	2.050		

present in the circuit (simulation parameters are provided in appendix E). The same circuit is also simulated by means of a its circuital model (circuit model provided by ADS) in order to have a comparison with the lossless circuit. Notice that the outcome of this kind of simulation is a touchstone file, therefore the circuit is represented by means of its scattering parameters in a broadband frequency range. Starting from this representation, the transmission matrix of the system $\underline{\mathbf{T}}$ is extracted by converting the S-parameters in ABCD parameters. After that, the dispersion diagram is therefore calculated referring to the theory presented in chapter 5. Figure 7.2 shows the main results obtained from the simulation of the symmetrical unit cell. As it appears in figure 7.2a the circuit presents a first passband located in the frequency range $PB_1 = [0.65, 0.9]$GHz and after a large stop band a second pass band in the frequency range $PB_2 = [1.9, 2.1]$GHz. Whereas the former is related to the fundamental Floquet harmonic($n = 0$), the latter is due to the $n = -1$ spatial harmonic. In particular PB_2 is the stop band in which this design is interested in, being the first Floquet mode above the light line (red line), therefore representing a leaky mode. The quantity $\det(\underline{\mathbf{U}})$ is a measure of how close the eigenmode of the system are close to each other (as presented in chapter 5). The quantity is close to zero around the edge frequency of PB_2 meaning that these points could be suitable for looking for an RBE. Previously, it has been mentioned that the Bloch impedance is the characteristic impedance of an infinite periodic structure (transmission line equivalent). Moreover, since the structure is symmetrical, one has $Z_B^+ = Z_B^-$. In practice it is not feasible to operate with such systems, and the first approximation is to use a discrete number of unit cell. However, By incrementing enough the number of cells, the input impedance of the discrete structure approaches the Bloch impedance becoming a good approximation for this quantity (an example is reported in picture 7.3). Looking at figure 7.2b it is possible to notice that a zero of $\mathrm{Im}\{Z_B\}$ is located close to PB_2 centre ($\beta d \simeq \pi/2$), meaning that the oscillation frequency may not be close to the ideal RBE. This fact suggest that this topology may not be ideal for the purpose of this design (the proof of this fact is given in section [oscillation of structure]).

To overcome this problem and improve the frequency selectivity another design is proposed. In this case an asymmetrical unit cell is employed. The need of an asymmetry comes from the fact that it is not possible to move

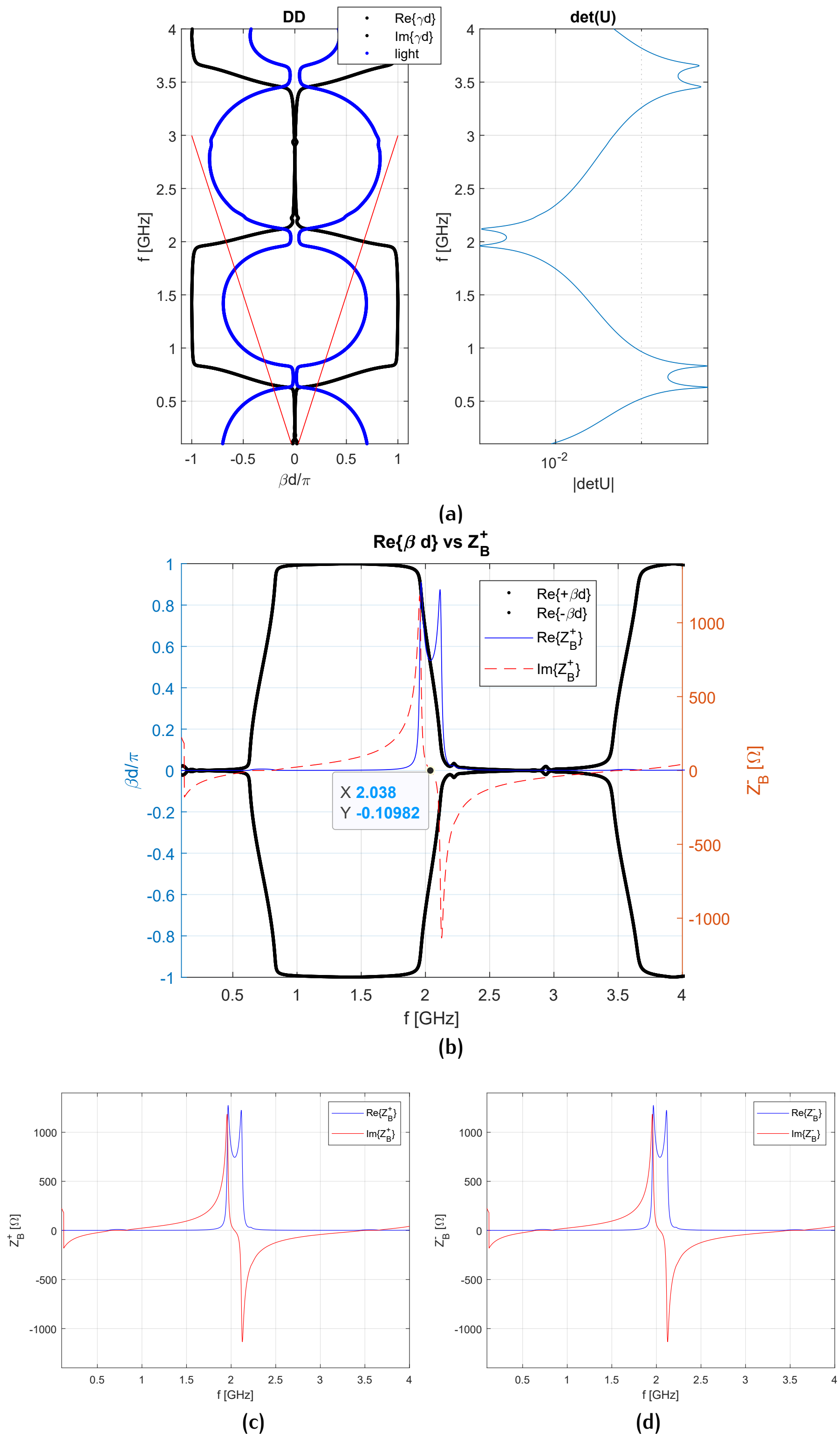

Figure 7.2: (a) Dispersion diagram for the lossy symmetrical unit cell (table 7.2). (b) $\beta d = 0$ and Z_B are compared. (c)(d) Bloch impedance for the forward and backward propagating mode.

the zero of $\text{Im}\{Z_B\}$ to the edges of the passband by simply modify the various aspect ratios of the interdigital capacitor. Table 7.3 reports the design parameters for the new cell; the extracted circuit is instead shown in picture 7.4.

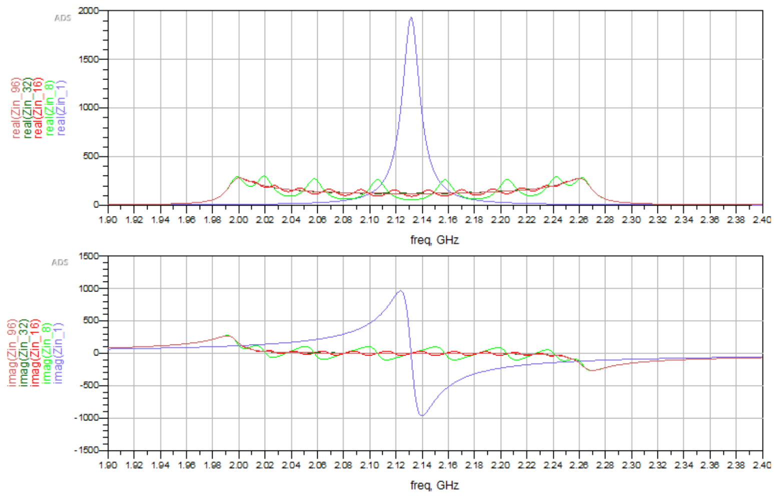

Figure 7.3: Input impedance of the cascade of 8, 16, 32, 96 uni cells (last cell terminated on a short circuit).

The circuit has been simulated with both method of moment microwave (MoM MW) and method of moment RF (MoM RF). The former takes into account all the losses present in the cell, whereas the latter only considers conduction and dielectric losses. The MoM RF simulation is useful to consider the ideal behaviour of the unit cell, that is close to the behaviour of a lossless system and the results are shown in figure 7.5.

As it appears from the comparison of the DD for lossless (figure 7.5a) and the lossy (figure 7.6a) unit cell, the dispersion changes accordingly to the theory previously presented. In fact, considering the lossy case, no more degeneracy is visible close to passbands edges, due to the perturbation introduced by loss. Moreover, Bloch impedance behaviour approaching stopbands changes dramatically for the two cases. In particular, a significant reduction for both real and imaginary part modulus is appreciable with full loss. On the contrary, the frequencies for which $\text{Im}\{Z_B^+\} = 0$ remain almost constant. In addition, the new asymmetric design exhibits some different

Table 7.3: Symmetric unit cell design parameters. The total number of fingers is N_p=60.

Quantity	Value [mm]	Quantity	Value [mm]
w	0.200	L_1	8.088
G	0.100	w_1	0.700
G_e	0.163	L_2	8.088
w_t	0.250	w_2	1.62
L_f	1.000	d	18.000
w_{cap}	17.900		
L_{cap}	1.825		

features with respect to the symmetric one. In particular, by looking at figure 7.6 it is possible to notice that:

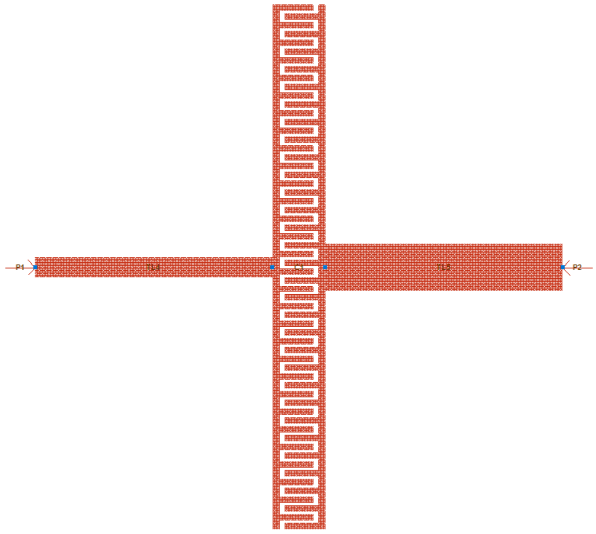

Figure 7.4: Layout of the asymmetrical unit cell extracted in ADS with parameters in table 7.3.

- The two passbands have been shifted and reduced shrank. Now, $PB_1 = [1.1, 1.25]\text{GHz}$ whereas, $PB_2 = [2.4, 2.5]\text{GHz}$. This effect is probably due to the lower capacitance obtained by reducing the number of fingers (now 60).
- The unit cell in shorter, therefore the portion of DD in which radiation is possible is reduced. In other words, the light cone is restricted. However, the $n = -1$ Floquet harmonic is still able to radiate within this region, close to the FBZ centre.
- $Z_B^+ \neq Z_B^-$ now, since the structure is not symmetric. Besides, the eigenmode are no more symmetric too (proof of this is reported in section [RBE section]). Notice that the frequency for which $\text{Im}\{Z_B^+\} = 0$ is now moved to one edge of PB_2, in particular toward the FBZ centre. Figure 7.6b shows exactly this behaviour.

The last feature of the new structure suggests that by cascading N cells, the input impedance of the circuit has a sharp frequency response around the frequency for which Bloch reactance vanishes.

7.2.2 Frequency response of the passive ladder circuit

Now that the unit cell is characterised, it is possible to build the discrete structure that is in charge to operate as distributed resonator. The circuit is built as a ladder, with N cascaded elements. The design is divided i two steps:

1. Simulating and characterising the discrete periodic structure by means of its circuit equivalent. The circuit is realized cascading N two-ports representing the S-parameters of the unit cell (figure 7.8a);

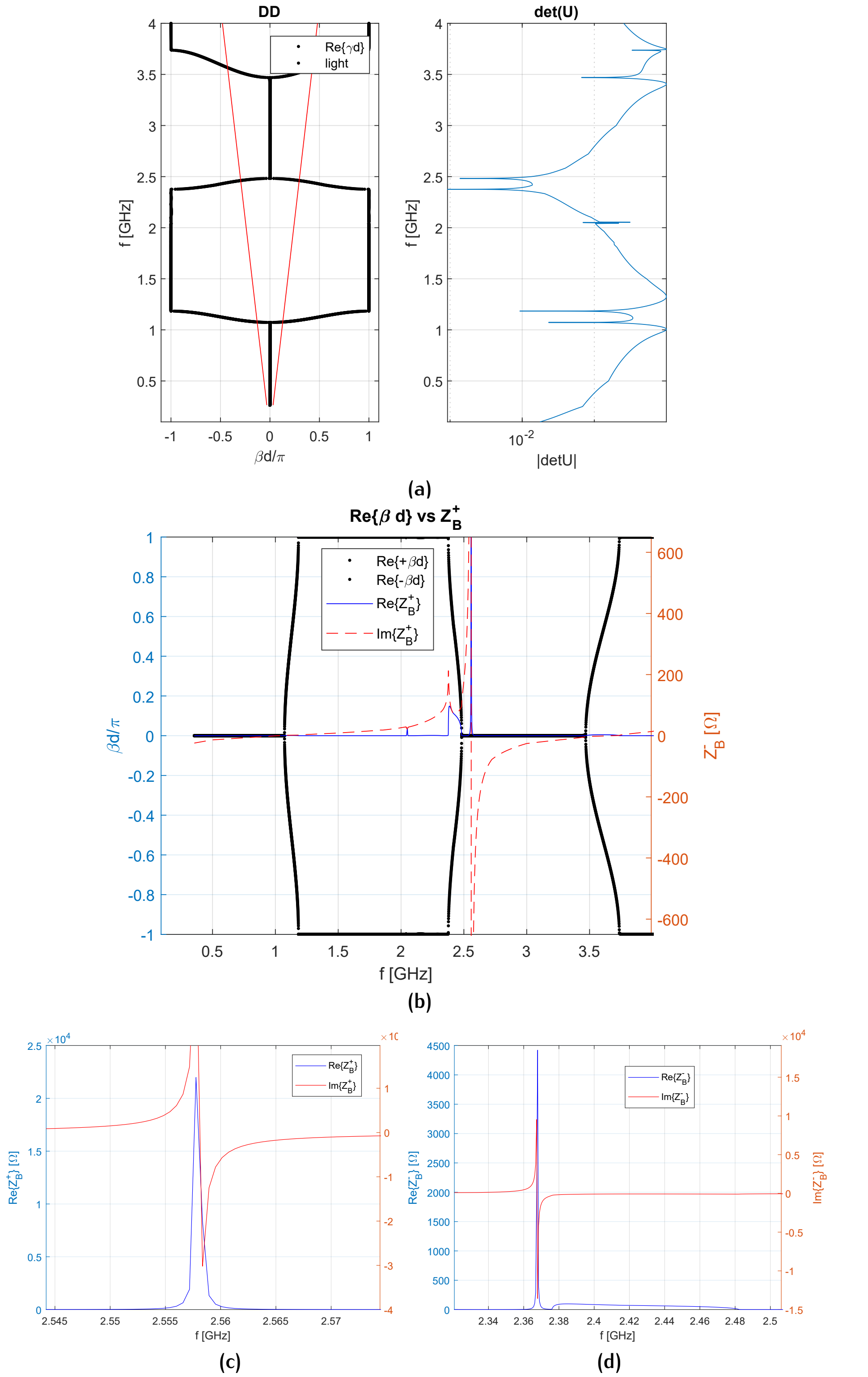

Figure 7.5: (a) Dispersion diagram for the asymmetrical lossless unit cell (table 7.3). (b) $\beta d = 0$ compared with Z_B. (c)(d) Bloch impedance for the forward and backward propagating mode.

2. Simulating and characterising the discrete periodic structure by means of full wave simulation.

Being the circuit a resonator, the first thing that is useful to know is its input impedance (admittance) and its frequency response (transfer function).

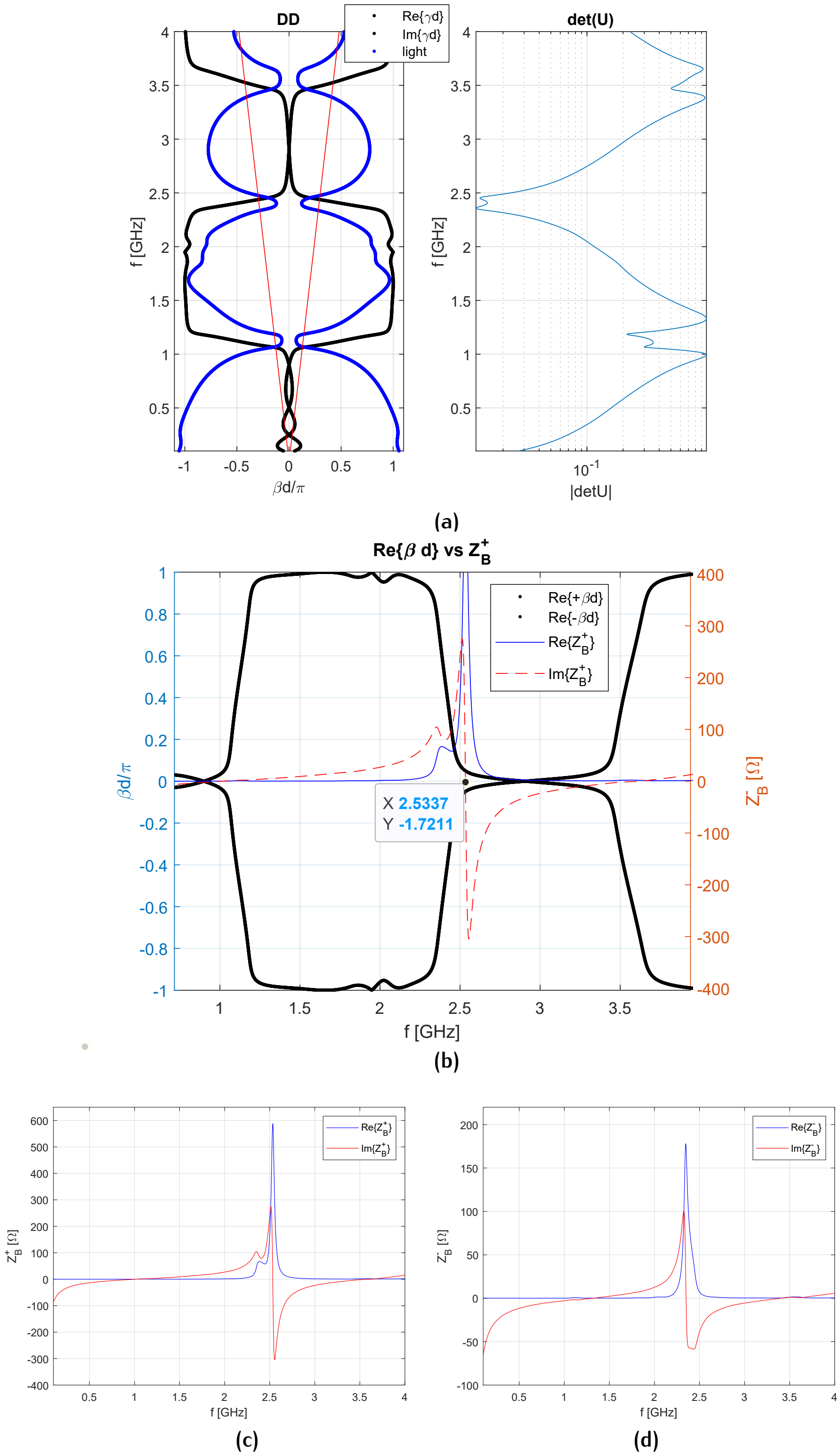

Figure 7.6: (a) Dispersion diagram for the asymmetrical lossy unit cell (table 7.3). (b) $\beta d = 0$ compared with Z_B. (c)(d) Bloch impedance for the forward and backward propagating mode.

In particular, figure 7.7a shows that the driving point admittance is stable varying the number of unit cells. The analysis is carried on by closing both terminations on $50\,\Omega$ excitation ports. As it appears, the main resonance frequency is located where the impedance change more rapidly close to res-

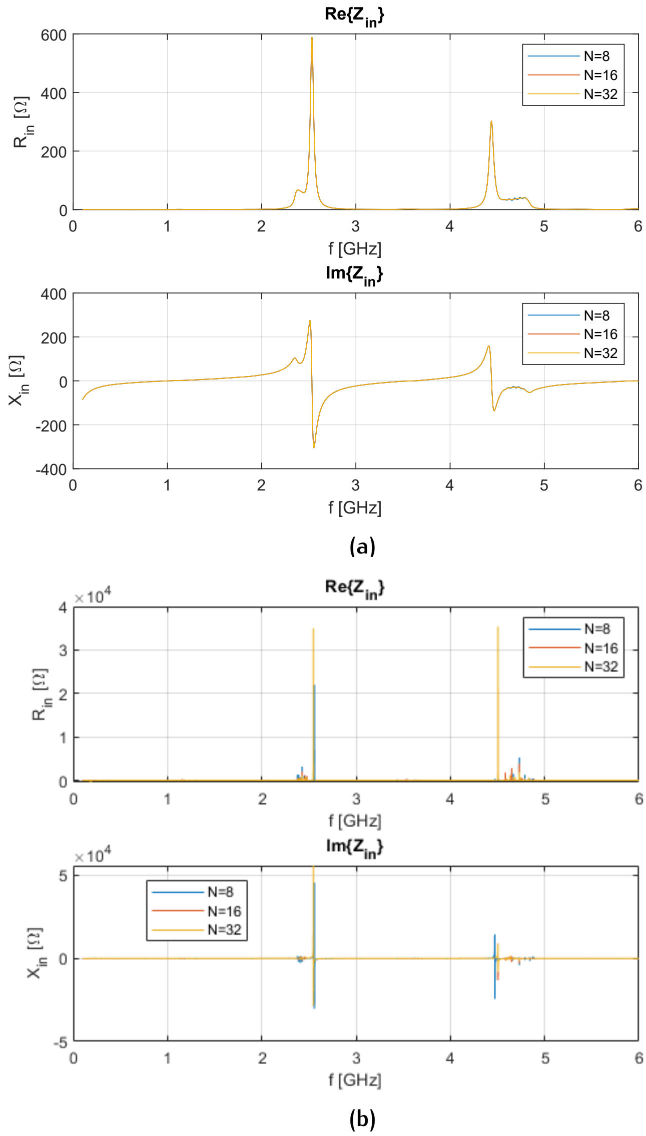

Figure 7.7: (a) Lossless structure. Discrete structure input impedance varying the number of unit cells: input resistance (above), input reactance (below). (b) Lossless structure. Discrete structure input impedance varying the number of unit cells: input resistance (above), input reactance (below).

onance at $f_{res} = 2.53\,\text{GHz}$ and this is valid for both the lossless (figure 7.7a) and the lossy case (figure 7.7a). It appears that more than one resonance frequency is present. However, using the circuit as resonant unit negative resistance device would be connected at its input port, that can be modelled with its Northon circuit equivalent. Supposing to reduce the output conductance of the device from zero to a finite negative value, the first value of input admittance that is compensated is the one corresponding to the maximum of the input impedance. It is worth it to recall that the presence of a resonance in the circuit is not a sufficient condition to have oscillation, as presented in chapter 5. Moreover, since the resonator is seen as a one-port from the outside, the input impedance is the resonator transfer function itself.

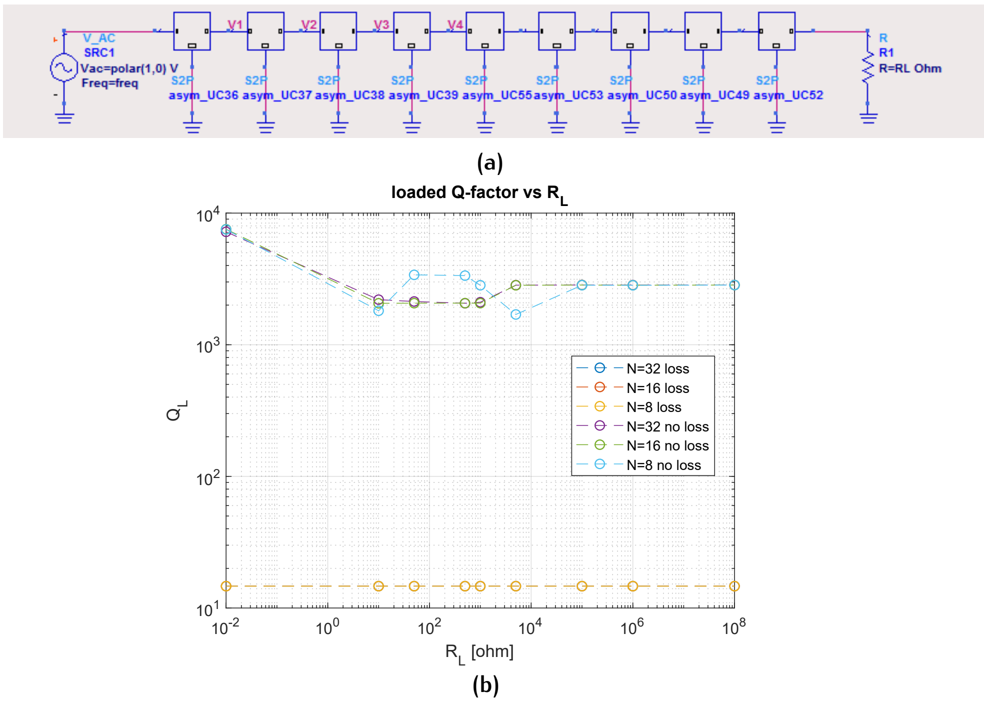

Figure 7.8: (a) Simulation setup in ADS for Q-factor evaluation (b) Total loaded Q-factor for the passive ladder structure.

Figure 7.8b shows the behaviour of the total Q-factor for the resonator. Since no analytical model is available for the circuit, the total Q factor have been calculated be means of equation 3.1.1 as:

$$Q_{tot} = \frac{f_{res}}{2\Delta f} \tag{7.1}$$

where Δf is the half power fractional bandwidth calculated at the input of the circuit. The lossless structure shows a Q factor close to 7000 for a short circuit, whereas it becomes almost constant approaching 2200 by introducing larger loads. On the contrary, the lossy structure shows a constant value, well below the lossless case, probably because of the large amount of loss present in the system. Moreover, it can be noticed, that $Q_L \simeq 14.50$ in the second case, regardless the value of the applied load. This relatively low value is not representing a problem for the oscillator operation, as it is presented in the next section. Although the behaviour of the structures in different, it is possible to conclude that:

- Using a number of cell $N \geq 8$ a discrete structure of this kind present almost constant loaded Q-factor.
- A short circuit appears to be the best possible load.
- Resonance is expected around $f_{res} = 2.5\,\text{GHz}$, close to the upper edge of PB_2.

7.2.3 Active single-ladder circuit and RBE

Now that the passive resonator is characterized, one step further is to add an active device in order to obtain oscillation. To do this, an ideal non linear

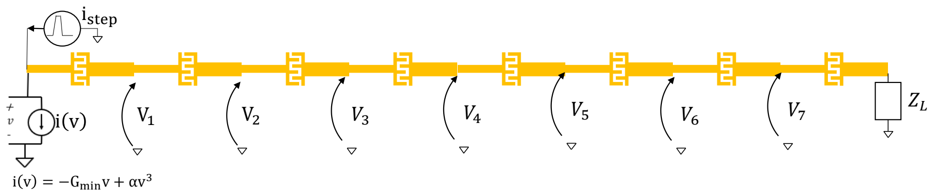

Figure 7.9: Block scheme for the time domain simulation of the circuit with asymmetrical unit cell.

source is connected in parallel at the input of the N cell ladder and a time transient simulation is performed (figure 7.9 shows a sketch of the whole circuit.). From Kurokawa condition for the input admittance one has:

$$G_s(f_{res}) = -G_{in}(f_{res})$$
$$B_s(f_{res}) = -B_{in}(f_{res})$$

therefore the active device must introduce a negative gain equal to $-G_s(f_{res})$. Notice that in this case it is supposed to have $B_s(f_{res}) = 0$, meaning that only the resonant circuit is in charge of imposing the oscillation frequency and paving the way for further future analysis. Basically, the gain source acts as a negative non-linear conductance, whose output characteristic is:

$$i(t) = -g_s v(t) + \alpha v(t)^3, \qquad \alpha = \frac{g_s}{3}$$

Being an oscillator, the circuit is not receiving an input signal. In practice, noise, that has a wideband spectrum (see chapter 4), would start the oscillation, after a certain initial transient, whose duration cannot be define a priori. In this application a linear edge current step is injected at the circuit input port as initial condition. The parameters are: current high level $i_h = 1\,\mu A$, current low value $i_l = 0$, initial delay $t_d = 0$, rise time $t_r = 25\,ps$, fall time $t_f = 25\,ps$, hold time $t_h = 55\,ps$ and period $t_p = 10\,\mu s$. An example of the simulated circuit is reported in figure 7.9. Even in this case both lossless and lossy circuits are simulated. The main result from the transient simulation are reported in table 7.4 and figure 7.10 for the lossless case and table 7.5 and figure 7.11 for the lossy case, respectively. Considering the reported data it is now possible to analyse the obtained results.

Table 7.4: Main result from simulation of the 8 cells ladder lossless array.

Quantity	Symbol	Value
Expected resonance frequency	$f_{r,e}^{NL}$	2.558 GHz
Input conductance	G_{in}^{NL}	45.5 µS
Expected min. source conductance	$g_{s,e}^{NL}$	−45.5 µS
Actual oscillation frequency	$f_{r,a}^{NL}$	2.563 GHz
Actual min. source conductance	$g_{s,a}^{NL}$	−3.95 µS
Phase shift between cells	$\Delta\phi^{NL}$	−6.3 deg
Total Q-factor	Q_T^{NL}	1282
Oscillation start-up time	t_{su}^{NL}	58 µs

Table 7.5: Main result from simulation of the 8 cells ladder lossy array.

Quantity	Symbol	Value
Expected resonance frequency	$f_{r,e}^{L}$	2.534 GHz
Input conductance	G_{in}^{L}	1.70 µS
Expected min. source conductance	$g_{s,e}^{L}$	−1.70 µS
Actual oscillation frequency	$f_{r,a}^{L}$	2.535 GHz
Actual min. source conductance	$g_{s,a}^{L}$	−5.80 µS
Phase shift between cells	$\Delta\phi^{L}$	−8.2 deg
Total Q-factor	Q_{T}^{L}	422
Oscillation start-up time	t_{su}^{L}	38 ns

- For both the structure the actual resonance frequency is very close to the expected oscillation frequency. Figures 7.5b and 7.6b show that the oscillation takes place very close to the FBZ edge. This result is confirmed by figures 7.11c and 7.10c. In fact the voltage phase shift at the periodic structure nodes is small (in lossy case $\Delta\phi^{L} = -8.2\,\text{deg}$ and $\Delta\phi^{NL} = -6.3\,\text{deg}$ in lossless one). The small phase shift should produce a distortion in the waveforms giving a non monochromatic oscillation. However, spurious frequency components are located well far from f_r in both cases.

- The actual gain required to trigger the oscillation in larger than what is expected. Input susceptance vanishes close to, but not exactly, where the input admittance minimum is located, therefore, larger values are required.

- Waveforms are attenuated along the structure, by a an amount proportional to $e^{-\alpha(f_r)d}$ at each cell. Even if all the cells oscillates almost in phase, the voltage amplitude dramatically decreases moving toward the load (around some µm at the last node).

- The total Q-factor for the ideal oscillator is decreased. However, the lossy structure shows a Q-factor well above the value found for the isolated resonator. This is a typical benefit provided by the presence of an EPD [7].

The design has been started with the purpose of realising an RBE oscillator. As previously mentioned lossy discrete structures do not present EPD because pass and stopbands cannot be sharply defined. The addition of gain may eventually bring back the working condition close to an ideal operation even if perfect EPDs can not be retrieved. Consider now the circuit in figure 7.12a. From chapter 5 it has been presented that unit cell transmission parameters can be extracted by scattering parameter simulation. The reported circuit has to be intended as part of an infinite periodic structure in which the non linear current source acts as distributed gain element. Notice that S-parameters are simulated by exciting the circuit with a signal source whose amplitude is small enough to make non linearities negligible. There-

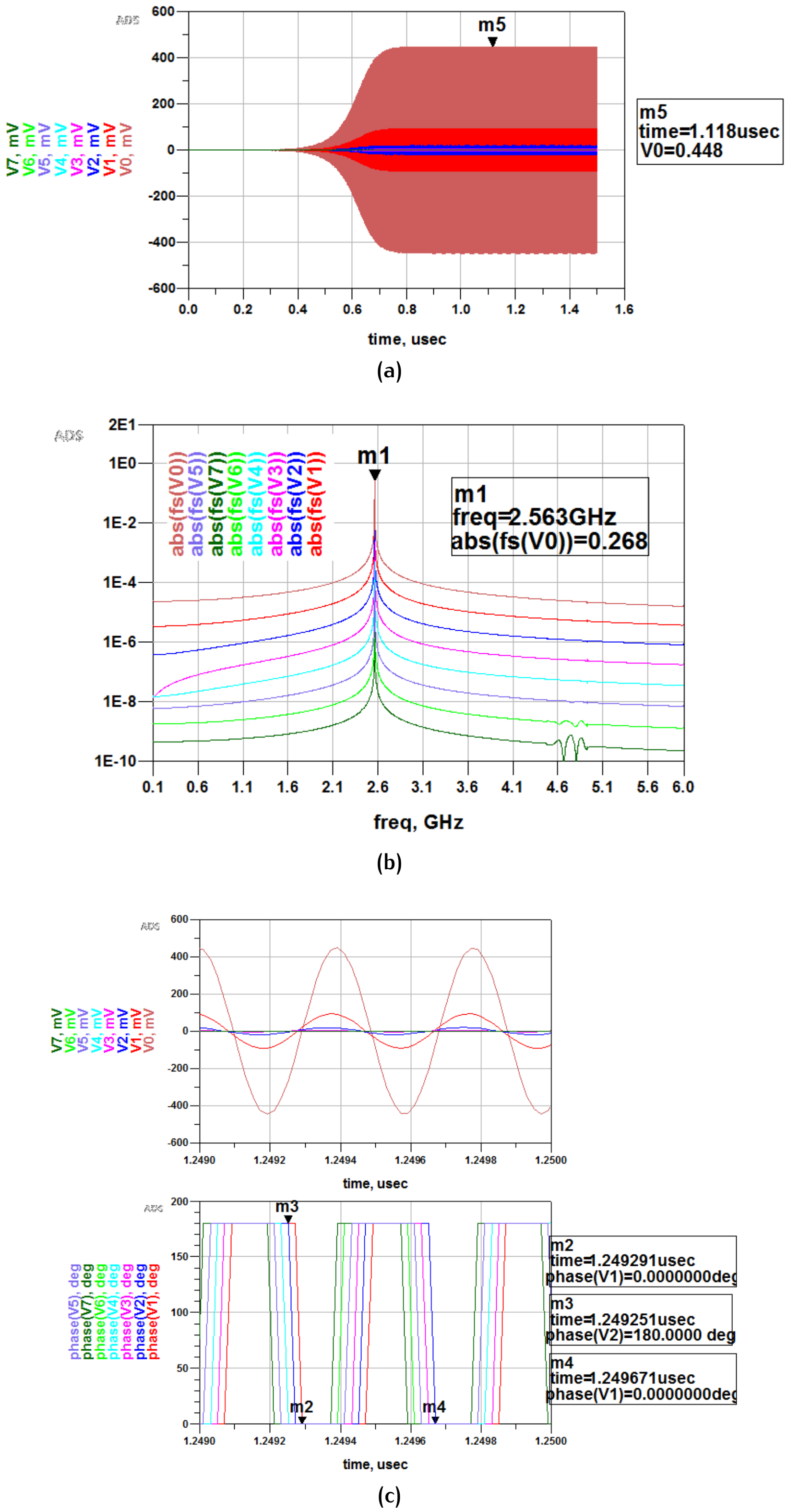

Figure 7.10: (a) Time domain response of the lossless ladder oscillator based on asymmetrical unit cell ($N = 8$). (b) Fourier transform of the time domain response shown in (a). As i appears the spectrum is very pure in a very large bandwidth. (c) Detail on the voltage wave form and to the associated phase.

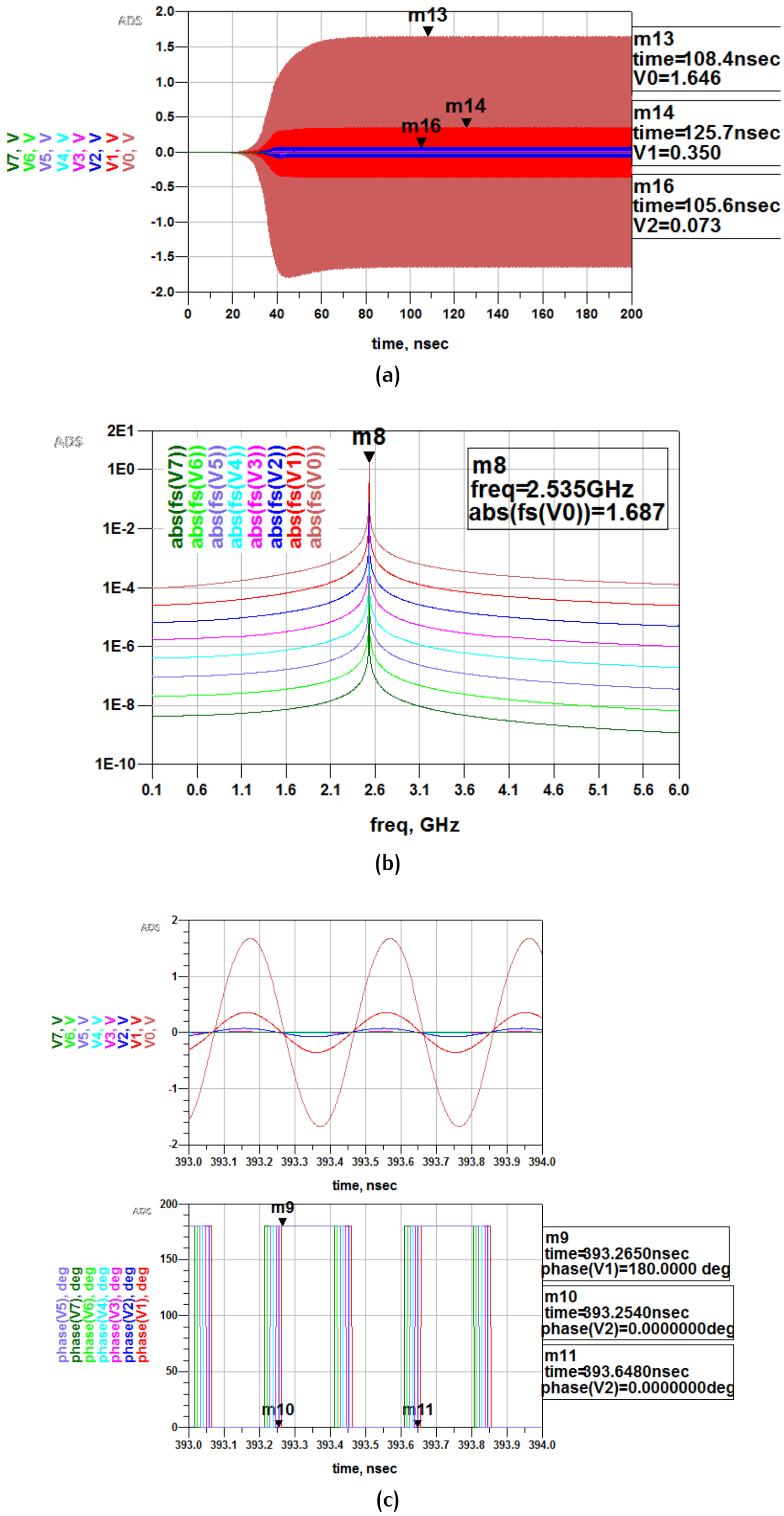

Figure 7.11: (a) Time domain response of the lossy ladder oscillator based on asymmetrical unit cell ($N = 8$). (b) Fourier transform of the time domain response shown in (a). As i appears the spectrum is very pure in a very large bandwidth also in the lossy case. (c) Detail on the voltage wave form and to the associated phase. The phase shift is

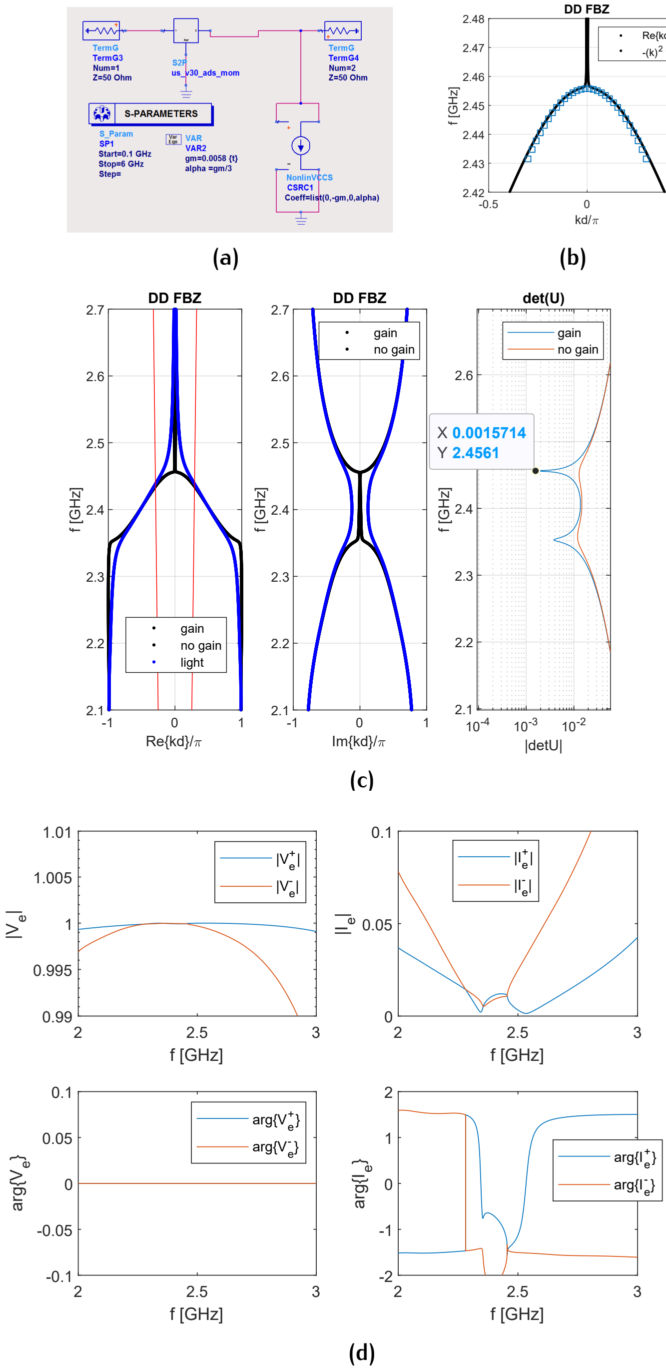

Figure 7.12: (a) Unit cell simulated with gain element. (b) Dispersion diagram for the unit cell with and without gain.

fore, the given current source can be actually modelled as a conductance resistor whose value is $-g_s$. By simulating the circuit it appears that the value of gain necessary to retrieve the degeneracy for both eigenvalues and eigenvectors is exactly $g_e = -5.8\,\mu\text{S}$. The chart in figure 7.12c shows this result. Notice that $\det(\underline{\mathbf{U}})$ is proportional to 10^{-3}, therefore both eigenvectors and eigenvalues show a non negligible value of degeneracy. The proof of the eigenvectors degeneracy is in figure 7.12d. Another proof of the presence of

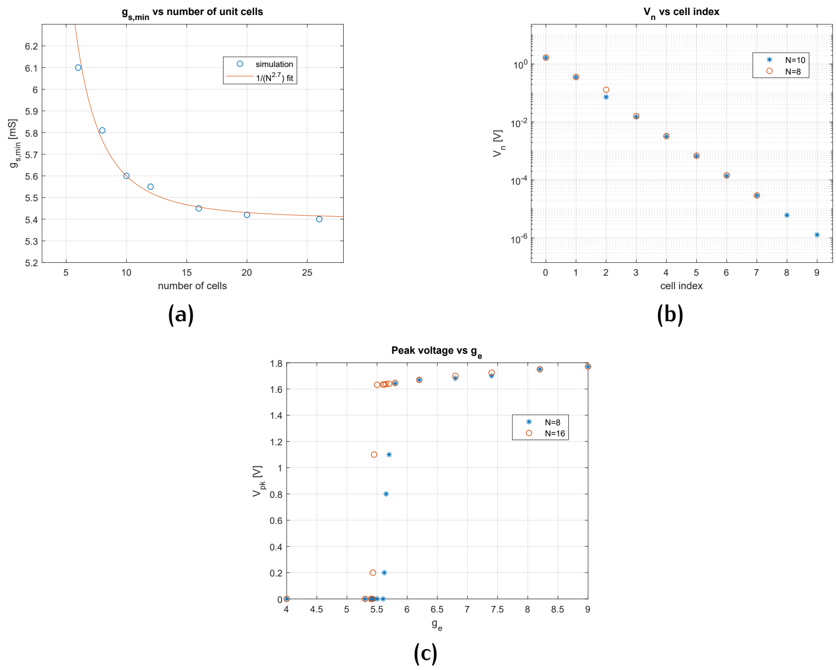

(a) (b) (c)

Figure 7.13: (a) g_s parametrization as a function of the number of cell. The driving admittance can is fit by $1/N^{2.7}$ suggesting the presence of a RBE. (b) Voltage exponential decay along the line for $N = 8, 16$. The voltage remains almost constant by varying the number of cells. (c) Peak voltage value is slightly changed by varying g_e.

a RBE is in figure 7.12b, in which it is shown how $\omega \propto -\beta^2$, showing hence the presence of a second order EPD [2].

The oscillation frequency for the discrete periodic structure is still not exactly located at f_e. The reason is that only in the input cell losses are recovered retrieving frequency selectiveness, whereas in the remaining part of the array oscillation is imposed by the first cell.

The minimum value of the transconductance varies by changing the number of cells employed in the structure. In particular, figure 7.13a shows that the the behaviour is proportional to $1/N^{2.7}$:

$$g_{s,min}(N) \approx \frac{0.1}{N^{2.7}} + 0.0054\,\mathrm{S} \tag{7.2}$$

the fitting function above is very close to results reported in literature, for example in [6], where it is shown that for RBE oscillators, the driving point admittance is proportional to $1/N^3$.

Figure 7.13b shows instead the variation of the peak voltage at each node of the array. The scale is logarithmic, and V_n linearly decreases suggesting an exponential decay. Furthermore, changing the number of cells slightly affect the voltage distribution at each node. Besides that, figure 7.13c shows that by increasing g_s of 10 % peak voltage changes of less than 2 %, provided that the variation is far from the threshold.

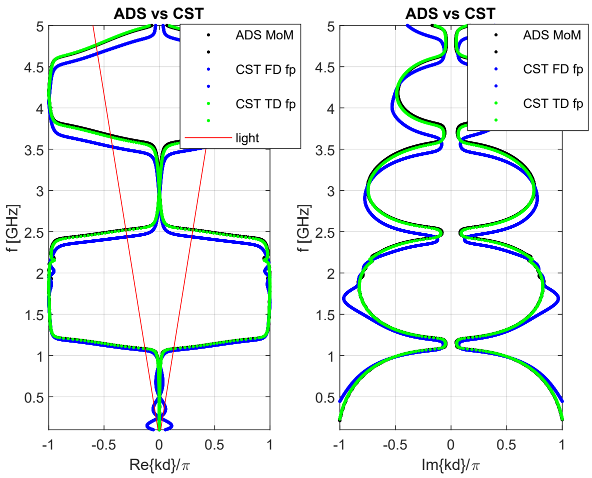

(a)

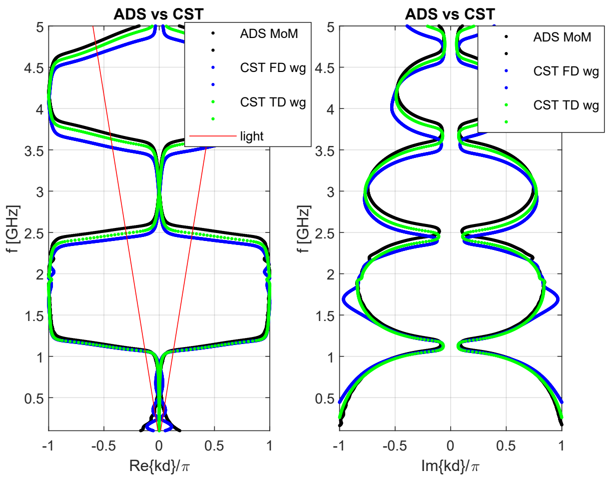

(b)

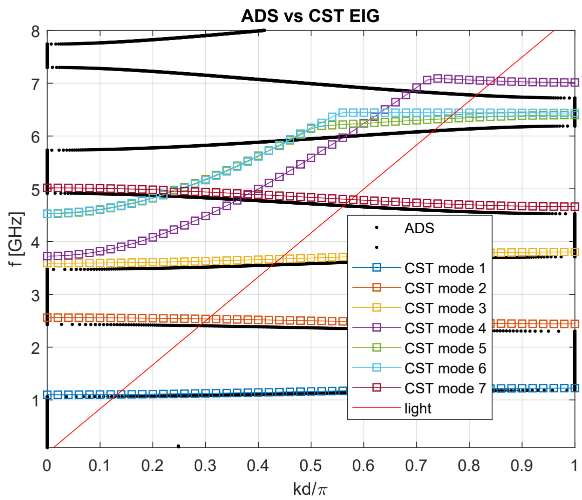

(c)

Figure 7.14: (a) ADS MoM simulation is compared with CST FD and TD solver with employing discrete face ports. (b) ADS MoM simulation is compared with CST FD and TD solver with employing waveguide ports and de-embedding the scattering parameters. (c) ADS lossless simulation versus CST eigenmode solver.

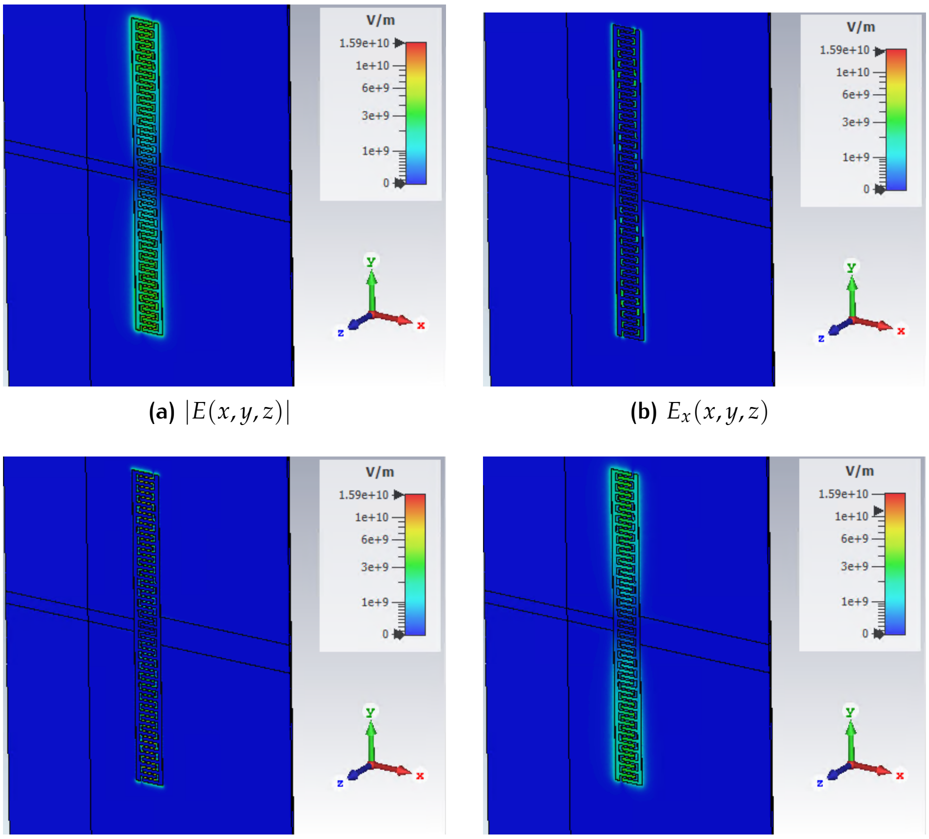

(a) $|E(x,y,z)|$ **(b)** $E_x(x,y,z)$

(c) $E_y(x,y,z)$ **(d)** $E_z(x,y,z)$

Figure 7.15: Mode 2: electric field distribution for interdigital capacitor at f_r. The high value of the electric field are non physical and due to the eigenmode solver, in which losses are ignored. A different color map is used in this plots in order to better understand the field distribution in the capacitor.

7.2.4 Modes Analysis

The unit cell is now analysed in order to understand how electromagnetic fields behave at various frequencies. In particular the next steps are focused on understanding the topology of electromagnetic modes around oscillation frequency and how they could eventually participate in radiation. In chapter 5 a formalism based on the transmission matrix method as been presented to study periodic structures. This method allows to obtain information about frequency and time domain response. Anyway, in this study the procedure has been strictly related to a circuital analysis until now, since each unit cell is modelled by its scattering parameters. [2] Full wave simulations carried so far are based on ADS MoM solver, that does not allow the direct calculation of eigenmodes. To confirm the validity of the ADS MoM solution, CST is employed with both frequency domain (FD) and time domain (TD) solvers. Excitations are provided with both discrete face ports and waveguide ports (simulation setup is in appendix E). Waveguide ports are located far from

2 The same analysis could be carried on by means of electromagnetic wave formalism [38], however the complexity of the geometry does not allow to define fields in the unit cell a priori and the calculation would be cumbersome and out of the scope of this study.

the unit cell and then scattering parameters are de-embedded at its inputs. All the CST simulations show a good agreement with the result obtained with ADS. In particular, DD from TD looks closer to DD from MoM than what is obtained from FD, for both discrete and waveguide ports.

To obtain a more comprehensive description of the EM fields CST MW Studio eigenmode solver (EIG) is employed (solver set up in appendix E). This kind of simulation allows to individuate higher order modes, that would not be visible by simulating the unit cell as two-port. The same information could be extracted by using a multi-mode waveguide port in fullwave simulation. However, ADS does not include this feature and CST frequency and time domain simulator would require a very large number of meshcells, along with very large computational resource demand and simulation time.

The outcome of the EIG simulation is reported in figure 7.14c. Since CST EIG solver does not take into account losses, the lossless circuit DD (no conduction, no dielectric, no radiation losses) is also plotted for comparison. A good agreement between the two solver is found for the eigenvalues of modes $1, 2, 3, 7$ that are related to the fundamental Floquet wave and its higher order spatial harmonics. The cut-off frequency for $n = 0$ spatial harmonic is located around 1 GHz for both the solver, whereas stop and passbands appear to be similar in amplitude for $n \neq 0$. Group velocity appears to be consistent in both the solver for this mode. As expected, harmonic $n = -1$ is a short wave whose phase velocity is negative approaching $f_e \simeq 2.6\,\text{GHz}$, where group delay tends to infinite.

The plot also shows the presence of three additional modes, namely number $4, 5, 6$, that could seem not expected given the previous results. They are short waves whose cut-off frequencies are well above f_r. They also exhibit a change in group velocity around $\beta d \simeq \pi/2$ for $5, 6$ and close to $\beta d \simeq 0.7\pi$ for 4. Close to these corner points, group velocity vanish and the quality factor of the system should increase, yielding strong resonance, leaving the possibility for following investigations. Moreover, the presence of intersections in modes 4 to 7 eigenvalues also predicts that energy can be exchanged among them at crossing points [39]. Finally, being the microstrip a quasi-TEM line [9], and although this modes arise above a certain frequency they are not detrimental for operation of the oscillator, as it will be shown.

Attention is now focused on mode 2, since it is responsible of carrying power in the oscillator close to f_r. Figure 7.15 shows the electric field distribution in the unit cell both in modulus and in the vector components. The electric field is mainly concentrated in the capacitor and in particular the maximum value is located at the end of the capacitor branches. For what concerns the three field components one can notice that E_x is mainly distributed along the external edges of the IC and in between the fingers, but only along the short sides. On the contrary E_y maximum is located in between the fingers longer side. It appears that the electric field is distributed as a standing wave along y. The circuit is not periodic in the y direction and no such an effect is expected. Anyway, it could be blamed to border effects due to the small substrate (the whole structure is heavily sub wavelength: $\lambda_r \simeq 125\,\text{mm} \ll w_{sub} = 38\,\text{mm}$, where w_{sub} is the substrate width[3]). E_z turns

3 It is importante to notice that the structure is periodic only in the x direction, therefore only there the periodicity of the cell is defined by the Bloch wave solution.

out to be the main electric field component. This fact confirms that a large part of the field can be coupled with the surrounding medium, generating a leaky mode. Recall that for leaky mode propagating on a periodic structure with negative group velocity, the generic field distribution is expressed as [43]:

$$E(x, y, z) = E_0 e^{+jk_x x} e^{-jk_z z} \tag{7.3}$$

Notice that the electric field maximum value is in the interdigital capacitor, with values touching $E_{max} \propto 10^{10}$V/m for the fringing areas in between the fingers. Besides, figure 7.16 shows that the electric field along the two access lines is four orders of magnitude below with respect to E_{max}. This strong field variation could be explained recalling that the lossless unit cell is very close to its resonance frequency, where the total Q-factor is $Q_{tot} \simeq 10^4$.

By comparing the field in figure 7.16 and 7.17 one can notice that the overall field distribution is neither a TE nor a TM, but rather a TEM, since all field components are non null for both **H** and **E** on the whole UC extension.

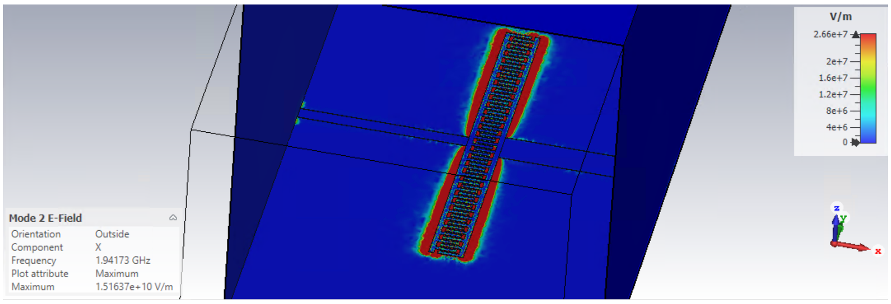

(a) $E_x(x, y, z)$

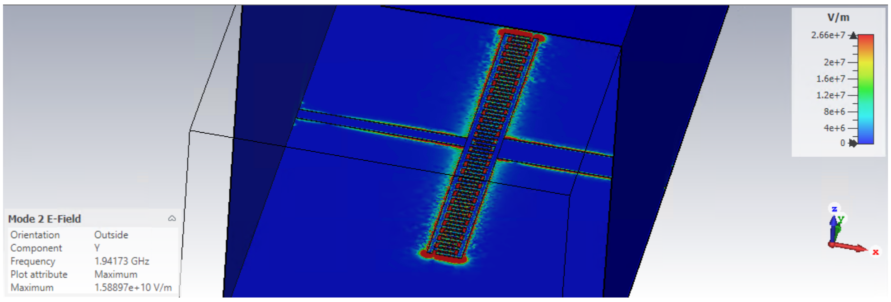

(b) $E_y(x, y, z)$

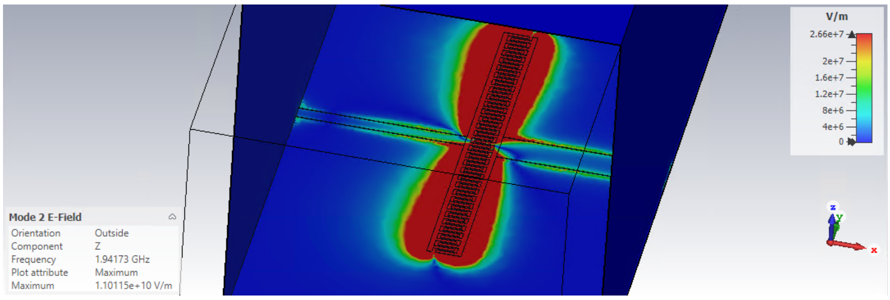

(c) $E_z(x, y, z)$

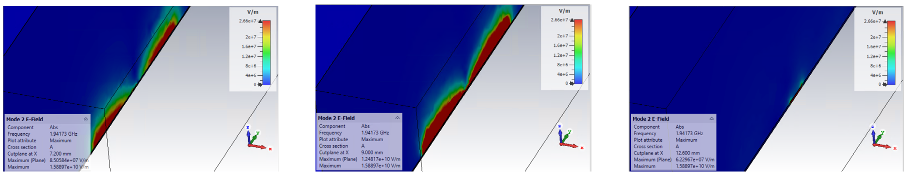

(d)

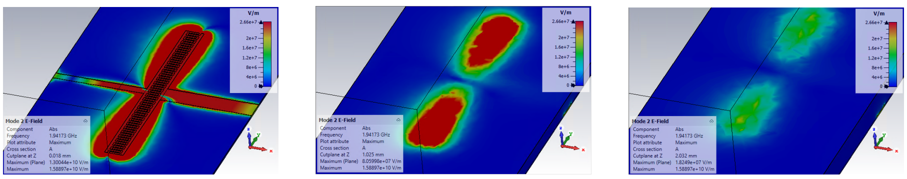

(e)

Figure 7.16: (a)(b)(c)Mode 2: electric field distribution for the unit cell at f_r. The high value of the electric field are non physical and due to the eigenmode solver, in which losses are ignored. (d) Electric field surrounding the unit cell at different cutting planes at $x = 6.2$ mm, $x = 9$ mm (UC centre) and $x = 15$ mm. (e) Electric field surrounding the unit cell at different cutting planes at $x = 18\,\mu$m, $x = 1$ mm and $x = 2.5$ mm.

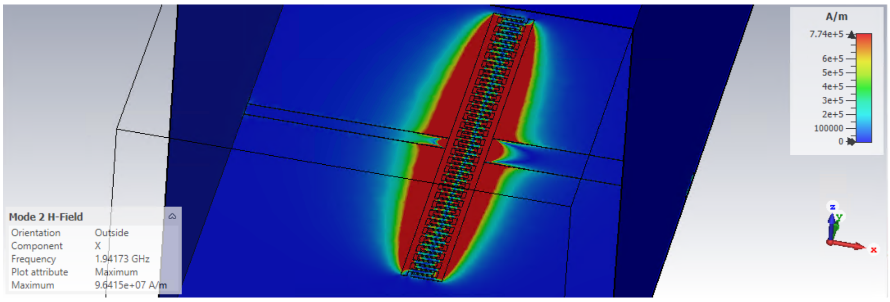

(a) $H_x(x, y, z)$

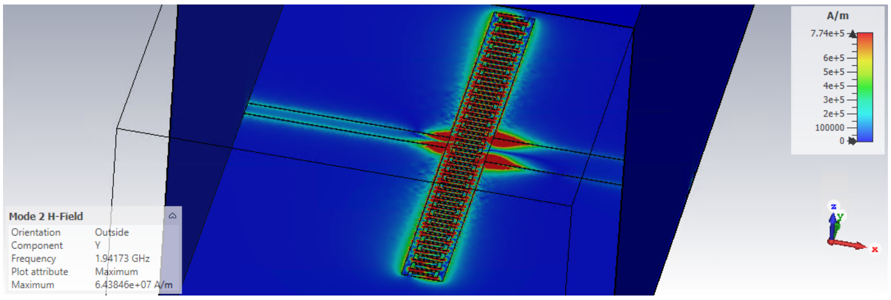

(b) $H_y(x, y, z)$

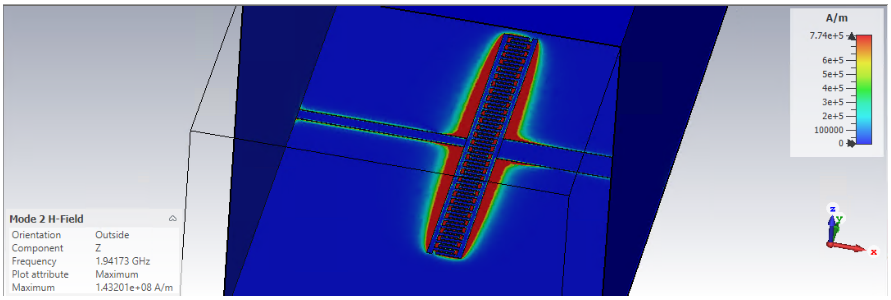

(c) $H_z(x, y, z)$

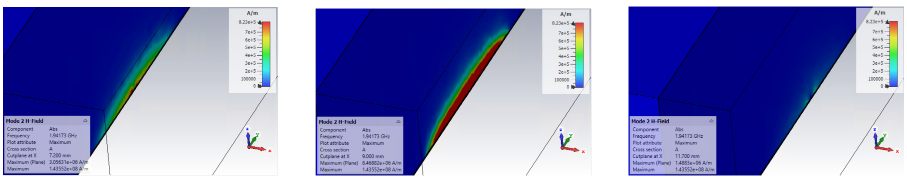

(d)

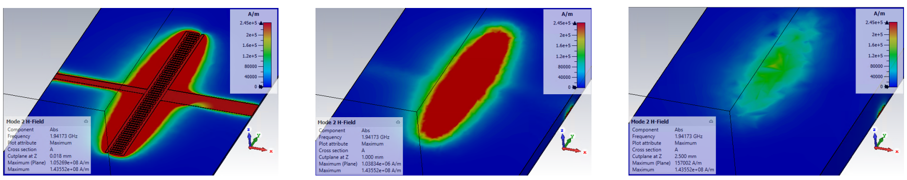

(e)

Figure 7.17: (a)(b)(c) Mode 2: magnetic field distribution for the unit cell at f_r. The high value of the electric field are non physical and due to the eigenmode solver, in which losses are ignored.(d) Magnetic field surrounding the unit cell at different cutting planes at $x = 6.2\,\text{mm}$, $x = 9\,\text{mm}$ (UC centre) and $x = 15\,\text{mm}$. (e) Magnetic field surrounding the unit cell at different cutting planes at $x = 18\,\mu\text{m}$, $x = 1\,\text{mm}$ and $x = 2.5\,\text{mm}$.

7.2.5 Oscillation and Radiation Analysis

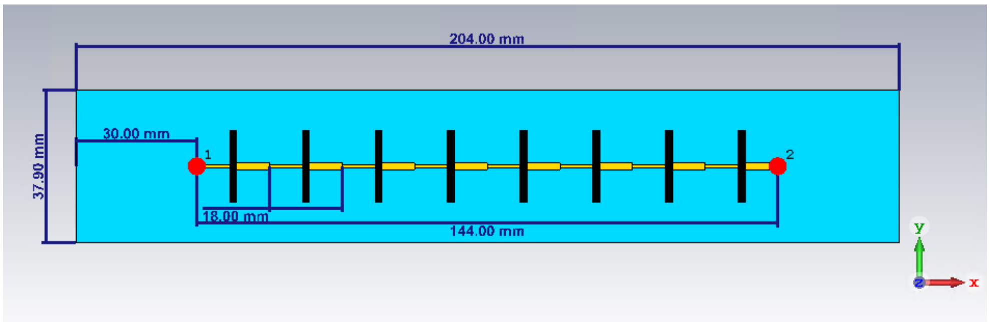

Figure 7.18: 8 cell array used as resonant-radiating device. Port 1 is used to feed the structure, whereas port 2 is used as load. Port 1 is used to feed the structure, whereas port 2 is used as load.

In the previous sections it has been shown how oscillation can be achieved in this design, but can radiation be obtained as well with such a structure? Can eventually the array also work as an antenna? We recall that the need of having a high quality factor is in contrast to the presence of losses in the system. Moreover, since the device is oscillating close to band edge, radiation (broadside in this case), becomes intrinsically impracticable with a *standard* periodic structure[4].

An 8 cells array is built and simulated by means of CST FD solver, employing discrete face ports. This solver has proved to give results further than the TD solver, anyway in this case simulation are faster with respect TD one. Moreover, the mesh can be more easily customized and adapted to the small geometry featured by the structure. Waveguide port exitation would bring to more accurate results, however this method does not allow to impose the port reference impedance arbitrarily. On the contrary, discrete face port does. The simulated structure in in figure 7.18, whereas the simulation setup can be consulted in appendix G.

Table 7.6: Main result from full wave simulation of the 8 cells ladder array.

Quantity	Symbol	Value CST	Value ADS
Expected resonance frequency	$f_{r,e}$	2.6145 GHz	2.534 GHz
Driving point conductance	G_{in}	1.575 µS	1.70 µS
Expected min. source conductance	$g_{s,e}$	−1.575 µS	−1.70 µS
Actual oscillation frequency	$f_{r,a}$	2.6145 GHz	2.535 GHz
Actual driving point conductance	$g_{s,a}$	−5.6 µS	−5.80 µS
Phase shift between cells	$\Delta\phi$	N.A.	−8.2 deg
Total Q-factor	Q_T	1188	422
Oscillation start-up time	t_{su}	25 ns	38 ns

4 As mentioned before, broadside radiation can be achieved with leaky wave employing right-left hand transmission line, or through some modification of the unit cell.

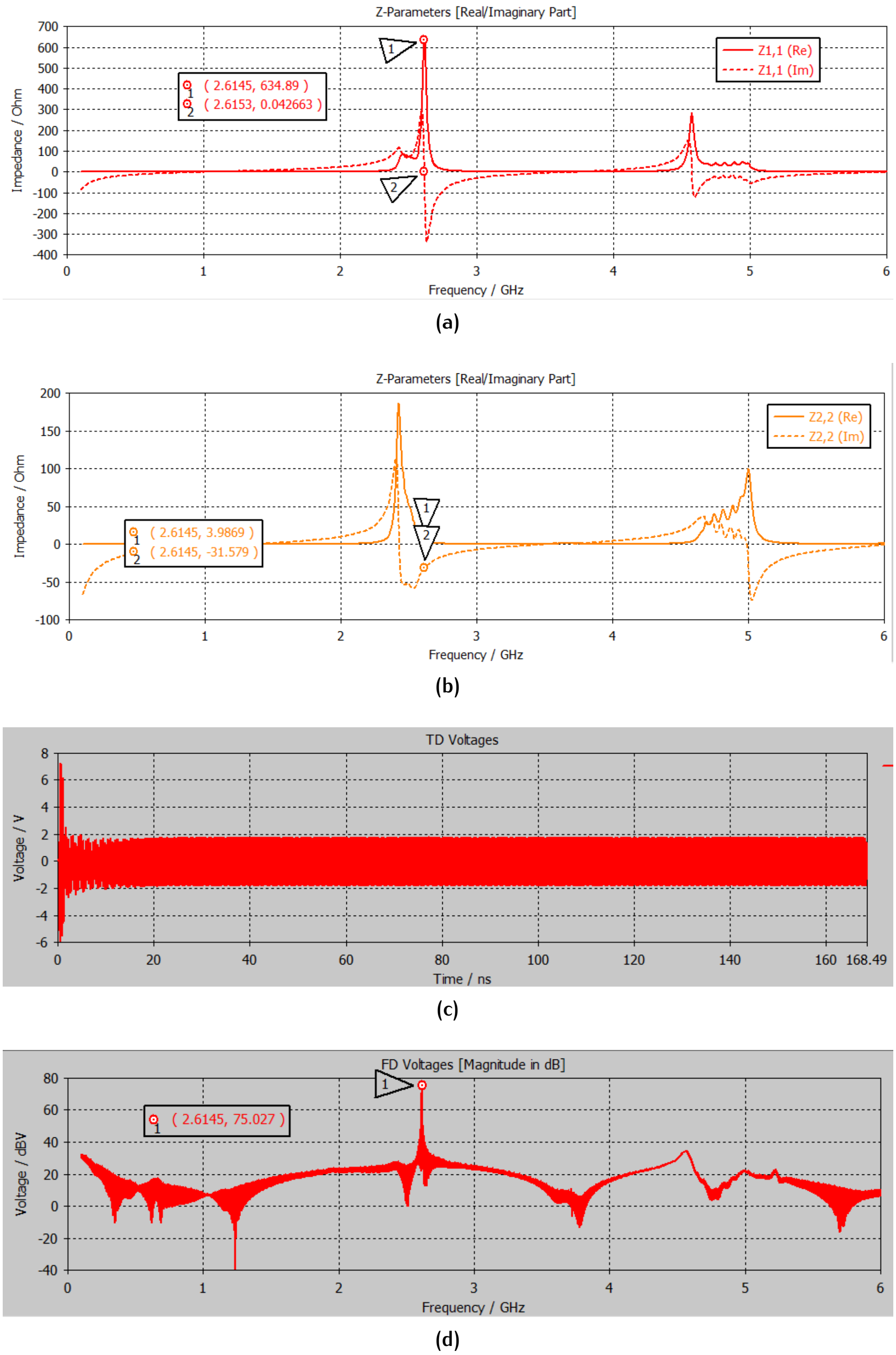

Figure 7.19: (a) Driving point impedance for the lossy designed array. (b) Output impendance for the designed array. (c) Voltage in time domain response at the input port. (d) Output spectrum: oscillation is located at $f_{r8} = 2.6145\,\text{GHz}$.

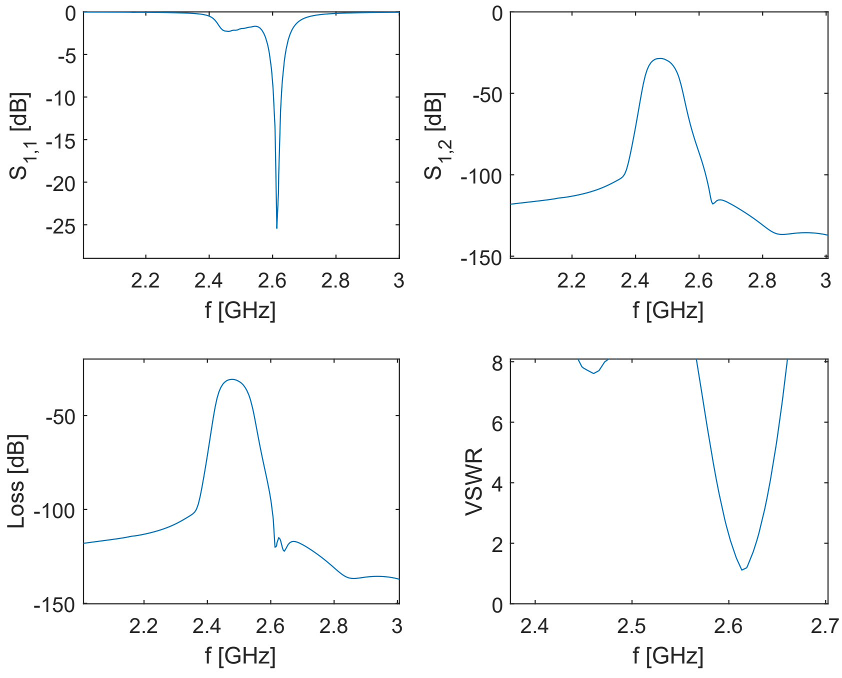

(a)

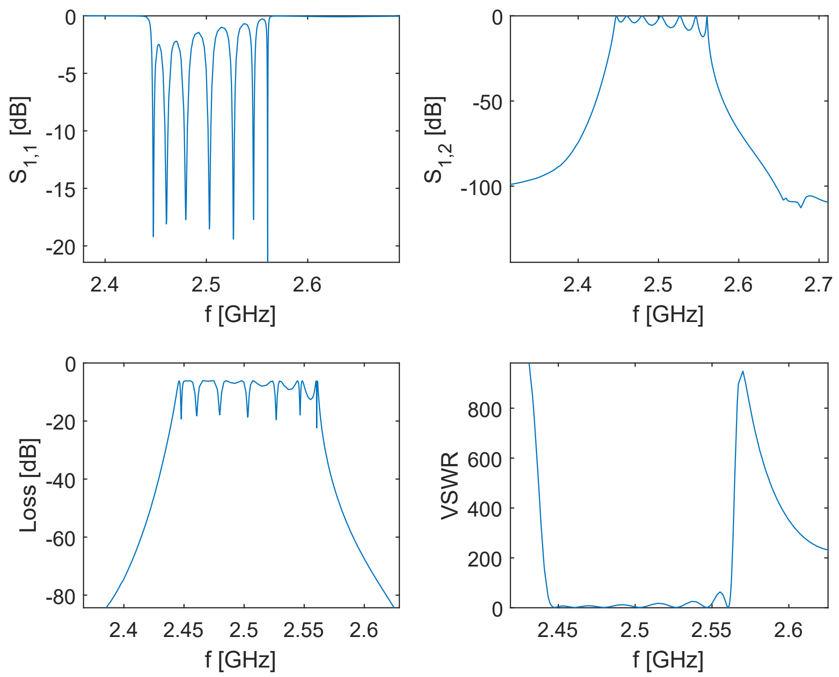

(b)

Figure 7.20: Scattering and loss parameters for (a) lossy and (b) lossless structure: reflection coefficient (top lef), transmission coefficient (top right), total loss (bottom left) and VSWR (bottom right).

The array is simulated and its scattering parameters are extracted. Each port of the device have resistive input matching at resonance frequency. In order to evaluate this frequency, the structure is simulated by means of CST Design Studio transient solver (circuital). To do so, the scattering parameters from the fullwave simulation are imported in the circuital simulator and then analysed with the circuit in figure G.1a. The complete circuit shows result in agreement to those presented in section 7.2.3. The comparison between the two methods is reported in table 7.6. Resonance frequency is similar for the two approaches, along with total Q-factor and driving point admittance.

Now that the oscillation has been verified to take place, it is possible to proceed by evaluating the radiation properties. First of all, array ports are matched to their input impedances at resonance frequency (driving point susceptance is null at port one and not considered at port 2). The set of scattering parameters related to this quantity are reported in figure 7.20 for both lossy and lossless structure. As it appears loss becomes really large around resonance frequency $f_r = 2.6145\,\text{GHz}$. It will be shown that such an important loss is the reason why this structure cannot be used as antenna with this substrate, since its radiation efficiency is very low. In fact, referring to figure 7.21, one can have some important information about radiation in farfield for this device. Although the field distribution on each unit cell is exponentially decaying, the radiation pattern is not the one typical of a leaky wave antenna. The radiation pattern is almost broadside, with one main beam laying on the $\varphi = 0$ plane.[5] Side lobes level is around $-2.4\,\text{dB}$ and HPBW is $36.7\,\text{dB}$ in the direction of major radiation. Figure 7.21a shows that the maximum antenna directivity is $D = 6.212\,\text{dB}$. However since radiation efficiency is $\eta_{cd} = \eta_0 = -36.71\,\text{dB}$, maximum gain is only $G = -30\,\text{dB}$. Even if input impedance matching is achieved, this gain reflects the presence of a large loss in conductor and dielectric at the operating frequency. Besides, being the radiating mode a quasi-standing wave and being the Q-factor of the array very high at f_r, only a small amount of the input power may be radiated. A comparison on figure 7.21f and 7.21g helps in understanding conduction losses are detrimental in determining the radiation efficiency. Close to oscillation frequency, lossless case shows overall low efficiency, anyway this is due to the frequency selectivity of the resonator and the vanishing group velocity approaching f_r. Some consideration could be done:

- The proposed layout is necessary to realise a frequency selective unit cell. However some improvement are necessary in the unit cell in order to increase the gain. For example by introducing ad additional two resonators shifted by $d/4$ in the same unit cell may improve broadside radiation [44].
- Beamwidth is proportional to antenna equivalent area. By increasing the number of cells, the area occupied by the device would increase eventually improving directivity.
- Fullwave simulator do not allow the use of non linear negative resistance component, therefore the actual behaviour of the device can not be tested. Adding a gain element would bring back the system to

5 Spherical coordinate system is used for simplicity.

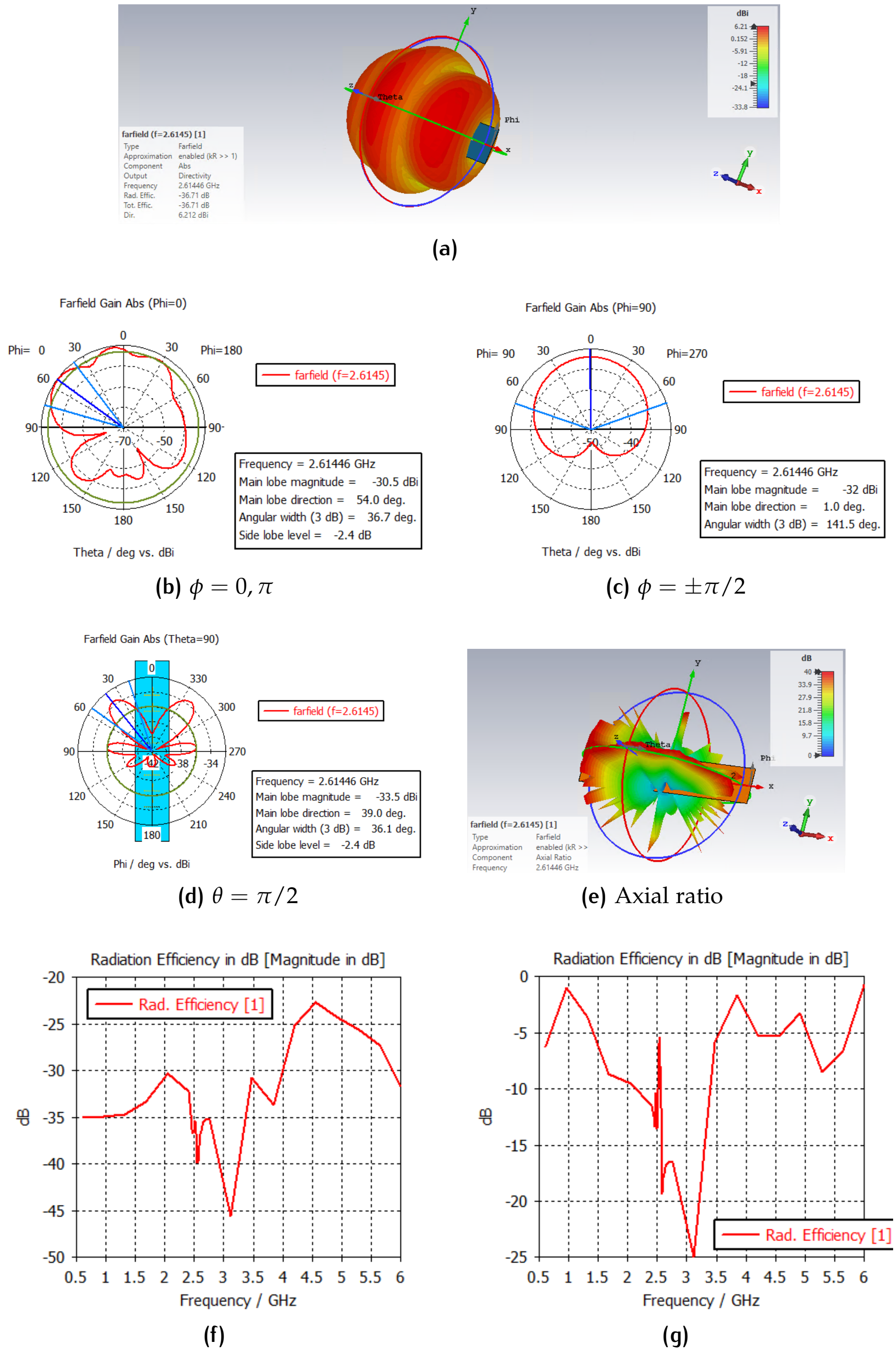

Figure 7.21: (a-d)Farfield radiation pattern and related cuts on the main planes for the lossy array. Radiation efficiency is very low because of the large amount ohmic and dielectric losses. (e) Axial ratio: the polarization is mainly elliptical in the main radiation direction. (f) Broadband radiation loss for lossy $N = 8$ array. (g)Broadband radiation loss for lossless $N = 8$ array.

work as a RBE structure, having the benefits of EPDs and increasing beamwidth [10].

- Low loss substrates may improve overall radiation efficiency.

- The device could be used as nearfield source, rather than farfield.

The farfield pattern shape, would not suggest the presence of a leaky wave travelling in the device. However, figure 7.22 confirms that actually a leaky travelling mode is present. In fact, the electric field is sampled on a cylindrical surface of radius $r = 20\,\mathrm{cm}$ around the device. A phase variation corresponds to shift in space of the electric field main beam and relative maxima. Hence, it appears that the field around the radiator is not static, with a peak value of $\simeq 0.7\,\mathrm{V/m}$ located along the normal to the antenna (z axis).

The conclusion is that a travelling wave is indeed present on the oscillator surface and it is responsible of radiation. This fact may be explained by recalling that the device resonates close, but not exactly at, $\beta d \simeq 0$. Given that, the forward and backward travelling mode would be not perfectly coalescing, setting a travelling wave in the circuit (perfect coalescence would bring to a standing wave).

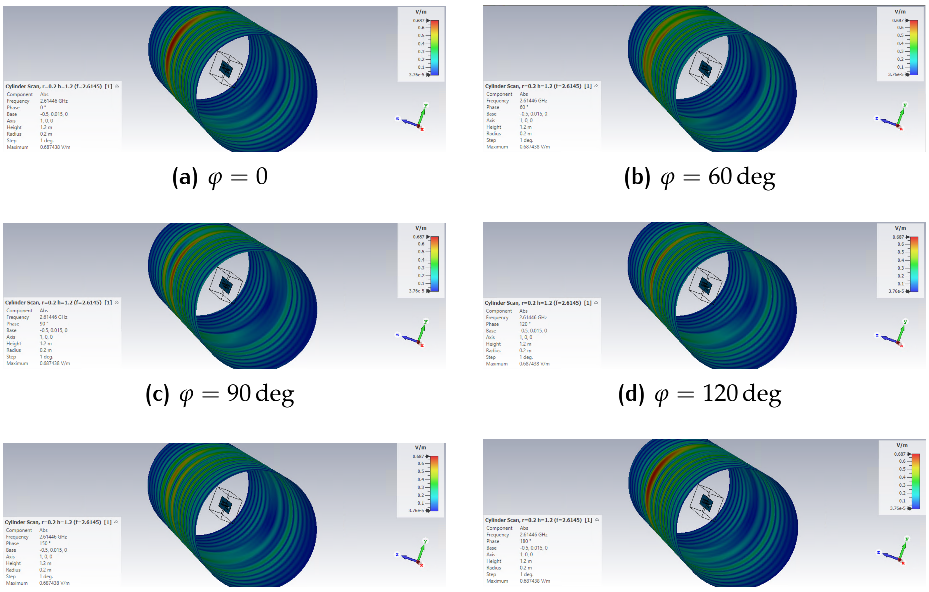

(a) $\varphi = 0$

(b) $\varphi = 60\,\mathrm{deg}$

(c) $\varphi = 90\,\mathrm{deg}$

(d) $\varphi = 120\,\mathrm{deg}$

(e) $\varphi = 150\,\mathrm{deg}$

(f) $\varphi = 180\,\mathrm{deg}$

Figure 7.22: Radiated field in the vicinity of the array at various phase steps showing the existance of a travelling wave. The cylindrical surface on which the electric field is evaluated is oriented along th x axis centered around the device. It has radius equal to $20\,\mathrm{cm}$ and height equal to $1\,\mathrm{m}$.

7.3 FOLDED LADDER DESIGN

The following analysis contains results from design tasks that are still under investigation. Here the aim is to obtain oscillation at the edge of the FBZ, hence at $\beta d = \pm\pi$. As it has been presented in the previous project, it is possible to obtain a stable oscillation employing a unit cell made of an interdigital capacitor and two microstrip access lines. Although the first aim is to obtain a sharp oscillation around RBE frequency, also radiation should be considered. In particular, being at band edge each node of the periodic structure is actually in opposition of phase with respect the other. The same can be say about each resonator. Radiation would be ideally impossible having each resonator-radiatior in opposition of phase with respect to the others. A ploy, aimed to solving this issue, would be a 90 deg. rotation of each cell on the plane (figure 7.23a).

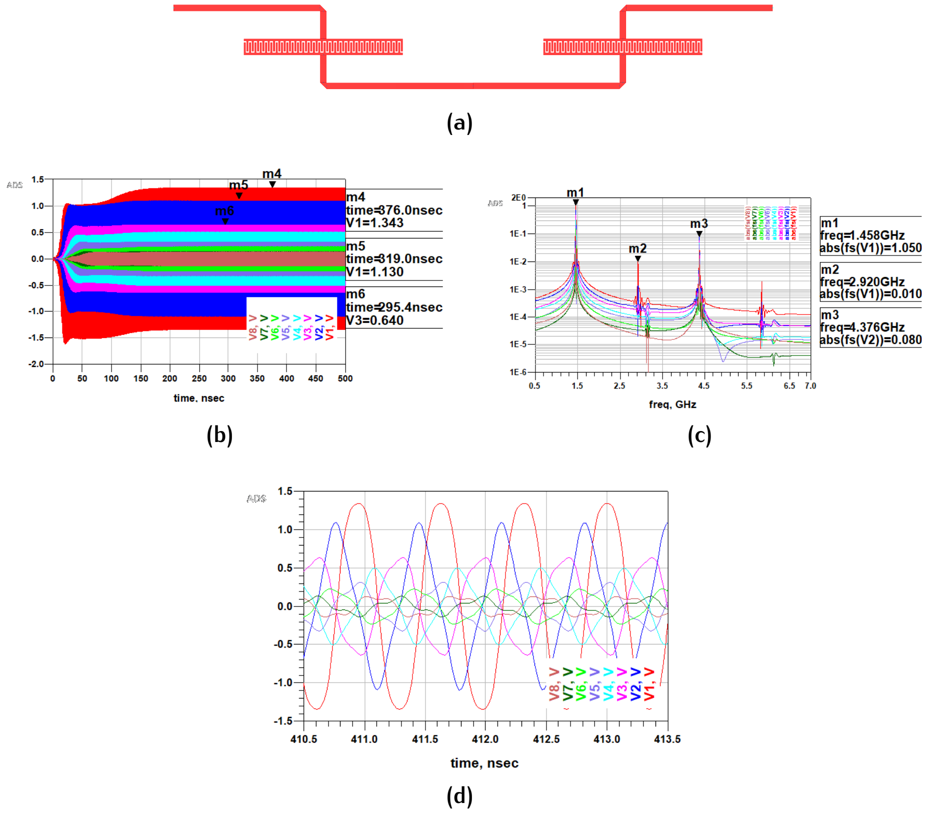

Figure 7.23: (a) Realised folded unit cell. (b) Voltage waveform of an 8 cell structure. (c) Output spectrum at each oscillator node. (d) Zoom on voltage waveforms.

As it appear the structure looks symmetric, but also asymmetric designs could be well suited for this application. This possibility is under investigation. At this time, the oscillation spectrum for this ladder structure is still quite impure. Compared to 7.11a the voltage waveforms undergo less attenuation along the line. This could be due to the fact the oscillator is working far from band edge, where losses are not too high. Since each node presents a different voltage waveform, not in phase to the other, the structure could still be able to radiate as a LWA. Improvements in oscillation properties is under investigation for this structure.

7.4 CLOSED LOOPS AND DISTRIBUTED GAIN

Previously we mentioned that gain would be able to better compensate for losses if provided in a distribute way. In particular, the structure presented until now are designed so that one only gain element is used at one of the oscillator sides. However, gain could be provided at each node through non linear elements. Discrete structures may still be used, provided that

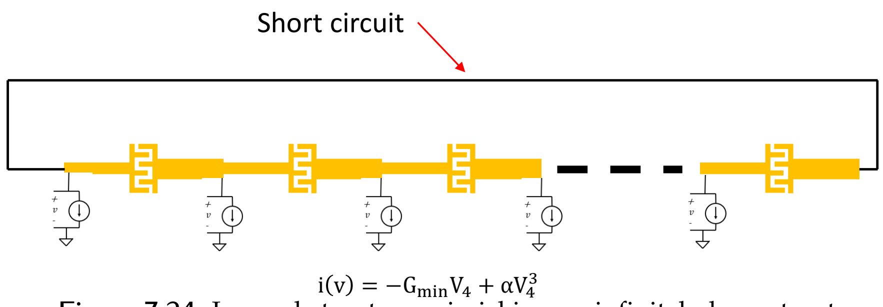

Figure 7.24: Looped structure mimicking an infinitely long structure.

each termination is the Bloch impedance Z_B seen at each side. Though Z_B is dispersive, hence a frequency dependent load should be used. Since this would be difficult in practice, another solution could be applied. In fact, each load could be substituted by means of a zero electrically long connection in order to realize a looped device. Oscillators based on this kind of structures are under investigation.

Part IV

CONCLUSIONS

8 CONCLUSIONS

This work have tried to find a solution to the following questions:

1. Is it possible to design any other EPD oscillating structures based on microstrip technology?
2. Is it an EPD condition sufficient oscillator also able to radiate, even if this is in contrast to having a large Q-factor?

An exact answer to both the questions would require a deeper study of the proposed structures and also the exploration of new solutions.

In this design, a novel topology for an RBE oscillator has been realised. An interdigital capacitor has been employed and designed to maximise its radiation resistance and minimize phase shits among radiating edges on its surface. After that, two access lines have been added to realise the unit cell. Asymmetric access lines turned out to be more convenient to obtain EPD at centre FBZ. The final layout area is approximatively $18\,\mathrm{mm} \times 18\,\mathrm{mm}$. Then, the unit cell is then simulated in full wave simulator and characterized to successfully verifying that an EPD could be retrieved by adding gain.

Next, a certain number of unit cell is cascaded to realize the actual resonator. The characterisation of the loaded quality factor suggests that using 8 cells loaded with a short circuit the structure behaves almost as an infinite periodic structure. After gain is added, provided by means of the equivalent model of a nonlinear cubic voltage controlled current source, it is then proved that the structure is an RBE oscillator. In fact, the figures of merit related to single ladder RBE oscillators are verified to be featured by the design (for instance $g_s = 1/N^{2.7}$). In particular the phase shift between each cell is 8 deg, meaning that the oscillator is actually working very close to $\beta d = 0$, i.e. the band edge (each cell in phase with the others). Moreover, resonance frequency $f_r = 2.535\,\mathrm{GHz}$ is slightly shifted from EPD frequency $f_e = 2.4561\,\mathrm{GHz}$. Besides, maximum loaded quality factor is $Q_{t,max} \approx 2000$ and minimum driving point impedance is $g_{e,min} = 5.8\,\mathrm{mS}$.

The next step it to perform eigenmode simulation by means of fullwave simulator to verify the T-matrix method validity and analysing field topology of the radiating mode. The radiating mode turns out to be the first $n = -1$ Floquet harmonic (see Chapter 5 for reference).

Full wave frequency domain simulations eventually suggest that the oscillator does not show particularly remarkable radiation properties. In fact even if the radiating mode is a leaky wave and the structure is working as leaky wave antenna (LWA), radiation efficiency is low due to large conduction and dielectric losses ($\eta_{nc} \simeq -15\,\mathrm{dB}$ for the lossless structure versus $\eta_{nc} \simeq -30\,\mathrm{dB}$ in lossy). This result suggests that the oscillator may be used as nearfield source rather than farfield ($|E_{pk}| \simeq 0.7\,\mathrm{V/m}$ at $0.5\,\mathrm{m}$ from the structure, with an excitation of $0.5\,\mathrm{W}$). Keep in mind that this result have been obtained without the addition of gain, because of simulation limitation.

The actual structure could therefore present significant enhancements. Further steps such as a prototype realization and topology improvements are under investigation.

Part V

APPENDIX

A PROOF OF KUROKAWA'S STABILITY CONDITION

Here the proof of Kurokawa stability criterion is given, as shown in [9]. Referring to figure [series oscillator], the load impedance is $Z_L(I,s) = R_L(I,s) + X_L(I,s)$, whereas the active device output impedance is $Z_S(I,s) = R_S(I,s) + X_S(I,s)$. Both the quantities can generally depend on the complex frequency $s = \alpha + j\omega$ and fundamental current component I. Given a small current change δI and a small change δs, one has:

$$\begin{aligned} Z_T(I,s) &= Z_S(I,s) + Z_L(I,s) \\ &= Z_T(I_0,s_0) + \left.\frac{\partial Z_T}{\partial s}\right|_{s_0,I_0} \delta s + \left.\frac{\partial Z_T}{\partial I}\right|_{s_0,I_0} \delta I = 0 \end{aligned} \tag{A.1}$$

where Z_T is null provided that the system is oscillating in $S_0 = j\omega_0$ with fundamental tone I_0. From A.1 it comes that:

$$\begin{aligned} Z_T(I_0,s_0) &= 0 \\ \frac{\partial Z_T}{\partial s} &= -j\frac{\partial Z_T}{\partial \omega} \end{aligned}$$

Therefore:

$$\delta s = \delta\alpha + j\delta\omega = \frac{-\partial Z_T/\partial I}{\partial Z_T/\partial s}\delta I = \frac{-j(\partial Z_T/\partial I)(\partial Z_T^*/\partial \omega)}{|\partial Z_T/\partial \omega|^2}\delta I \tag{A.2}$$

Supposing that every oscillation transient produced by δI or δs is decaying, we must have $\delta\alpha < 0$ if $\delta I > 0$. Therefore, from A.2:

$$Im\left\{\frac{\partial Z_T}{\partial I}\frac{\partial Z_T^*}{\partial \omega)}\right\} < 0 \tag{A.3}$$

or

$$\frac{\partial R_T}{\partial I}\frac{\partial X_T}{\partial \omega)} - \frac{\partial X_T}{\partial I}\frac{\partial R_T}{\partial \omega)} > 0 \tag{A.4}$$

Supposing that the load presents $\partial R_L/\partial I = \partial X_L/\partial I = \partial R_L/\partial \omega$ and substituting in A.4:

$$\frac{\partial R_S}{\partial I}\frac{\partial}{\partial \omega}(X_L + X_S) - \frac{\partial X_L}{\partial \omega}\frac{\partial R_S}{\partial I} > 0 \tag{A.5}$$

that is *Kurokawa's condition* for a stable oscillation.

B | ENERGY FLOW THROUGH A PERIODIC STRUCTURE

Given a periodic transmission line, its unit cell is considered and placed in a bounded surface S modelling a perfect electric conducting (PEC) waveguide walls (figure [unit cell with boundaries, collin]). The surface is chosen such that S_1 and S_2 boundaries coincide perpendicularly with the unit cell terminations. Moreover a cylindrical surface S_c, with infinite radius, surrounds the structure. The unit cell have dispersive parameters ϵ and μ.Since the volume is bounded by a perfect conductor the boundary condition for the electric field holds on the PEC:

$$\mathbf{n} \times \mathbf{E}|_S = 0 \tag{B.1}$$

From Foster's reactance theorem, [38] one has:

$$\begin{aligned}\oint_S \left(\mathbf{E} \times \frac{\partial \mathbf{H}^*}{\partial \omega} + \frac{\partial \mathbf{E}^*}{\partial \omega} \times \mathbf{H} \right) \cdot d\mathbf{S} &= -j \int_V \left(\mathbf{H} \cdot \mathbf{H}^* \frac{\partial \omega \mu}{\partial \omega} + \mathbf{E} \cdot \mathbf{E}^* \frac{\partial \omega \epsilon}{\partial \omega} \right) \\ &= -4j(W_m + W_e)\end{aligned} \tag{B.2}$$

Where $W_m + W_e$ is the total time-average energy stored in the volume bounded by S. Poynting vector is null on S_c and $\mathbf{dS} = \mathbf{z}dS$, where $\mathbf{z}$ is the unit versor along z.

$$\begin{aligned}\oint_{S_1} \left(\mathbf{E_1} \times \frac{\partial \mathbf{H_1^*}}{\partial \omega} + \frac{\partial \mathbf{E_1^*}}{\partial \omega} \times \mathbf{H_1} \right) \cdot \mathbf{z}\, dS - \oint_{S_2} \left(\mathbf{E_2} \times \frac{\partial \mathbf{H_2^*}}{\partial \omega} + \frac{\partial \mathbf{E_2^*}}{\partial \omega} \times \mathbf{H_2} \right) \cdot \mathbf{z}\, dS = \\ = -4j(W_m + W_e)\end{aligned} \tag{B.3}$$

Where $\mathbf{E_1}$,$\mathbf{H_1}$ and $\mathbf{E_2}$,$\mathbf{H_2}$ are the electric and magnetic fields on terminal 1 and 2, respectively. For Bloch modes:

$$\mathbf{E_2} = \mathbf{E_1} e^{-j\gamma d} \quad \mathbf{H_2} = \mathbf{H_1} e^{-j\gamma d} \tag{B.4}$$

where γd is the phase shift introduced by the unit cell of length d for the Bloch mode. Substituting in B.4, one has that the argument of the second interval becomes:

$$\begin{aligned}\mathbf{E_2} \times \frac{\partial \mathbf{H_2^*}}{\partial \omega} + \frac{\partial \mathbf{E_2^*}}{\partial \omega} \times \mathbf{H_2} = \\ \mathbf{E_1} \times \frac{\partial \mathbf{H_1^*}}{\partial \omega} + jd\frac{d\beta}{d\omega} \mathbf{E_1} \times \mathbf{H_1}^* + \frac{\partial \mathbf{E_1^*}}{\partial \omega} \times \mathbf{H_1} + jd\frac{d\beta}{d\omega} \mathbf{E_1}^* \times \mathbf{H_1}\end{aligned} \tag{B.5}$$

Therefore:

$$-2jd\frac{d\beta}{d\omega} Re\left\{ \oint_S \mathbf{E_1} \times \mathbf{H_1}^* \cdot \mathbf{z}\, dS \right\} = -4jd\frac{d\beta}{d\omega} P = -4j(W_m + W_e) \tag{B.6}$$

Where:

$$P = \frac{1}{2} Re\left\{ \oint_S \mathbf{E_1} \times \mathbf{H_1}^* \cdot \mathbf{z}\, dS \right\} \tag{B.7}$$

is the transmitted power from a terminal plane. Inverting B.6, one has:

$$v_g = \frac{d\omega}{d\beta} = d\frac{P}{W_m + W_e} \tag{B.8}$$

from which it comes that the group velocity v_g times the energy density $(W_m + W_e)/d$ give the power flowing through one unit cell terminal. Hence, v_g is the energy flow's velocity.

C | FARFIELD FIELDS DERIVATION

It is given a finite volume with main dimension D, that contains magnetic source ($\mathbf{J}_m$) or electric sources ($\mathbf{J}_e$). Each point of the volume is reached by means a vector $\boldsymbol{r}'$. A generic point outside the volume is located at position P at a distance $\boldsymbol{r}$ from the sources. The solution of the wave equation exited by an electric or magnetic current densities, at this position P is given by the convolution integral:

$$\mathbf{E}(\mathbf{r}) = -j\omega\mu_0 \int_{\mathbf{r}'} \underline{\mathbf{G}}(\boldsymbol{r}-\boldsymbol{r}') \cdot \mathbf{J}_e(\boldsymbol{r}') \cdot d\boldsymbol{r}' + j\int_{\mathbf{r}'} \boldsymbol{\nabla} \times \underline{\mathbf{G}}(\boldsymbol{r}-\boldsymbol{r}') \cdot \mathbf{J}_m(\boldsymbol{r}') \cdot d\boldsymbol{r}' \tag{C.1}$$

where $\mathbf{G}$ is the dyadic Green function, that for $\boldsymbol{rho}k_0 \gg 1$ is given by:

$$\underline{\mathbf{G}}(\boldsymbol{r}-\boldsymbol{r}') \simeq \frac{e^{-jk_0\rho}}{4\pi\rho}\underline{\mathbf{I}}_{t,\rho} \tag{C.2}$$

$$\boldsymbol{\nabla} \times \underline{\mathbf{G}}(\boldsymbol{r}-\boldsymbol{r}') = -jk_0\hat{\boldsymbol{\rho}} \times \underline{\mathbf{G}}(\boldsymbol{r}-\boldsymbol{r}') \simeq -jk_0\frac{e^{-jk_0\rho}}{4\pi\rho}\hat{\boldsymbol{\rho}} \times \underline{\mathbf{I}}_{t,\rho} \tag{C.3}$$

where $\frac{e^{-jk_0\rho}}{4\pi\rho}$ is the scalar Green's function and $\underline{\mathbf{I}}_{t,\rho}$ is the dyadic transverse identity defined by $\underline{\mathbf{I}}_{t,\rho} = (\hat{\boldsymbol{\varphi}}\hat{\boldsymbol{\theta}} - \hat{\boldsymbol{\theta}}\hat{\boldsymbol{\varphi}})$, with $\hat{\varphi}$ and $\hat{\boldsymbol{\theta}}$ unit vector for the azimuth and zenith angles, respectively. The transverse dyadic for very large $\boldsymbol{\rho}$ is almost constant and can be carried out of the integral. Since $\boldsymbol{\rho} = \boldsymbol{r} - \boldsymbol{r}'$, the amplitude ρ is given by:

$$\begin{aligned}\rho &= \sqrt{(\boldsymbol{r}-\boldsymbol{r}')(\boldsymbol{r}-\boldsymbol{r}')} = \sqrt{r^2 + r'^2 - 2\boldsymbol{r}\cdot\boldsymbol{r}'} \\ &= r\sqrt{1 + \left(\frac{r'}{r}\right)^2 - 2\hat{\boldsymbol{r}}\cdot\frac{r'}{r}}\end{aligned} \tag{C.4}$$

that, in case that $r' \ll r$ can be approximated at the first order as:

$$\rho \simeq r - \boldsymbol{r}' \cdot \hat{\boldsymbol{r}} \tag{C.5}$$

that is called *Fraunhofer approsimation*. In this condition, called *farfield condition* each vector $\boldsymbol{\rho}$ is considered almost parallel to each other. The phase different introduced by this approximation can be estimated as an error given by:

$$\Delta\varphi = k_0\Delta\rho = \frac{k_0}{2r}\left[r'^2 - (\boldsymbol{r}'\cdot\hat{\boldsymbol{r}})^2\right] < \frac{k_0 r'^2}{2r} \tag{C.6}$$

Each points inside the volume is in a position bounded by $r' < D/2$, therefore:

$$\frac{4D^2}{4r\lambda} \tag{C.7}$$

and considered $\Delta\varphi < \pi/8$ an acceptable error one has the Frounhofer approximation defined as:

$$r > \frac{2D^2}{\lambda} = r_{ff} \tag{C.8}$$

Substituting the relations obtained till now in C.2, and recalling that $\boldsymbol{\rho} \approx \boldsymbol{r}$, one has:

$$\underline{\mathbf{G}} = \frac{e^{-jk_0 r}}{4\pi r}(\hat{\boldsymbol{\theta}}\hat{\boldsymbol{\theta}} + \hat{\boldsymbol{\varphi}}\hat{\boldsymbol{\varphi}})e^{jk_0(\boldsymbol{r}'\cdot\hat{\boldsymbol{r}})} \tag{C.9}$$

$$\boldsymbol{\nabla} \times \underline{\mathbf{G}} = -jk_0\frac{e^{-jk_0 r}}{4\pi r}(\hat{\boldsymbol{\varphi}}\hat{\boldsymbol{\theta}} - \hat{\boldsymbol{\theta}}\hat{\boldsymbol{\varphi}})e^{jk_0(\boldsymbol{r}'\cdot\hat{\boldsymbol{r}})} \tag{C.10}$$

which, substituted in C.1 yields:

$$\begin{aligned}\mathbf{E}(\boldsymbol{r}) = -j\omega\mu_0\frac{e^{-jk_0 r}}{4\pi r}\Bigg[&\underline{\mathbf{I}}_{t,r}\cdot\int_{\boldsymbol{r}'}\mathbf{J}_e(\boldsymbol{r}')e^{jk_0(\boldsymbol{r}'\cdot\boldsymbol{r})}\,d\boldsymbol{r}'\\ &- Y_0\hat{\boldsymbol{r}}\times\underline{\mathbf{I}}_{t,r}\cdot\int_{\boldsymbol{r}'}\mathbf{J}_m(\boldsymbol{r}')e^{jk_0(\boldsymbol{r}'\cdot\boldsymbol{r})}\,d\boldsymbol{r}'\Bigg]\end{aligned} \tag{C.11}$$

where the quantity closed in square brackets is the *generalised electric moment*, GEM, indicated with $\boldsymbol{p}_e(\hat{\boldsymbol{r}})$, such that:

$$\boldsymbol{p}_e(\hat{\boldsymbol{r}}) = \underline{\mathbf{I}}_{t,r}\cdot\int_{\boldsymbol{r}'}\mathbf{J}_e(\boldsymbol{r}')e^{jk_0(\boldsymbol{r}'\cdot\boldsymbol{r})}\,d\boldsymbol{r}' - Y_0\hat{\boldsymbol{r}}\times\underline{\mathbf{I}}_{t,r}\cdot\int_{\boldsymbol{r}'}\mathbf{J}_m(\boldsymbol{r}')e^{jk_0(\boldsymbol{r}'\cdot\boldsymbol{r})}\,d\boldsymbol{r}' \tag{C.12}$$

Each integral in C.12 is a three dimensional Fourier transform computed for $\boldsymbol{k} = k_0\hat{\boldsymbol{r}}$. The relation hence becomes:

$$\boldsymbol{p}_e(\hat{\boldsymbol{r}}) = \underline{\mathbf{I}}_{t,r}\cdot\mathcal{F}_3\{\mathbf{J}_e(\boldsymbol{r})\}_{k_0\hat{\boldsymbol{r}}} - Y_0\hat{\boldsymbol{r}}\times\underline{\mathbf{I}}_{t,r}\cdot\mathcal{F}_3\{\mathbf{J}_e(\boldsymbol{r})\}_{k_0\hat{\boldsymbol{r}}} \tag{C.13}$$

Notice that the GEM is a vector that has only transverse components along θ and φ. The polarization of the resulting electric field can be derived by separating variables as follows:

$$\boldsymbol{p}_e(\hat{\boldsymbol{r}}) = \boldsymbol{p}_{e_\theta}(\hat{\boldsymbol{r}})\hat{\boldsymbol{\theta}} + \boldsymbol{p}_{e_\varphi}(\hat{\boldsymbol{r}})\hat{\boldsymbol{\varphi}} \tag{C.14}$$

To sum up, the electric field can be written in term of $\boldsymbol{p}_e(\hat{\boldsymbol{r}})$ as:

$$\mathbf{E}(\boldsymbol{r},\theta,\varphi) = -jZ_0\frac{e^{-jk_0 r}}{2r\lambda}\boldsymbol{p}_e(\hat{\boldsymbol{r}}) \tag{C.15}$$

whereas the magnetic field can be eventually found by means of the well known conversion formula:

$$\mathbf{H}(\boldsymbol{r},\theta,\varphi) = \frac{1}{Z_0}\boldsymbol{k}\times\mathbf{E}(\boldsymbol{r},\theta,\varphi) \tag{C.16}$$

For what concerns the equivalent electric and magnetic current, they can be calculated by means of equivalence theorem.[42] Given an arbitrary field distribution (electric, $\mathbf{E}_s$ or magnetic, $\mathbf{H}_s$) located on the aperture (extension) of a radiator, the equivalent sources are given by:

$$\mathbf{J}_m = -2\hat{\boldsymbol{n}}\times\mathbf{E}_s \tag{C.17}$$

$$\mathbf{J}_e = -2\hat{\boldsymbol{n}}\times\mathbf{H}_s \tag{C.18}$$

where $\hat{\boldsymbol{n}}$ is the unit vector normal to the aperture.

D TRANSMISSION LINE CIRCUIT MODEL

Telegraphers equation solution yields that voltage and current in a transmission line are given by the superposition of two travelling waves expresses ad time-harmonic functions: one forward mode with wavenumber $-\gamma$ and one backward mode with wavenumber γ. The wavenumber is expressed as $\gamma = \beta + j\alpha$. The expression for Voltage and current along the line is given by:

$$V(z) = V^{+}e^{-j\gamma z} + V^{-}e^{-j\gamma z} \tag{D.1}$$

$$I(z) = I^{+}e^{-j\gamma z} - I^{-}e^{-j\gamma z} \tag{D.2}$$

Relations above can be written in term of transmission matrix. In particular, for a lossless transmission line we have the T-matrix defined as follows:

$$\underline{\mathbf{T}}^{tl} = \begin{pmatrix} A^{tl} & B^{tl} \\ C^{tl} & D^{tl} \end{pmatrix} = \begin{pmatrix} \cos\gamma l & -jZ_0\sin\gamma l \\ -j\dfrac{\sin\gamma l}{Z_0} & \cos\gamma l \end{pmatrix} \tag{D.3}$$

Moreover,the conversion from T matrix to Z matrix yields:

$$\underline{\mathbf{Z}}_T^{tl} = \begin{pmatrix} Z_{11}^{tl} & Z_{12}^{tl} \\ Z_{21}^{tl} & Z_{22}^{tl} \end{pmatrix} = \begin{pmatrix} \dfrac{A^{tl}}{C^{tl}} & \dfrac{\Delta T^{tl}}{C^{tl}} \\ \dfrac{1}{C^{tl}} & \dfrac{A^{tl}}{C^{tl}} \end{pmatrix} \tag{D.4}$$

$$= Z_0 \begin{pmatrix} \dfrac{1}{j\tan\gamma l} & -\dfrac{1}{j\sin\gamma l} \\ -\dfrac{1}{j\sin\gamma l} & \dfrac{1}{j\tan\gamma l} \end{pmatrix} \tag{D.5}$$

where $\Delta\underline{\mathbf{T}} = 1$ since the network is reciprocal. The corresponding T-equivalent network follows:

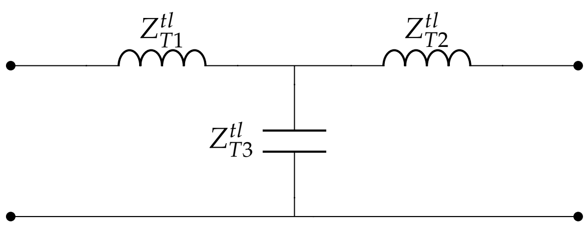

Figure D.1: Transmission line T-circuit equivalent.

Where:

$$Z_{T1}^{tl} = Z_{11}^{tl} - Z_{12}^{tl} = jZ_0\tan\frac{\gamma l}{2} \tag{D.6a}$$

$$Z_{T2}^{tl} = Z_{22}^{tl} - Z_{12}^{tl} = jZ_0\tan\frac{\gamma l}{2} \tag{D.6b}$$

$$Z_{T3}^{tl} = Z_{12}^{tl} = Z_{21}^{tl} = -j\frac{Z_0}{\sin\gamma l} \tag{D.6c}$$

Then Z^{tl}_{T1} and Z^{tl}_{T2} are series inductive components, represented by L^{tl}, whereas the Z^{tl}_{T3} models a shunt capacitance C^{tl} in figure D.1.

E RBE OSCILLATOR AT $\beta d = 0$, SIMULATION SETUP

SYMMETRICAL UC: ADS MOM MW SOLVER SETUP

In the following the screenshots reporting the configuration of ADS in Momentum Microwave simulation. The total amount of meshcells is 17150.

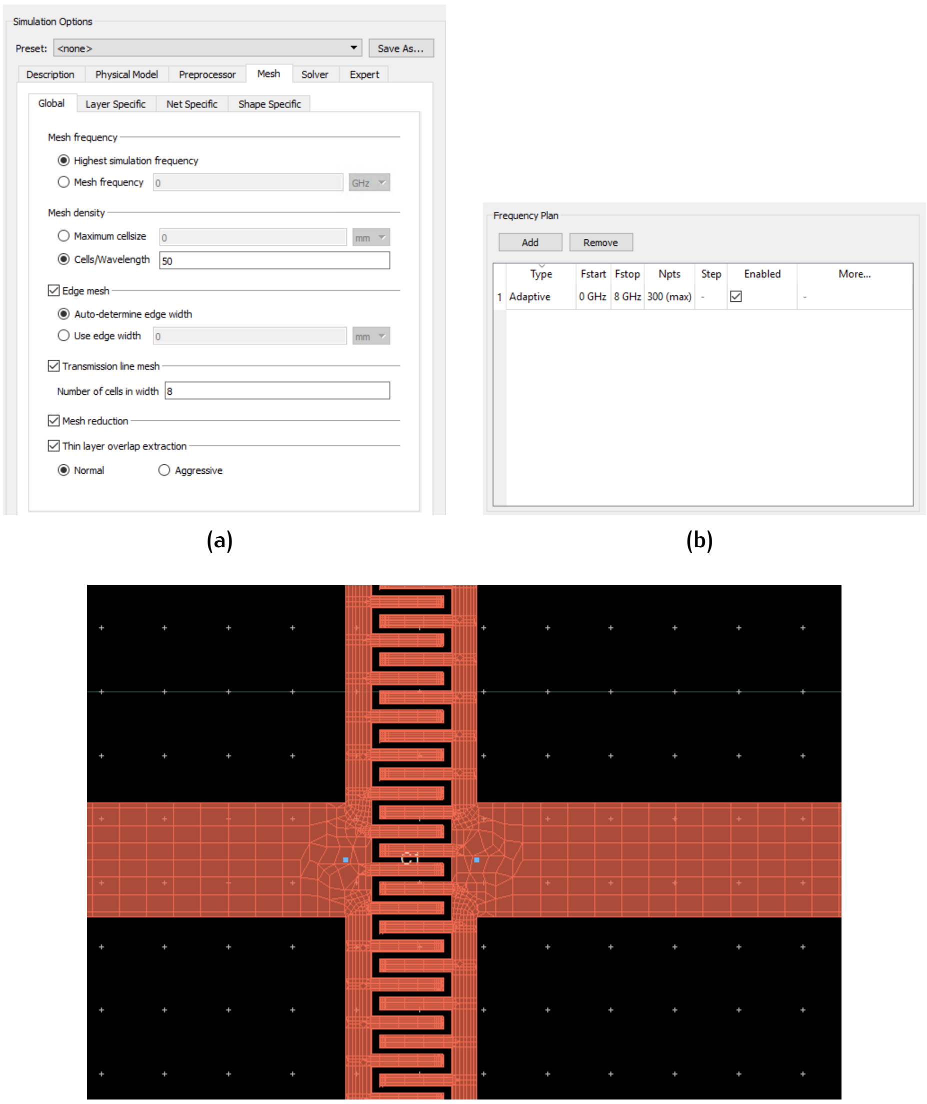

(c)

Figure E.1: (a)(b)Simulation configuration for ADS MOM MW solver. (c) Mesh used for the simulation.

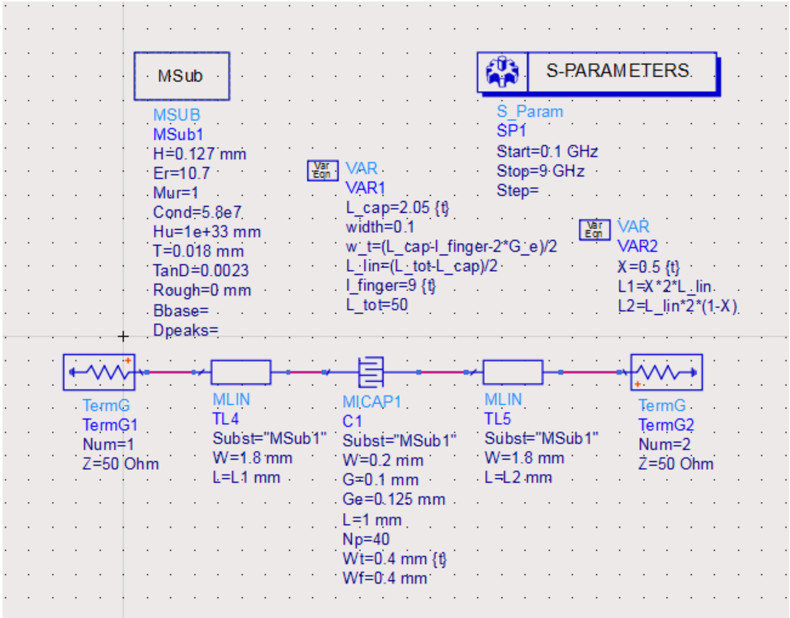

Figure E.2: Circuit used for the layout extraction and lossless simulation.

ASYMMETRICAL UC: ADS MOM MW SOLVER SETUP

In the following the screenshots reporting the configuration of ADS in Momentum Microwave simulation. The total amount of meshcells is 22500.

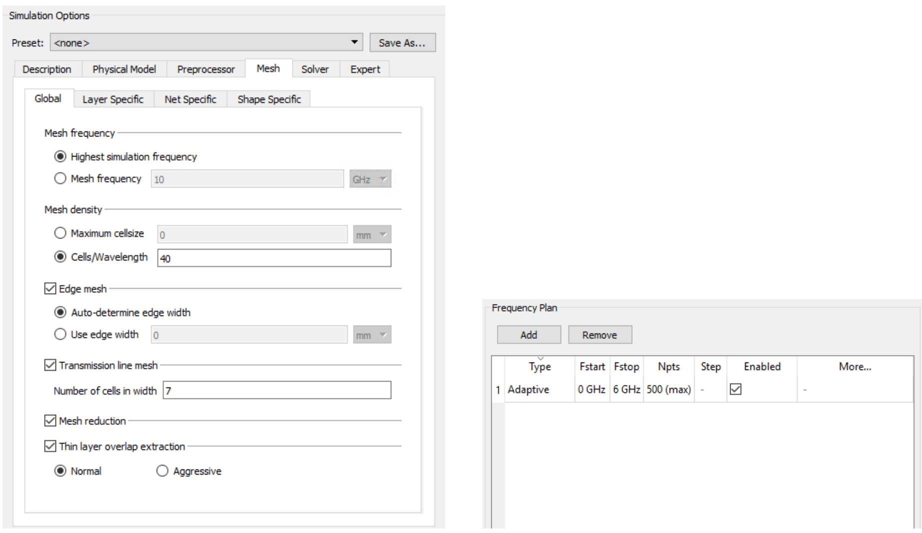

(a) (b)

Figure E.3: (a)(b)Simulation configuration for ADS MOM MW solver.

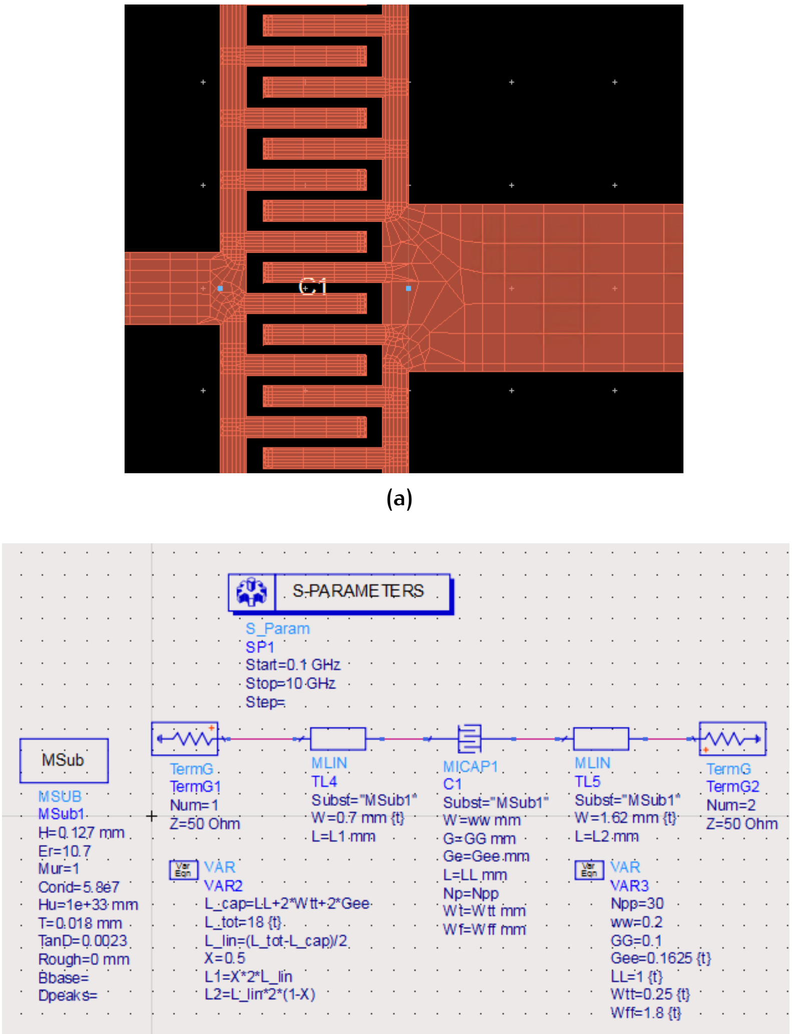

(a)

(b)

Figure E.4: (a) Mesh used for the simulation. (b) Circuit used for the layout extraction and lossless simulation.

ASYMMETRICAL UC: CST MW STUDIO EIGENMODE SOLVER SETUP

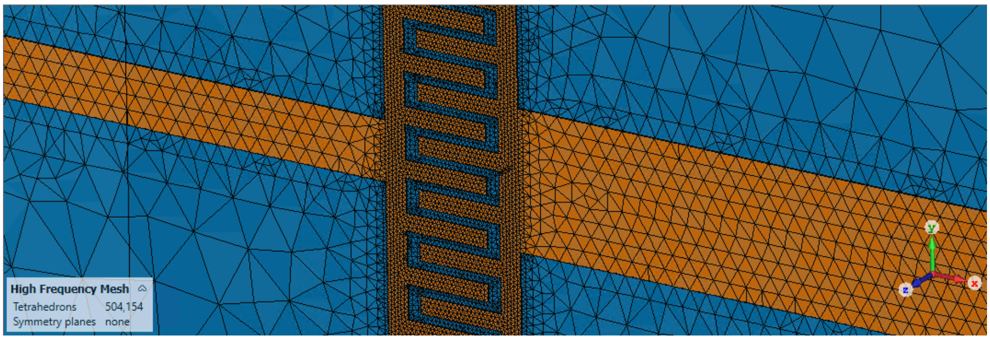

(a)

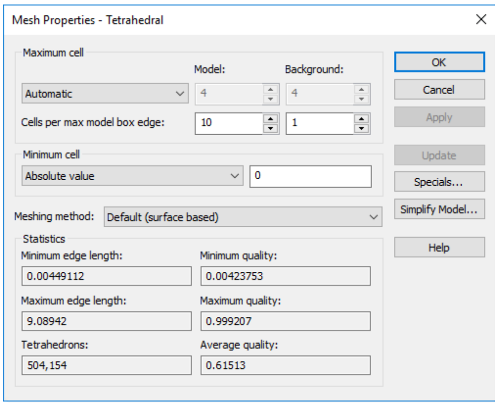

(b)

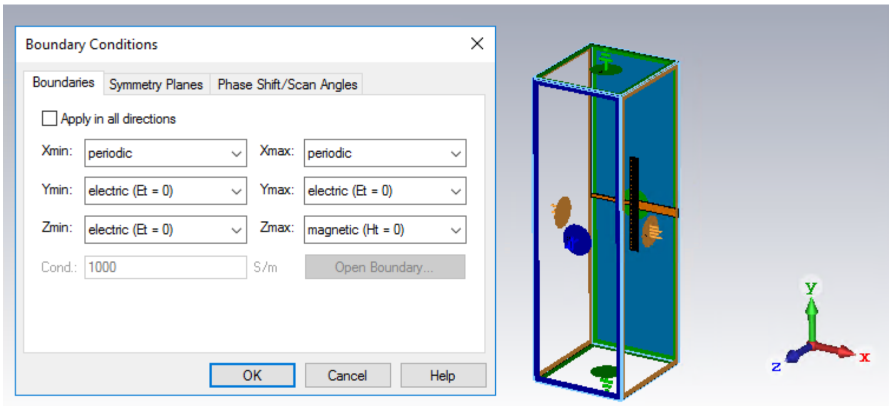

(c)

Figure E.5: (a) Mesh used for the eigenmode simulation. (b) Mesh setup. Notice, a denser meshgroup has been used in narrow parts. (c) Boundary conditions employed for the simulation.

ASYMMETRICAL UC: CST MW STUDIO FD DISCRETE PORT

Solver accuracy parameters is set to 0.02. Total number of meshcells: ≈500k. Frequency range is $f = [0.1\,\text{GHz}, 6\,\text{GHz}]$. Open boundaries condition is imposed.

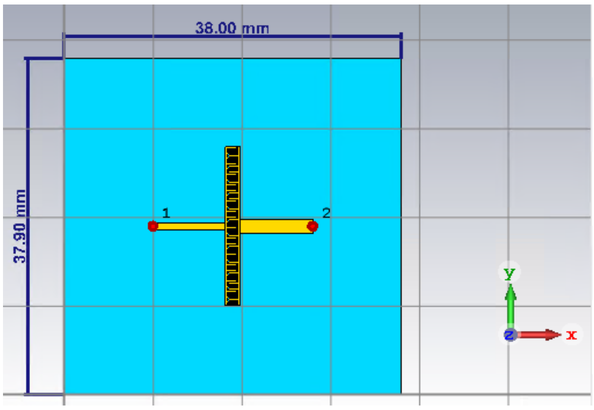

(a)

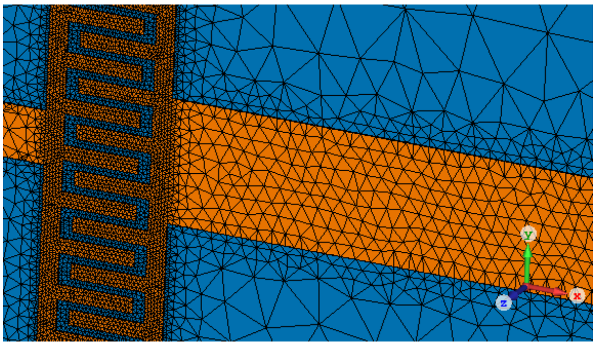

(b)

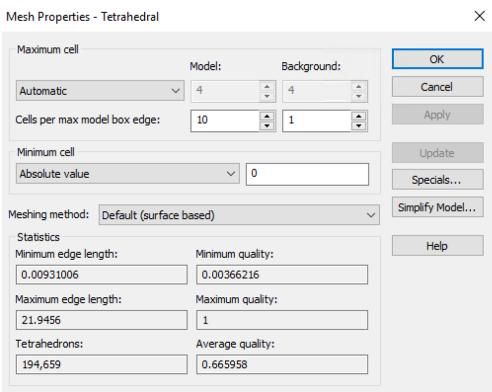

(c)

Figure E.6: (a) Simulation layout (valid also for TD simulator). (b) Mesh used for the frequency domain simulation. (c) Mesh setup. Notice, a denser mesh-group has been used in narrow parts.

ASYMMETRICAL UC: CST MW STUDIO TD DISCRETE PORT

Solver accuracy parameters is set to $-80\,\text{dB}$. Total number of meshcells: ≈2.5M. Frequency range is $f = [0.1\,\text{GHz}, 6\,\text{GHz}]$. Open boundaries condition is imposed.

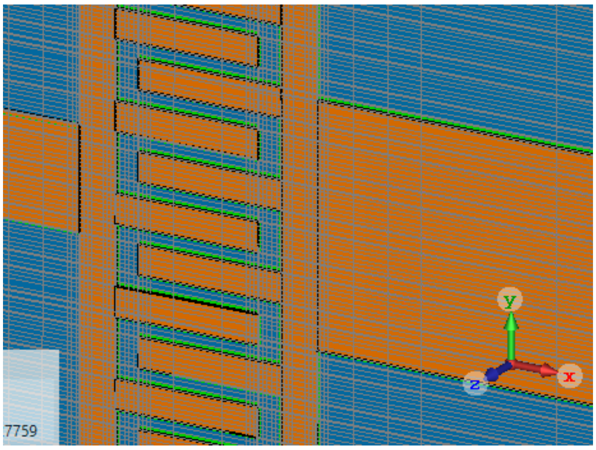

(a)

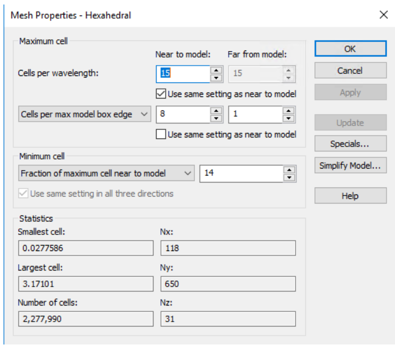

(b)

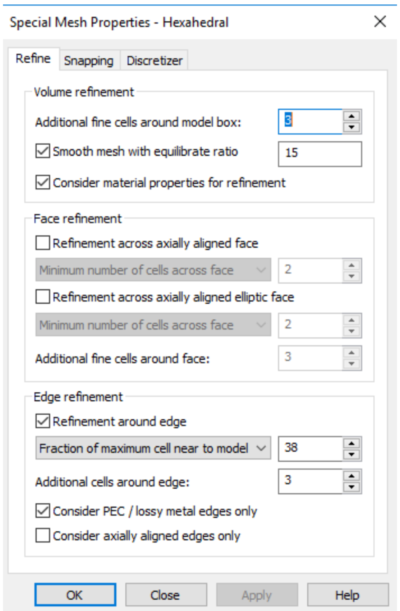

(c)

Figure E.7: (a) Mesh used for the time domain simulation. (b),(c) Mesh setup. Notice, a denser meshgroup has been used in narrow parts.

ASYMMETRICAL UC: CST MW STUDIO FD WAVEGUIDE PORT

Solver accuracy parameters is set to 0.02. Total number of meshcells: ≈600k. Frequency range is $f = [0.1\,\text{GHz}, 6\,\text{GHz}]$. Open boundaries condition is imposed. Waveguide port are single mode with extension coefficient $k = 7$.

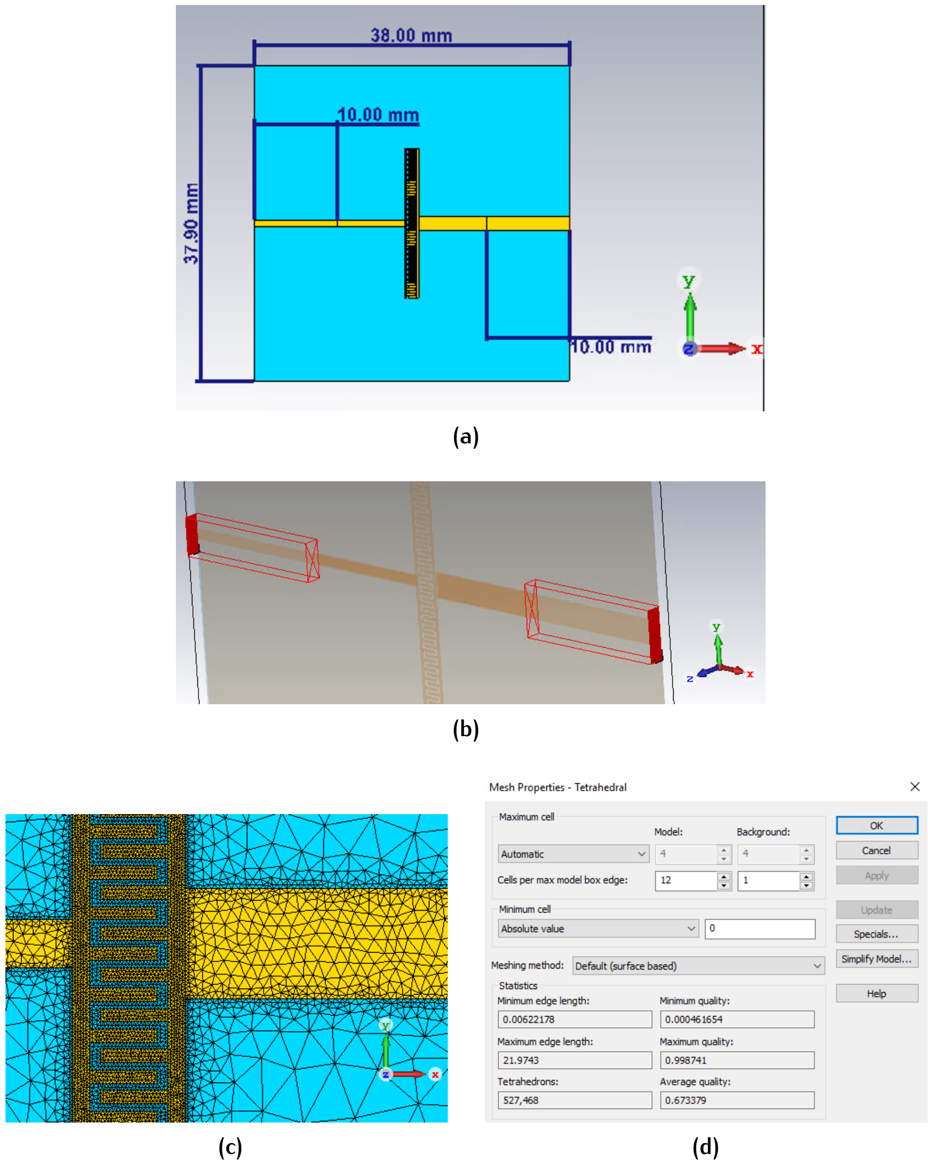

Figure E.8: (a) Simulation layout (valid also for TD simulator). (b) Waveguide ports de-embedding. (c) Mesh used for the frequency domain simulation. (d) Mesh setup. Notice, a denser meshgroup has been used in narrow parts.

ASYMMETRICAL UC: CST MW STUDIO TD WAVEGUIDE PORT

Solver accuracy parameters is set to $-80\,\mathrm{dB}$. Total number of meshcells: $\approx$2.5M. Frequency range is $f = [0.1\,\mathrm{GHz}, 6\,\mathrm{GHz}]$. Open boundaries condition is imposed. Waveguide port are single mode with extension coefficient $k = 7$.

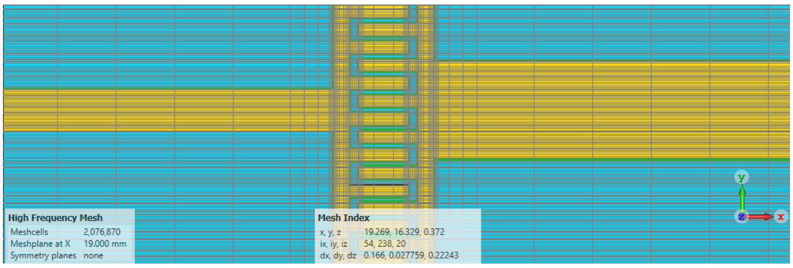

(a)

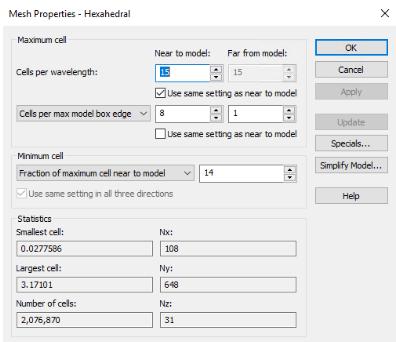

(b)

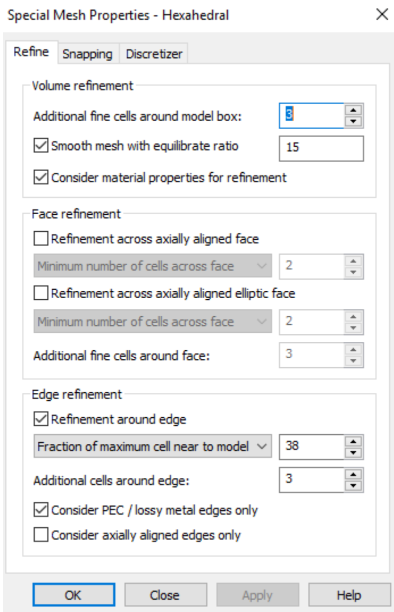

(c)

Figure E.9: (a) Simulation layout (valid also for TD simulator). (b) Waveguide ports de-embedding. (c) Mesh used for the frequency domain simulation. (d) Mesh setup. Notice, a denser meshgroup has been used in narrow parts.

F EIGENMODE SOLVER MODES FIELD CUTS

In the following various cuts of the asymmetrical unit cell are reported, in order to inspect the internal electric field behaviour for the eigenmode 2 (7.14c).

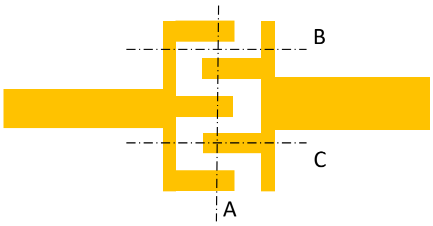

(a)

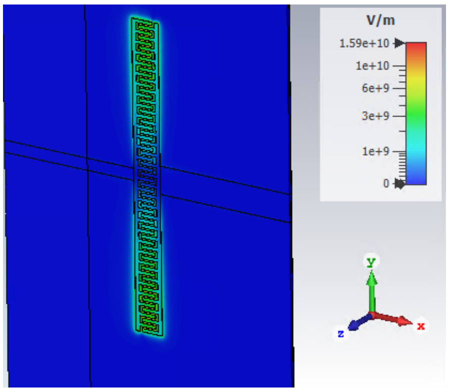

(b) $|J(x,y,z)|$

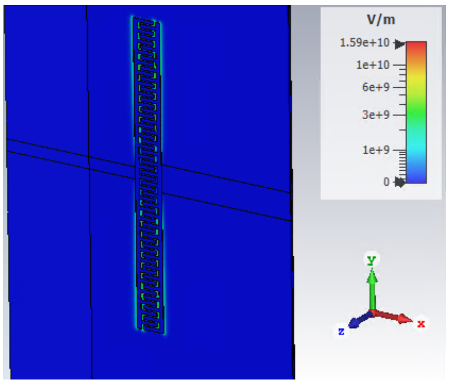

(c) $|J_x(x,y,z)|$

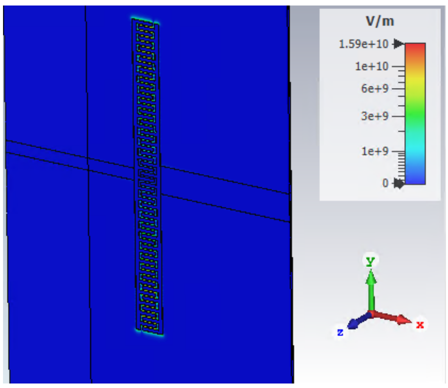

(d) $|J_y(x,y,z)|$

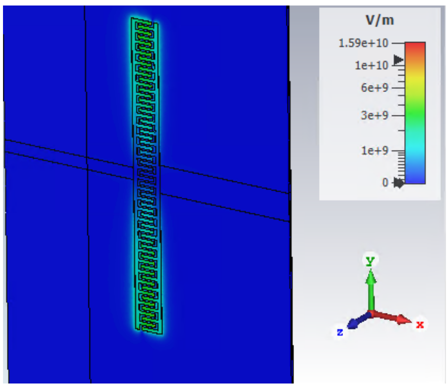

(e) $|J_z(x,y,z)|$

Figure F.1: (a) cuts realised to inspect EM field distribution. (b),(c),(d) Surface current distribution for mode 2.

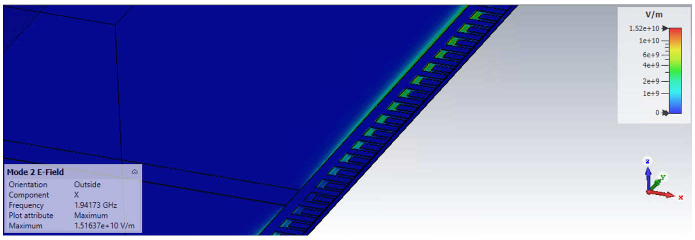

(a) $|E(x,y,z)|$

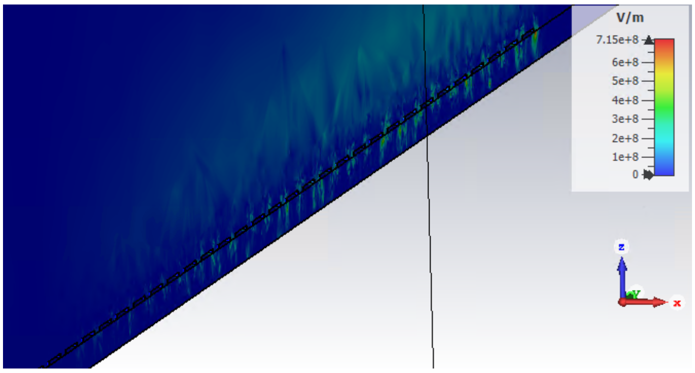

(b) $|E_x(x,y,z)|$

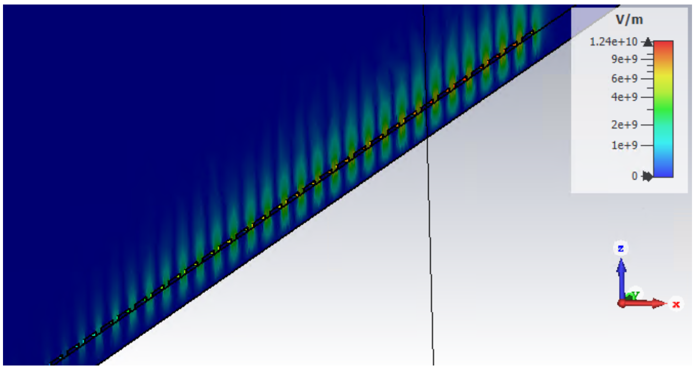

(c) $|E_y(x,y,z)|$

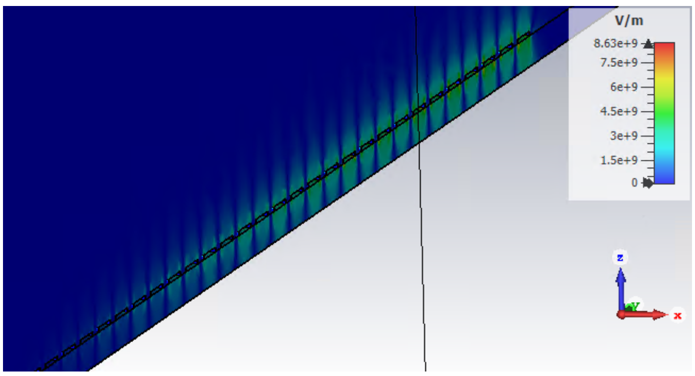

(d) $|E_z(x,y,z)|$

Figure F.2: Electric field distribution absolute value in the plane defined by cut 'A'.

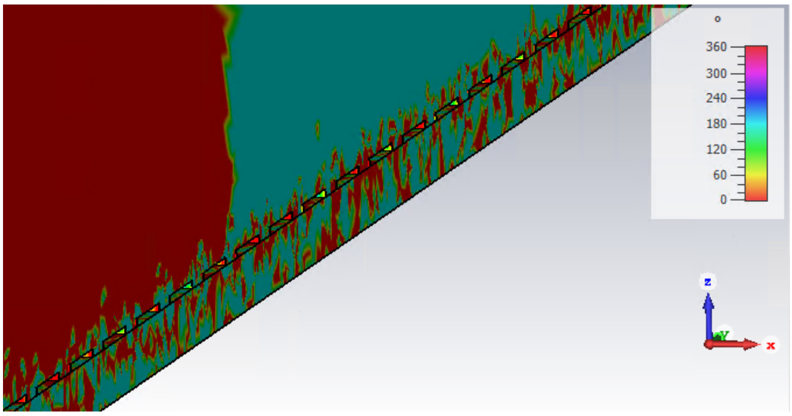

(a) $\arg\{E_x(x,y,z)\}|$

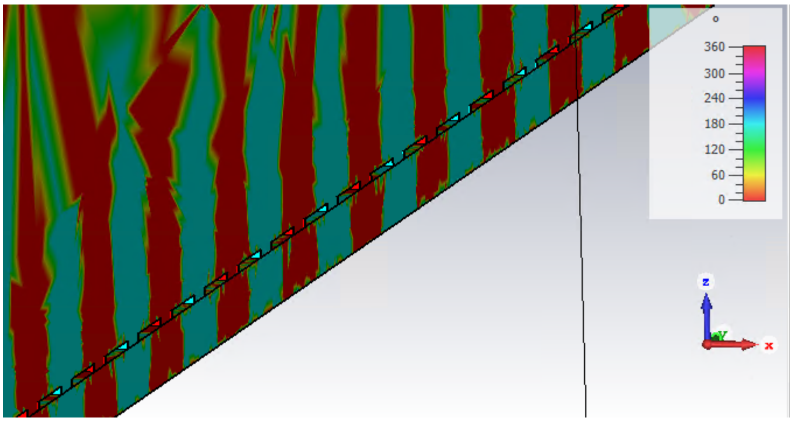

(b) $\arg\{E_y(x,y,z)\}|$

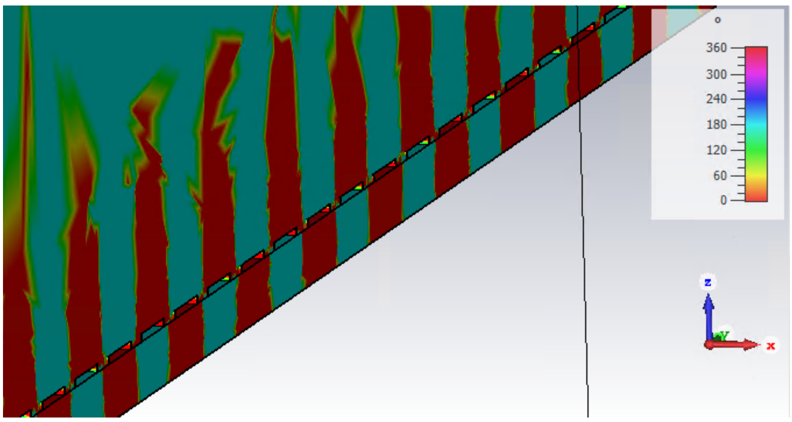

(c) $\arg\{E_y(x,y,z)\}|$

Figure F.3: Electric field distribution phase in the plane defined by cut 'A'.

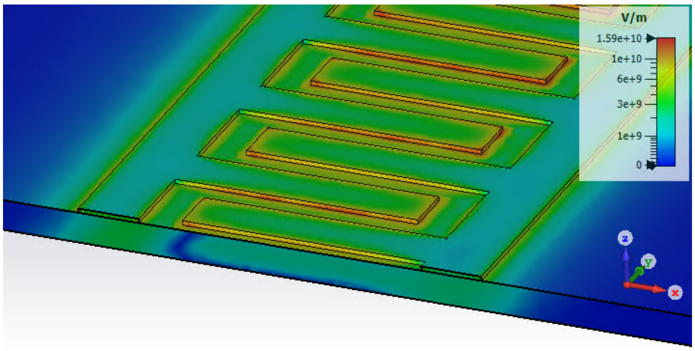

(a) $|E(x,y,z)|$

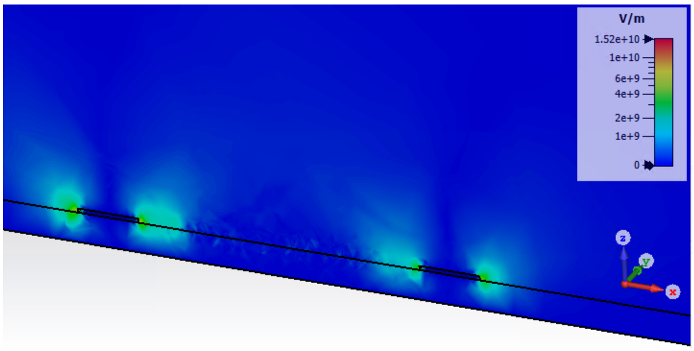

(b) $|E_x(x,y,z)|$

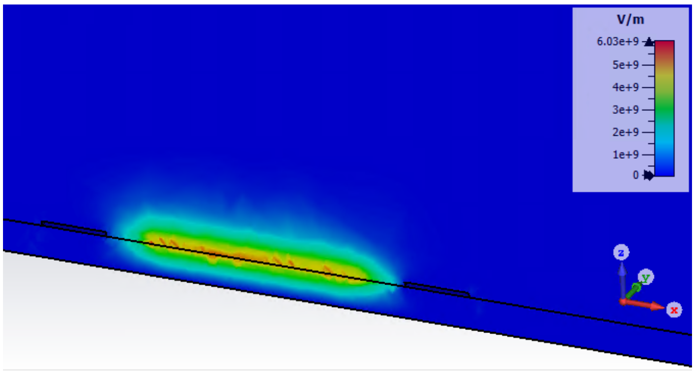

(c) $|E_y(x,y,z)|$

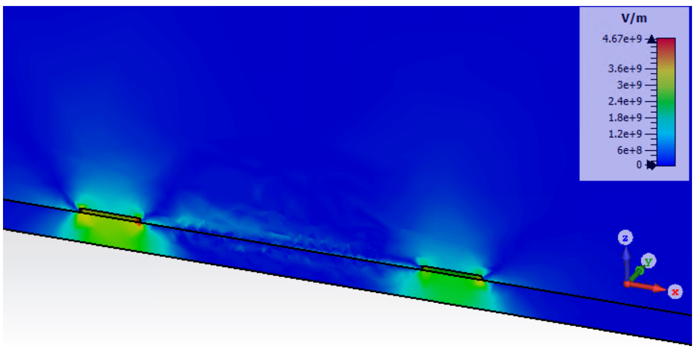

(d) $|E_z(x,y,z)|$

Figure F.4: Electric field distribution absolute value in the plane defined by cut 'B'.

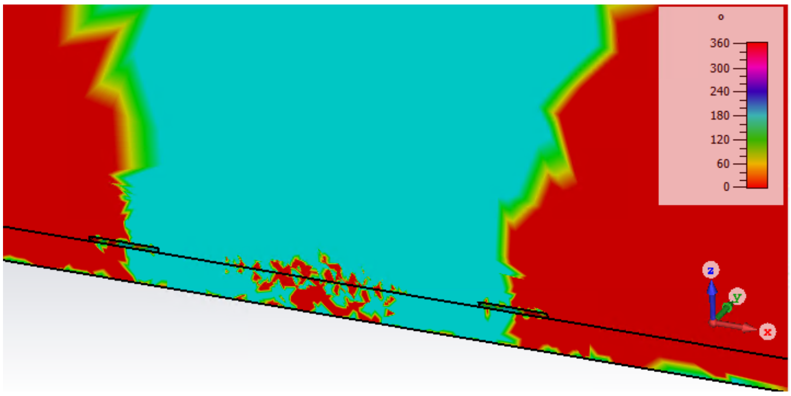

(a) $\arg\{E_x(x,y,z)\}|$

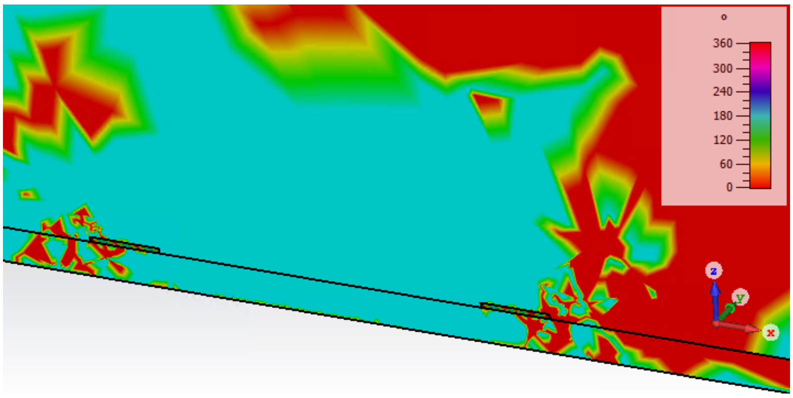

(b) $\arg\{E_y(x,y,z)\}|$

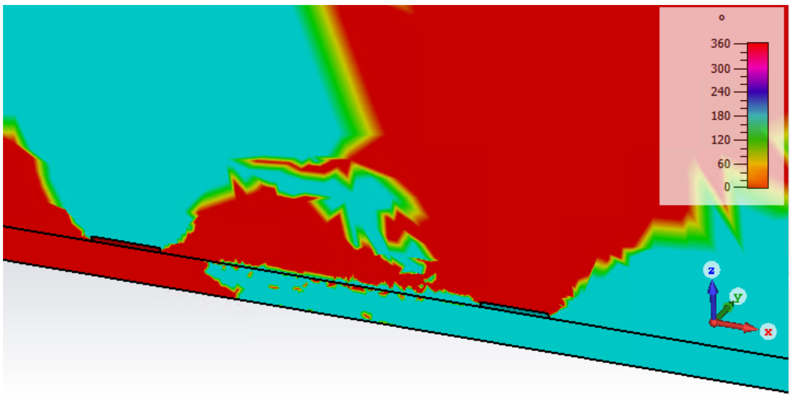

(c) $\arg\{E_y(x,y,z)\}|$

Figure F.5: Electric field distribution phase in the plane defined by cut 'B'.

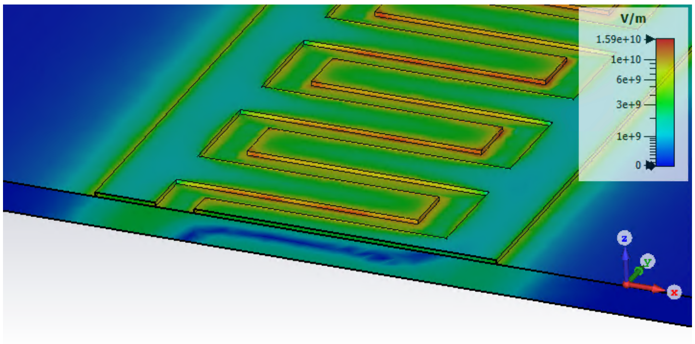

(a) $|E(x,y,z)|$

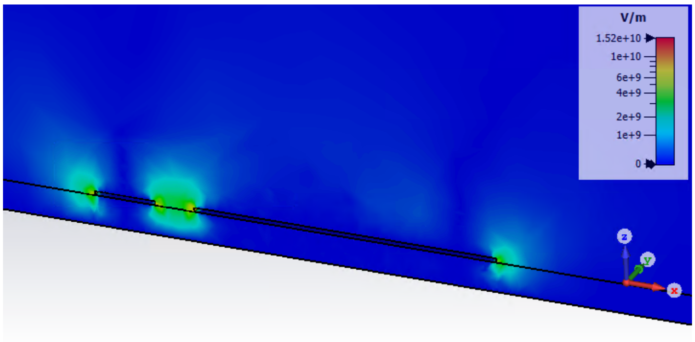

(b) $|E_x(x,y,z)|$

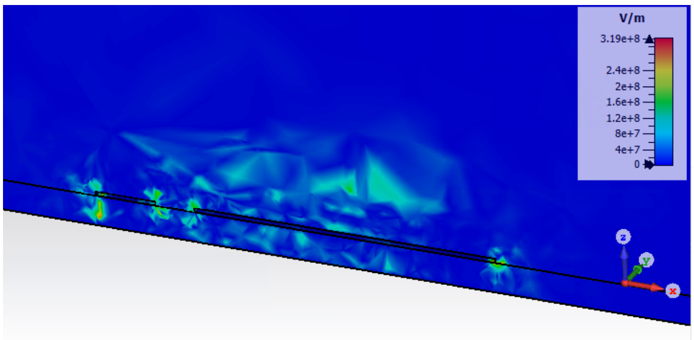

(c) $|E_y(x,y,z)|$

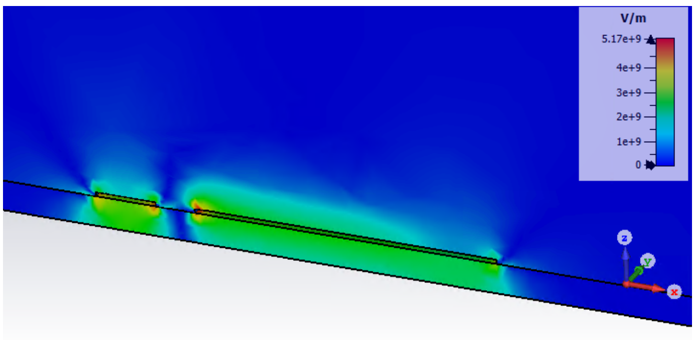

(d) $|E_z(x,y,z)|$

Figure F.6: Electric field distribution absolute value in the plane defined by cut 'C'.

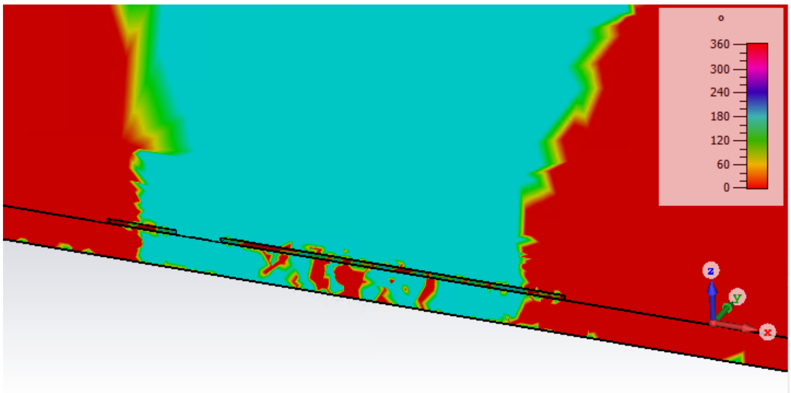

(a) $\arg\{E_x(x,y,z)\}|$

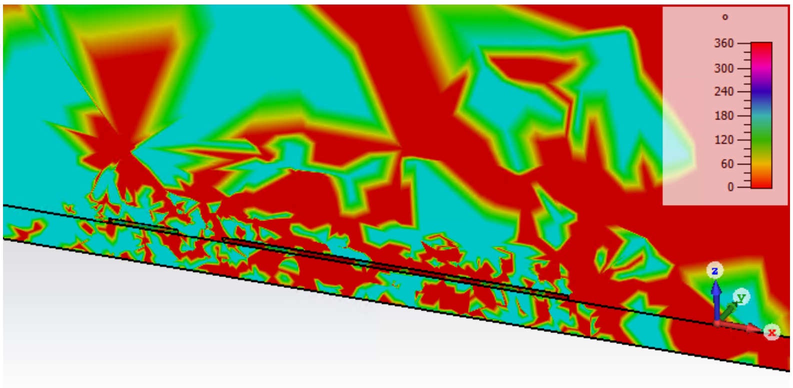

(b) $\arg\{E_y(x,y,z)\}|$

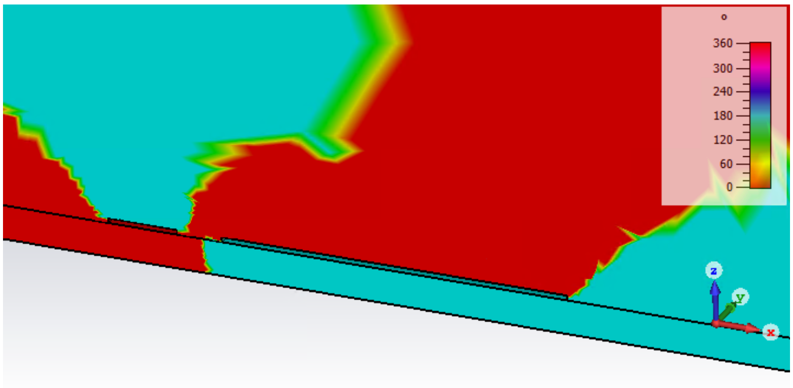

(c) $\arg\{E_y(x,y,z)\}|$

Figure F.7: Electric field distribution phase in the plane defined by cut 'B'.

G | 8 CELL ARRAY SIMULATION SETUP

The array is simulated with CST MW Studio in FD. Solver accuracy parameters is set to 0.01. Total number of meshcells: $\approx$ 1.5M. Frequency range is $f = [0.1\,\text{GHz}, 6\,\text{GHz}]$. Open boundaries condition is imposed.

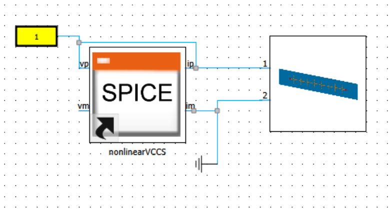

(a)

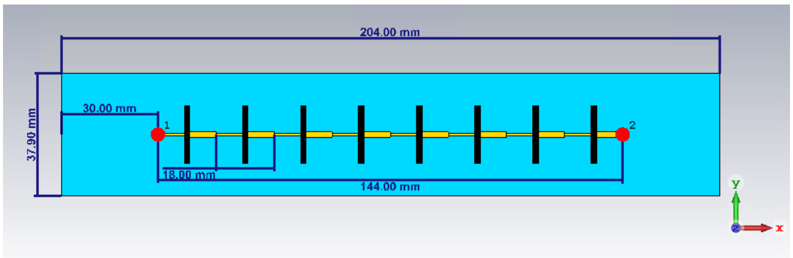

(b)

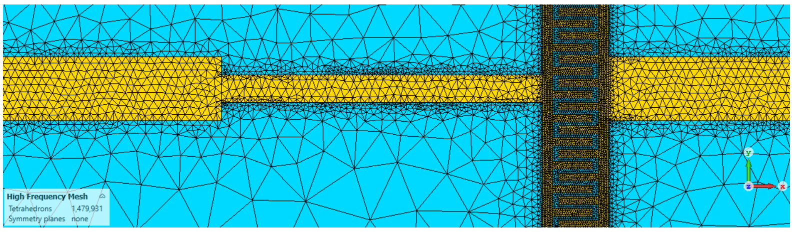

(c)

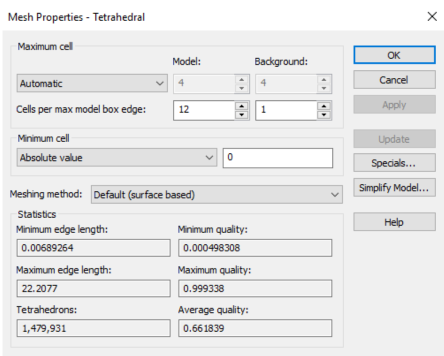

(d)

Figure G.1: (a) Simulation layout. (b) Mesh used for the frequency domain simulation. (c) Mesh setup. Notice, a denser meshgroup has been used in narrow parts.

BIBLIOGRAPHY

[1] W. D. Heiss, “The physics of exceptional points”, *Journal of Physics A: Mathematical and Theoretical*, vol. 45, no. 44, p. 444 016, Oct. 2012, ISSN: 1751-8121. DOI: 10.1088/1751-8113/45/44/444016. [Online]. Available: http://dx.doi.org/10.1088/1751-8113/45/44/444016.

[2] A. Figotin and I. Vitebskiy, “Gigantic transmission band-edge resonance in periodic stacks of anisotropic layers”, *Phys. Rev. E*, vol. 72, p. 036 619, 3 Sep. 2005. DOI: 10.1103/PhysRevE.72.036619. [Online]. Available: https://link.aps.org/doi/10.1103/PhysRevE.72.036619.

[3] M. Y. Nada, M. A. K. Othman, O. Boyraz, and F. Capolino, “Giant resonance and anomalous quality factor scaling in degenerate band edge coupled resonator optical waveguides”, *Journal of Lightwave Technology*, vol. 36, no. 14, pp. 3030–3039, Jul. 2018.

[4] M. Y. Nada, M. A. K. Othman, and F. Capolino, “Theory of coupled resonator optical waveguides exhibiting high-order exceptional points of degeneracy”, vol. 96, no. 18, Nov. 2017, ISSN: 2469-9969. DOI: 10.1103/physrevb.96.184304. [Online]. Available: http://dx.doi.org/10.1103/PhysRevB.96.184304.

[5] T. Mealy, A. F. Abdelshafy, and F. Capolino, “Backward-wave oscillator with distributed power extraction based on exceptional point of degeneracy and gain and radiation-loss balance”, in *2019 International Vacuum Electronics Conference (IVEC)*, Apr. 2019, pp. 1–2. DOI: 10.1109/IVEC.2019.8745292.

[6] D. Oshmari, F. Yazdi, M. A. K. Othman, J. Sloan, M. Radfar, M. M. Green, and F. Capolino, “New oscillator concept based on band edge degeneracy in lumped double-ladder circuits”, *IET Circuits, Devices & Systems*, vol. 13, no. 7, pp. 950–957, Oct. 2019. DOI: 10.1049/iet-cds.2018.5048.

[7] A. F. Abdelshafy, M. A. K. Othman, D. Oshmarin, A. Al-Mutawa, and F. Capolino, “Exceptional points of degeneracy in periodic coupled waveguides and the interplay of gain and radiation loss: Theoretical and experimental demonstration”, 2018. arXiv: 1809.05256 [physics.app-ph].

[8] M. A. K. Othman, M. Veysi, A. Figotin, and F. Capolino, “Degenerate band edge electron beam oscillators: Low starting current”, pp. 1–2, Apr. 2016. DOI: 10.1109/IVEC.2016.7561947.

[9] D. M. Pozar, *Microwave Engineering*. Hoboken, NJ, USA: Wiley, 2012.

[10] M. A. K. Othman and F. Capolino, “Theory of exceptional points of degeneracy in uniform coupled waveguides and balance of gain and loss”, *IEEE Transactions on Antennas and Propagation*, vol. 65, no. 10, pp. 5289–5302, Oct. 2017. DOI: 10.1109/TAP.2017.2738063.

[11] W. Chen, S. Kaya Ozdemir, G. Zhao, J. Wiersig, and L. Yang, "Exceptional points enhance sensing in an optical microcavity", *Nature*, vol. 548, no. 14, pp. 192–196, Aug. 2017. DOI: 10.1038/nature23281.

[12] M. A. K. Othman, X. Pan, G. Atmatzakis, C. G. Christodoulou, and F. Capolino, "Experimental demonstration of degenerate band edge in metallic periodically loaded circular waveguide", *IEEE Transactions on Microwave Theory and Techniques*, vol. 65, no. 11, pp. 4037–4045, Nov. 2017, ISSN: 1557-9670. DOI: 10.1109/TMTT.2017.2706271.

[13] H. Kazemi, M. Y. Nada, T. Mealy, A. F. Abdelshafy, and F. Capolino, "Exceptional points of degeneracy induced by linear time-periodic variation", *Physical Review Applied*, vol. 11, no. 1, Jan. 2019, ISSN: 2331-7019. DOI: 10.1103/physrevapplied.11.014007. [Online]. Available: http://dx.doi.org/10.1103/PhysRevApplied.11.014007.

[14] M. Nada, M. Othman, F. Yazdi, D. Oshmarin, A. Abdelshafv, and F. Capolino, "Unique charactersitics and applications of systems with exceptional points of degeneracy", pp. 869–870, Jul. 2018. DOI: 10.1109/APUSNCURSINRSM.2018.8609108.

[15] J. Wiersig, "Enhancing the sensitivity of frequency and energy splitting detection by using exceptional points: Application to microcavity sensors for single-particle detection", *Phys. Rev. Lett.*, vol. 112, p. 203 901, 20 May 2014. DOI: 10.1103/PhysRevLett.112.203901. [Online]. Available: https://link.aps.org/doi/10.1103/PhysRevLett.112.203901.

[16] C. Dembowski, H. D. Gräf, H. L. Harney, A. Heine, W. D. Heiss, H. Rehfeld, and A. Richter, "Experimental observation of the topological structure of exceptional points", *Phys. Rev. Lett.*, vol. 86, pp. 787–790, 5 Jan. 2001. DOI: 10.1103/PhysRevLett.86.787.

[17] Y. Choi, S. Kang, S. Lim, W. Kim, J.-R. Kim, J.-H. Lee, and K. An, "Quasieigenstate coalescence in an atom-cavity quantum composite", *Phys. Rev. Lett.*, vol. 104, p. 153 601, 15 Apr. 2010. DOI: 10.1103/PhysRevLett.104.153601. [Online]. Available: https://link.aps.org/doi/10.1103/PhysRevLett.104.153601.

[18] C. Dembowski, B. Dietz, H. D. Gräf, H. L. Harney, A. Heine, W. D. Heiss, and A. Richter, "Encircling an exceptional point", *Phys. Rev. E*, vol. 69, p. 056 216, 5 May 2004. DOI: 10.1103/PhysRevE.69.056216. [Online]. Available: https://link.aps.org/doi/10.1103/PhysRevE.69.056216.

[19] B. Dietz, T. Friedrich, J. Metz, M. Miski-Oglu, A. Richter, F. Schäfer, and C. A. Stafford, "Rabi oscillations at exceptional points in microwave billiards", *Phys. Rev. E*, vol. 75, p. 027 201, 2 Feb. 2007. DOI: 10.1103/PhysRevE.75.027201. [Online]. Available: https://link.aps.org/doi/10.1103/PhysRevE.75.027201.

[20] S.-B. Lee, J. Yang, S. Moon, S.-Y. Lee, J.-B. Shim, S. W. Kim, J.-H. Lee, and K. An, "Observation of an exceptional point in a chaotic optical microcavity", *Phys. Rev. Lett.*, vol. 103, p. 134 101, 13 Sep. 2009. DOI: 10.1103/PhysRevLett.103.134101. [Online]. Available: https://link.aps.org/doi/10.1103/PhysRevLett.103.134101.

[21] J. Zhu, Ş. K. Özdemir, L. He, and L. Yang, "Controlled manipulation of mode splitting in an optical microcavity by two rayleigh scatterers", *Opt. Express*, vol. 18, no. 23, pp. 23 535–23 543, Nov. 2010. DOI: 10.1364/OE.18.023535. [Online]. Available: http://www.opticsexpress.org/abstract.cfm?URI=oe-18-23-23535.

[22] J. Wiersig, "Enhancing the sensitivity of frequency and energy splitting detection by using exceptional points: Application to microcavity sensors for single-particle detection", *Phys. Rev. Lett.*, vol. 112, p. 203 901, 20 May 2014. DOI: 10.1103/PhysRevLett.112.203901. [Online]. Available: https://link.aps.org/doi/10.1103/PhysRevLett.112.203901.

[23] C. D. Meyer, Ed., *Matrix Analysis and Applied Linear Algebra*. Philadelphia, PA, USA: Society for Industrial and Applied Mathematics, 2000, ISBN: 0-89871-454-0.

[24] M. L. Povinelli, S. G. Johnson, and J. D. Joannopoulos, "Slow-light, band-edge waveguides for tunable time delays", *Opt. Express*, vol. 13, no. 18, pp. 7145–7159, Sep. 2005. DOI: 10.1364/OPEX.13.007145. [Online]. Available: http://www.opticsexpress.org/abstract.cfm?URI=oe-13-18-7145.

[25] T. Baba, "Slow light in photonic crystals", *Nature Photonics*, vol. 2, no. 18, pp. 465–473, Aug. 2008. DOI: 10.1038/nphoton.2008.146. [Online]. Available: https://doi.org/10.1038/nphoton.2008.146.

[26] J. L. Volakis and K. Sertel, "Narrowband and wideband metamaterial antennas based on degenerate band edge and magnetic photonic crystals", *Proceedings of the IEEE*, vol. 99, no. 10, pp. 1732–1745, Oct. 2011, ISSN: 1558-2256. DOI: 10.1109/JPROC.2011.2115230.

[27] A. F. Abdelshafy, T. Mealy, D. Oshmarin, M. Y. Nada, H. Kazemi, and F. Capolino, "Exceptional points of degeneracy induced in uniform and periodic coupled systems", in *2019 International Conference on Electromagnetics in Advanced Applications (ICEAA)*, Sep. 2019, pp. 1219–1219. DOI: 10.1109/ICEAA.2019.8879227.

[28] G. D. Vendelin, A. M. Pavio, and U. L. Rohde, *Microwave Circuit Design Using Linear and Nonlinear Techniques*. Hoboken, NJ, USA: Wiley, 2005.

[29] I. Bahl, *Lumped Elements for RF and Microwave Circuits*. Norwood, MA, USA: Artech House, 2003.

[30] G. D. Alley, "Interdigital capacitors and their application to lumped-element microwave integrated circuits", *IEEE Transactions on Microwave Theory and Techniques*, vol. 18, no. 12, pp. 1028–1033, Dec. 1970. DOI: 10.1109/TMTT.1970.1127407.

[31] C. Caloz and T. Itoh, "Tl theory of mtms", in *Electromagnetic Metamaterials: Transmission Line Theory and Microwave Applications*. IEEE, 2006. DOI: 10.1002/0471754323.ch3. [Online]. Available: https://ieeexplore.ieee.org/document/5237813.

[32] S. A. Maas, *Nonlinear Microwave and RF Circuits*. Norwood, MA, USA: Artech House, 2003.

[33] K. Kurokawa, "Some basic characteristics of broadband negative resistance oscillator circuits", *The Bell System Technical Journal*, vol. 48, no. 6, pp. 1937–1955, Jul. 1969. DOI: 10.1002/j.1538-7305.1969.tb01158.x.

[34] A. Grebennikov, *RF and Microwave Transistor Oscillator Design*. Chichester, WS, England: Wiley, 2007.

[35] B. Razavi, *Design of Analog CMOS Integrated Circuits*. New York, NY, USA: Artech House, 2017.

[36] G. Ghione and M. Pirola, *Microwave Electronics*, ser. The Cambridge RF and Microwave Engineering Series. Cambridge University Press, 2017. DOI: 10.1017/9781316756171.

[37] E. Yamashita and J. R. Baird, "Theory of a tunnel diode oscillator in a microwave structure", *Proceedings of the IEEE*, vol. 54, no. 4, pp. 606–611, Apr. 1966. DOI: 10.1109/PROC.1966.4780.

[38] R. E. Collin, *Foundations for Microwave Engineering*. Hoboken, NJ, USA: Wiley, 2001.

[39] L. Brillouin, *Wave Propagation in Periodic Structures: Electric Filters and Crystal Lattices*. Hoboken, NJ, USA: Dover Publications, Inc., 1953.

[40] M. Abegaonkar, L. Kurra, and S. K. Koul, *Printed Resonant Periodic Structures and their Applications*. Boca Raton, FL, USA: CRC Press, 1953.

[41] N. W. Ashcroft and N. D. Mermin, *Solid State Physics*. Holt, Rinehart and Winston, 1976.

[42] C. A. Balanis, *Antenna Theory: Analysis and Design*. Hoboken, NJ, USA: Wiley, 2003.

[43] ——, *Modern Antenna Handbook*. Hoboken, NJ, USA: Wiley, 2008.

[44] D. R. Jackson, C. Caloz, and T. Itoh, "Leaky-wave antennas", *Proceedings of the IEEE*, vol. 100, no. 7, pp. 2194–2206, Jul. 2012. DOI: 10.1109/JPROC.2012.2187410.

[45] R. C. Johnson, *Antenna Engineering Handbook*. ??,??,USA: McGraw-Hill, 1993.

[46] (2019). Rogers RO6010, Datasheet, [Online]. Available: https://rogerscorp.com/-/media/project/rogerscorp/documents/advanced-connectivity-solutions/english/data-sheets/rt-duroid-6006-6010lm-laminate-data-sheet.pdf (visited on 12/02/2019).